Università degli Studi di Napoli *Federico II*

A highly innovative design of a photomultiplier: prototypes, engineering and applications in astroparticle physics.

Scientific Disciplinar Sector: FIS/01

PhD Candidate:
Daniele Vivolo

Supervisors:
Prof. Giancarlo Barbarino
Dr. Gianfranca De Rosa

Years 2011/2014

Contents

List of Figures

List of Tables

Introduction

Photon detection represents a critical issue in the current generation of high-energy astroparticle physics experiments. Indeed, many experiments in this rapidly emerging field are based on the detection of the Cherenkov or fluorescence light produced after the passage of charged particles through transparent media like air, water or ice. For these applications, the quality of the experimental results is crucially related to the performances of the adopted photodetectors, for which therefore high efficiency, photon counting capability and large sensitive surface are required.

To date, this field is dominated by PhotoMultiplier Tubes (PMTs), a one-century-old technology that in the last decades has known a whirling evolution, leading to impressive improvements, especially in terms of quantum efficiency and gain, but affected by some intrinsic drawbacks that strongly limit its performances. Moreover, the next generation of experiments will set stricter requirements about photodetectors performances, in particular for what concerns photon counting capability and power consumption. For these reasons, in the last decades several alternatives to PMTs, mainly based on semiconductors, have been introduced. In particular, SiPM technology has achieved a very high level of performances, but its application to astroparticle physics experiment is definitely compromised by its small sensitive surface (typically not exceeding 10 mm^2).

In this context, an interesting solution is represented by the VSiPMT (acronym of Vacuum Silicon PhotoMultiplier Tube), a novel photodetector based on the combination of PMT and Geiger-mode Avalanche PhotoDiode (G-APD) technologies. Indeed, in such device the standard dynode chain of the PMT is replaced by a G-APD, operating in electron multiplier mode, thus matching large sensitive surface and high photon counting performances.

After years of preliminary work aimed at proving the feasibility of the VSiPMT, the encouraging results achieved convinced Hamamatsu Photonics, World leader company in PMT and SiPM manufacture, to realize some prototypes of the device.

This thesis describes accurately all the phases of the VSiPMT project, with a particular focus on the results of the prototype characterization phase and on the possible application of the VSiPMT to the KM3NeT neutrino telescope.

The manuscript is organized in four chapters. In the first one, the open challenges of astroparticle physics are introduced. In particular, it contains a summary of the present knowledge about Cosmic Ray physics, with an overview on cosmic messengers and on detection strategies. The second chapter is focused on photodetectors, with the description of PMT technology and of its semiconductor-based alternatives. The third chapter is dedicated to the VSiPMT project, from the preliminary work required to prove the feasibility of the device to the description of the prototype characterization phase. In addition, the engineering studies for the realization of a new generation of VSiPMT prototypes with

larger photocathode area are presented. In the last chapter, the possible application of the VSiPMT to the KM3NeT neutrino telescope is investigated. The chapter contains the description of the requirements indicated by the collaboration for the photodetectors and of the currently adopted devices, showing the possible advantages of the VSiPMT solution and proposing a new VSiPMT-optimized approach for the front-end electronics.

Chapter 1

Open challenges in astroparticle physics

Astroparticle physics is a field in rapid development and in constant evolution, that can open up new observing windows in astronomy, as well as in cosmology and in the study of phenomena beyond the Standard Model (SM).

Until now, many questions have found an answer, that in turn generated even more (and more complicated) questions.

One of the most fascinating challenges of astroparticle physics is the study of **Cosmic Rays** (CRs). These charged particles, coming from the Universe on our head like a steady rain, have been discovered more than one century ago, but the question about their origin, as well as their propagation and acceleration mechanisms, is still a matter of discussion. Many scenarios have been proposed: according to one of the most popular current hypotheses, galactic Cosmic Rays are generated in Supernovae (Baade and Zwicky [1934]). However, many other astrophysical sources can be considered candidate sources of CRs. For this reason, the investigation of Cosmic Rays can make possible to give a detailed look inside the innermost mechanisms and the mysterious processes which occur in astrophysical objects, making them fantastic laboratories for particle physics, especially for the study of the intrinsic properties and of the acceleration mechanisms of particles like neutrinos, axions and others.

The investigation of the composition of the Universe is among the most important targets of modern particle and astroparticle physics. The nature of **Dark matter** (DM) is still an open question, whose solution could have an incredible impact on the knowledge of the large scale structure in the Universe and, possibly, could lead to the empirical evidence of new unknown particles.

The first evidence for a "missing matter problem" dates back to 1933, when Fritz Zwicky, measuring the velocity dispersion of galaxies in the Coma cluster, found out that the measured value was roughly one order of magnitude larger than that expected from the estimated total mass of the cluster (Zwicky [1933]). However, the formulation of the Dark Matter problem was made only in the 1970s, when from the galactic rotational curves of spiral galaxies it was evidenced the presence of large amounts of mass, on scales much larger than the optical size of galactic disks. Many experimental observations, spanning over the last few decades, provide a strong clue for the existence of a non-luminous and non-absorbing component of matter, interacting only gravitationally and accounting for

about one quarter of the total mass of the Universe.

Today, we know that only the 4% of the Universe is made of ordinary matter. According to the most recent measurements and cosmological models, the 73% of the cosmic energy budget seems to consist of "dark energy" and the remaining 23% of dark matter. The nature of dark energy is still an open question, probably intimately connected with the fundamental question of the "cosmological constant problem" and its investigation represents one of the most challenging and fascinating issues in modern physics.

To date, favored dark matter candidates are Weakly Interacting Massive Particles (WIMPs), well described in the framework of the Minimal Supersymmetric extension of the Standard Model (MSSM).

Three main different approaches are possible for the detection of such particles. The first one is based on *direct techniques*: WIMPs are expected to interact, although with an extremely low cross section, with ordinary matter, inducing atomic recoils. The direct detection of WIMPs is therefore performed measuring the energy released in these atomic recoils, discriminating it from the background. The second approach is carried out by *indirect techniques*: WIMPs can be trapped in the gravitational potential of massive astrophysical objects, such as the Earth, the Sun or the Galaxy itself, through elastic scattering. As a critical density is reached, WIMPs can interact in self-annihilation processes that are expected to produce mainly gamma rays, neutrinos and anti-matter cosmic rays. The observation of these products can provide an indirect evidence for the existence of WIMPs. Conversely, the third approach is based on particle colliders: in this case, WIMPs should be produced in high-energy colliding processes of Standard Model particles and indirectly detected observing the SM particles produced in the related production mechanisms.

Dark matter search is a primary task in modern physics: the discovery of WIMPs and the study of their properties will open up new important windows in the knowledge of the constitution of the Universe, as well as in particle physics and cosmology.

Another crucial task of astroparticle physics is the study of **neutrino oscillations**. One of the main breakthroughs of the past decade has been the discovery that neutrinos are massive particles. This discovery, for which Ray Davis and Masatoshi Koshiba were awarded the Nobel Prize in Physics in 2002, has represented an important evidence of phenomena beyond the Standard Model of particle physics, in which neutrinos are expected to be strictly massless.

The measurement of the quadratic mass differences between the different neutrino flavors has been performed observing neutrino flavor oscillations on their way from the Sun to the Earth. The precise mechanisms of neutrino oscillations are still under investigation. Also in this case, different approaches are possible, depending on the source of the neutrinos under study: Sun, Supernovae and the Earth's atmosphere are possible candidates, as well as experiments in which neutrinos are artificially produced from reactors and accelerators.

The extreme importance of the exploration of the full picture of neutrino masses and oscillations relies in the (possible) discovery of CP asymmetry, that would manifest itself in a difference between the measured rate of $\nu_\mu \to \nu_e$ and $\bar{\nu}_\mu \to \bar{\nu}_e$ transformations, as well as in spectral distortions. According to some recent theoretical works, the CP violation determined from the mixing among the three neutrino flavors could provide an explanation for the origin of the cosmological matter-antimatter asymmetry observed in nature,

that constitutes one of the biggest puzzles of modern particle physics and cosmology.

1.1 Cosmic Rays

Cosmic Rays (CR) are charged particles hitting our atmosphere like a steady rain from space. They were discovered in 1912 Victor Hess (Nobel Prize winner in 1936 for this discovery) as he found an increase of the ionization rate of the atmosphere with altitude. The ionization of the air was believed to have a terrestrial origin, in particular it was thought to arise from the radiation of radioactive elements on Earth or from the radioactive gases or radon isotopes in the ground. Later, it turned out that some of these particles have energies a hundred million times greater than that achievable by terrestrial accelerators.

The discovery was confirmed by several balloon flights at altitudes of up to 5 km. After one of these, made during a near-total eclipse, also the Sun was ruled out as the radiation's source.

In more than one century, the composition and sources of such extraterrestrial cosmic radiation (*Höhenstrahlung*) have been extensively studied and its spectrum has been investigated over more than 12 decades in energy. Cosmic Rays are mainly composed of protons ($\sim 90\%$) and alpha particles ($\sim 9\%$). Also other nuclei and in general all the other stable elements of the periodic table (lifetime $> 10^6$ yrs) are present, with relative abundances and isotopic composition that are very similar to the solar system ones. Therefore, even small differences can provide incredibly useful information about production and propagation mechanisms of Cosmic Rays.

The Cosmic Rays incident at the top of the terrestrial atmosphere are standardly classified in "primary" CR, the particles accelerated at astrophysical sources, and "secondary" CR, that are those produced in the interaction of the primaries with the InterStellar Medium (ISM). Therefore, electrons, protons and helium, as well as carbon, oxygen, iron, and other nuclei synthesized in stars, are primaries. Nuclei as Lithium, Beryllium, and Boron (which are not abundant end-products of stellar nucleosynthesis) are secondaries. Antiprotons and positrons are also in large part secondaries but the hypothesis that a small fraction of them may be primary is currently under investigation (Beringer et al. [2012]). With the exception of particles coming from the solar flares, Cosmic Rays are originated from outside the solar system. However, the incoming radiation is "modulated" by the solar wind, the expanding magnetized plasma generated by the Sun, which has the effect of decelerating and partially excluding the lower energy component of galactic CR.

The interaction of Cosmic Rays with air nuclei in the upper atmosphere can produce secondary particles and initiate extensive showers of electrons, photons, muons and neutrinos reaching the ground level.

Experimentally, the energy spectrum of cosmic rays in wide energy range is rather featureless, though it is almost well approximated by a broken power-law:

$$\frac{dN}{dE} = N_0 E^{-\alpha}, \tag{1.1}$$

where N_0 is a normalization constant and α is the so-called "spectral index". As shown in Fig. 1.1, the Cosmic Rays spectrum rapidly decreases with increasing energy, with very few structures. In particular, three breaks can be observed. The first one occurs at about
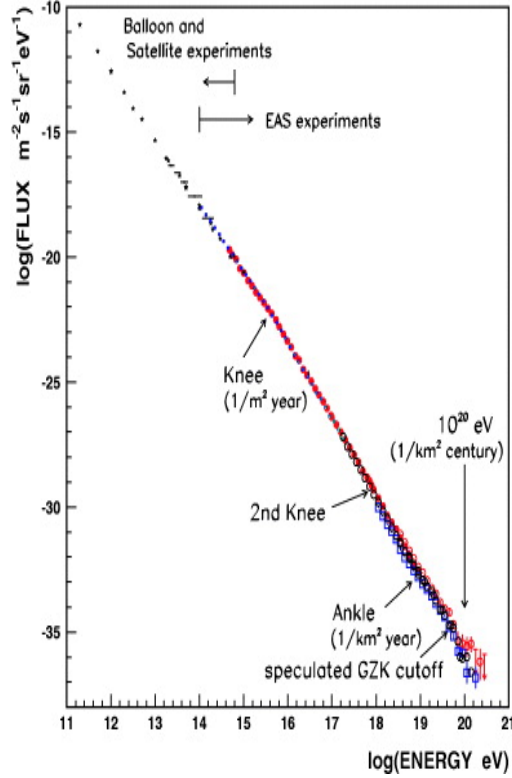
Figure 1.1: Cosmic Ray spectrum.

4 PeV, with the spectral index abruptly changing from $\gamma \simeq 2.7$ to $\gamma \simeq 3.2$. Similarly, at about 400 PeV the spectrum gets slightly steeper. These two breaks are commonly referred to as "knee" and "second knee", respectively (see Fig. 1.2 for details). The steepening of the Cosmic Ray spectrum around 4 PeV is supposed to be related with the upper end of galactic sources of Cosmic Rays (Peters [1961]). In particular, the change in the spectral index of the CR spectrum depends on the different origin and composition of Cosmic Rays (Gaisser [2006]).

The curvature radius of a particle with charge Ze in a uniform magnetic field is given by:

$$r = \frac{10E_{15}}{ZeB_{-6}},$$ (1.2)

where E_{15} is the particle energy in PeV and B_{-6} is the field intensity in μG. Below the knee the curvature radius of the particles is smaller than the galactic disk thickness, therefore their sources must belong to our Galaxy, where Cosmic Rays propagate by diffusion. Above the knee, the curvature radius becomes greater than the disk thickness, and CR may escape into the galactic halo, where the density is very low and the magnetic field is weaker than the disk one. Only a fraction of the particles that are diffusing through the halo can re-enter the disk, going into a zone with stronger magnetic field. This leakage of CR induces an increase of the spectral index because the escape probability is greater for higher energy particles.

A change of composition of CR would represent a possible hint for the transition from Galactic to extra-galactic Cosmic Rays. Acceleration and propagation both depend on magnetic fields and hence on the magnetic rigidity, defined as the total momentum divided

15
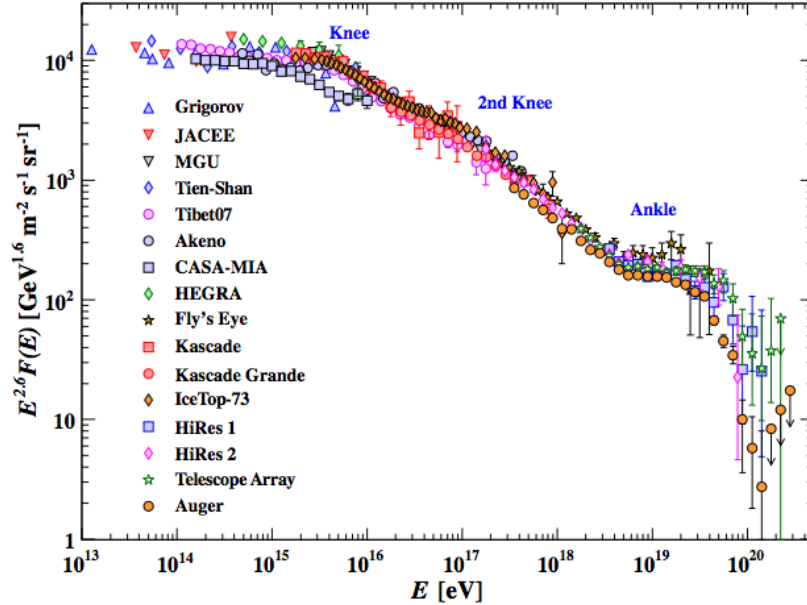
Figure 1.2: Cosmic Ray spectrum: the three breaks.

by the charge of the particle being accelerated. Thus, a likely signature of the upper-end of one population of particles would be an increase in the relative abundance of heavy nuclei, first protons and then helium, carbon and so on (Peters [1961]). The first evidence of such sequence is provided by the KASCADE experiment, whose data cover the energy range below $10^{18}eV$ (Apel et al. [2013]).

The observed mean mass increase above the knee indicates that the knee marks the maximum acceleration energy of the most abundant Galactic sources. This leads to the hypothesis that heavy primaries would experience the same limitation of particle acceleration, giving rise to the second knee, also called the "Iron-knee", observable at about $E_{knee}^{Fe} \sim 26 \times E_{knee}^{p}$ (~ 400 PeV), that effectively represents the end mark of the Galactic CR spectrum.

On the other side, in correspondence to the third break, occurring at about 3 EeV, the spectrum gets harder, with the spectral index decreasing back to $\gamma \simeq 2.8$. This break, called "ankle", is widely interpreted as a crossover from a steeper galactic component to a harder component of extragalactic origin.

At the highest energies ever detected ($\sim 10^{20}$ eV) the measured flux is limited by the very low statistics of such rare events. According to predictions of Greisen, Zatsepin, and Kuzmin, ultra high energy cosmic rays (UHECRs) rapidly lose energy by the interaction with the 2.7 K cosmic microwave background radiation (CMB), causing their spectrum to be cut off at energies around 6×10^{19} eV (the so-called *GZK cutoff*) (Grupen [2005]).

1.2 Cosmic Rays accelerators

Many questions about the observation of Cosmic Rays are still waiting for an answer: about the nature itself of these particles; about cosmic accelerators mechanisms, boosting particles to the extremely high observed energies; about the maximum energy achievable

16

by galactic sources and about propagation mechanisms through the Universe.

In principle, the CR energy spectrum could extend beyond the maximum energy that a proton can maintain when traveling over large cosmic distances, due to collisions with the 2.7 K Cosmic Microwave Background radiation (CMB). An hypothetical observation of a large flux above this energy limit would be attributed to entirely new cosmic phenomena, opening completely new scenarios. An answer to all these open questions can be searched through a multi-messenger approach based on the interplay of detectors for high-energy γ-rays, neutrinos and charged Cosmic Rays.

Several models have been proposed to explain the CR spectrum at high energies, based on the connection between non-thermal emission from astrophysical sources and particle acceleration processes.

Basically, two different approaches for the production of charged UHECRs exist, referred to as the "top-down" and "bottom-up" scenarios. The first one is based on the decay of super heavy particles (with masses ranging from 10^{11} eV up to the GUT scale), resulting in protons of energies up to 10^{22} eV. In this scenario, the GZK cut-off is avoided, since the protons are produced in the Earths vicinity. Furthermore, the proton signal is expected to be accompanied by a large flux of neutrinos and high-energy photons. However, the absence of such signatures in combination with the CR suppression at highest energies favor the GZK cut-off and hence support the argument of the bottom-up scenario.

In this scenario, based on the hypothesis that particle production and acceleration processes happen in distant sources, there are mainly two kinds of acceleration mechanisms: direct acceleration of charged particles by an electric field and statistical acceleration in a magnetized plasma.

The former acceleration mechanism, in which the electric field that accelerates the charged particles may originate, for example, from a rotating magnetic neutron star (pulsar) or a rotating accretion disk threaded by magnetic fields, is not widely favored as acceleration mechanism, most of all because it is difficult to obtain the characteristic power-law spectrum of the observed CR.

The second acceleration mechanism was suggested by Enrico Fermi in 1949 (Fermi [1949]). According to this model, individual charged particles are accelerated due to repeated collisionless scatterings (encounters) of the particles either with randomly moving inhomogeneities of the turbulent magnetic field or with shocks in the medium (Bhattacharjee and Sigl [2000]). In the first case, an average energy gain can be expected after many encounters even when taking into account that the particle may either lose or gain energy at each encounter. This mechanism is called *second-order Femi mechanism* because the average energy gain in this case is proportional to $\left(\frac{u}{c}\right)^2$, where u is the relative velocity of the cloud with respect to the frame in which the CR ensemble is isotropic, and c is the velocity of light. However, this quadratic dependence implies an acceleration time scale larger than the typical escape time of CR in the Galaxy, making the second-order Fermi mechanism acceleration process not efficient. In addition, the expected resulting spectrum does not in general have a power-law shape. If collisions of particles with plane shock fronts are taken into account, a more efficient version of Fermi mechanism is obtained. According to this model, the acceleration of galactic Cosmic Rays is described by the stochastic energy gain of charged particles each time they go through a plasma shock wave propagating into the ISM, while being confined inside the acceleration region by a magnetic field. In this case (commonly referred to as *first-order Femi*
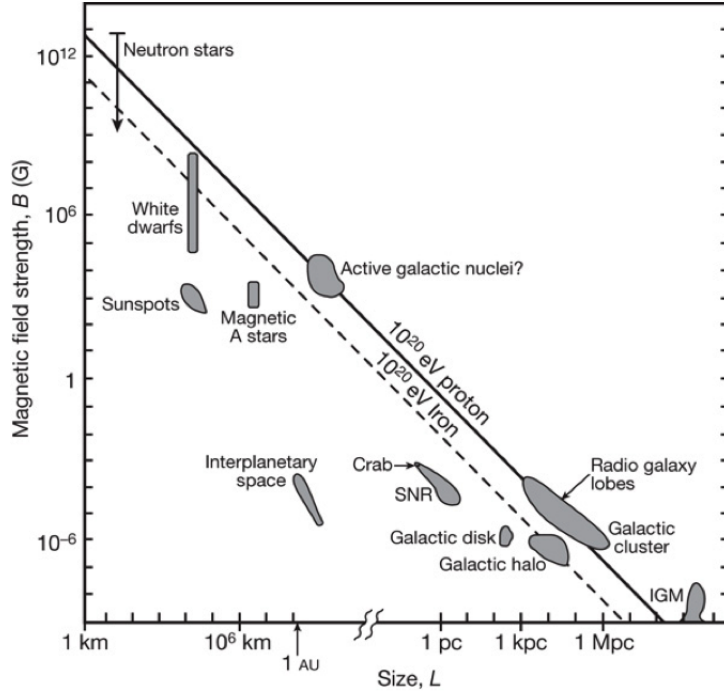
Figure 1.3: The Hillas diagram showing size and magnetic field strengths of possible sites of particle acceleration.

mechanism), there is a first order dependence of the average energy gain of particles on the relative velocity between the shock front and the isotropic CR frame. The first-order Femi mechanism is particularly interesting because shock accelerations are expected to hold in many astrophysical sources, like SuperNova Remnants (SNRs), and the expected spectrum for accelerated particles corresponds to a power-law. The first-order Fermi acceleration mechanism, in the form of Diffusive Shock Acceleration (DSA), can accelerate particles to energies perhaps up to $\sim 10^{17}$ eV but probably not much beyond.

The knee and the second knee are interpreted as the points where cosmic accelerators in the galaxy, depending on the charge number Z (protons or heavier particles in the case of knee and second knee, respectively), have reached their maximum energy.

The relation between the size L of the acceleration region and the magnetic field intensity B present in it and responsible of the shocks are represented in the so-called *Hillas plot* (see Fig. 1.3). In non-exotic acceleration processes, particles are confined within a region and accelerated by magnetic field shocks until they reach a maximum energy, above which they are no more confined by the magnetic field and are able to escape. Approximately, the value of the maximum achievable energy is given by

$$E_{max} \sim ZBL, \qquad (1.3)$$

shown in Fig. 1.3 as a solid/dashed line for 10^{20} eV protons/iron nuclei, respectively. Only the astrophysical sources lying above the lines can represent possible candidates for the acceleration of particles up to energies into the GZK region (Pablo M. Bauleo [2009]). Candidates that satisfy the conditions for acceleration up to 10^{20} eV are neutron stars with very strong magnetic fields, AGN (Active Galactic Nuclei) jets, Pulsars and GRBs.

The GZK cutoff

UHECR protons are expected to lose a significant part of their energy (about one half) in photo-production interactions that cause the GZK effect ends up in neutrinos (Beringer et al. [2012]). A measure of this cosmogenic neutrino flux above $10^{18}eV$ would represent a fundamental step in understanding the UHECR uncertainties. The magnitude of the cosmogenic neutrino flux has a strong dependence on the Cosmic Ray spectrum at the acceleration stage, as well as on cosmic ray composition and cosmological evolution of the cosmic ray sources.

The expected rate of cosmogenic neutrinos is lower than current limits obtained by Ice-Cube (Abbasi et al. [2011]), the Auger observatory (Abreu et al. [2011]), RICE (Kravchenko et al. [2012]), ANITA-2 (Gorham et al. [2012]) and the Waxman-Bahcall benchmark flux of neutrinos produced in Cosmic Ray sources (Waxman and Bahcall [1999]).

1.3   Cosmic messengers

A multi-wavelength study of the electromagnetic radiation, ranging from radio to γ-rays, can provide very useful information about mechanisms of jet formation and hence about the origin of ultra high energy Cosmic Rays. However, γ-ray astronomy is strongly limited by the relatively short mean free path of photons (about $10Mpc$ for $E > 10^{13}eV$). On the other side, if one assumes protons as astronomical probes some source identification problems arise related to the proton *Larmor radius* in the galactic and intergalactic magnetic field. The deflection angle, in fact, is given by

$$R_L = \frac{E}{qBc} \tag{1.4}$$

where B is the magnetic field and E is the energy of protons. The galactic magnetic field ($B \sim 3 \times 10^{-6}$ G) produces a sensible deflection for cosmic protons with energy $E < 10^{18}$ eV, while for high energies ($E > 50$ EeV) the deflection due to galactic or extragalactic magnetic fields is negligible. Low energy protons have weak source pointing probes while, due to the GZK cutoff, high energy protons are not able to travel over distances higher than few tens of Mpc, thus providing a small field of view.

Neutrino astronomy provides both excellent source pointing capability and an unrivaled field of view. In fact, since neutrinos have only weak interactions with matter, they can escape much denser celestial environments than light, thus behaving as tracers of the innermost processes occurring in astrophysical sources, which are hidden to traditional astronomy. Moreover, having no electric charge, neutrinos can move in a straight line, regardless of the presence of magnetic fields on their path, so that they will point back to their source.

Taking advantage of these characteristics, it is clear that their use in a complementary way with high energy protons and high energy photons can give important insight on the hadronic mechanisms occurring in the sources as well as revealing their nature.

1.3.1   High energy charged CR

For high energy charged CR (where the expected flux is very faint) ground-based experiments exploiting the *cascade* effect are required.

Air showers are caused by the interactions in the atmosphere of single Cosmic Rays sufficiently energetic to make their cascades detectable at the ground level. The shower has a hadronic core, acting as a collimated source of electromagnetic subshowers, generated mostly from $\pi^0 \to \gamma\gamma$ decays. The most numerous charged particles produced in these processes are electrons and positrons. The number of muons, produced by decays of charged mesons, is an order of magnitude lower. At ground level, air showers spread over very large areas, therefore arrays of detectors (operating for long times) are required to study CR with primary energy $E_0 > 10^{14}$ eV. Indeed, for higher energies the expected flux is too low to be measured with small detectors in balloons and satellites.

Air shower detectors can be classified in three types:

- shower arrays studying the size and the lateral distribution of the shower at the ground level;

- Cherenkov detectors, aimed at the detection of the Cherenkov radiation emitted by the charged particles of the shower;

- fluorescence detectors, that study the nitrogen fluorescence excited by the charged particles in the shower.

In the last case, since the fluorescence light is emitted isotropically, the showers can be observed from the side.

In particular, the fluorescence technique is particularly useful in the energy range above 10^{17} eV as it makes possible to establish the primary energy in a model-independent way. Indeed, since the fluorescence light is emitted isotropically, the longitudinal development of the showers can be observed, from which it is possible to obtained the primary energy by integrating the energy deposition in the atmosphere. However, results are strongly dependent on the light absorption in the atmosphere.

1.3.2 Gamma-ray astronomy

SNR shocks are among the most promising candidates for galactic Cosmic Rays acceleration. This hypothesis is strongly supported by the observed $\gamma-$ray emission at TeV energies from supernova remnants. One of the most outstanding aims of the current generation Imaging Atmospheric Cherenkov Telescopes (IACT), is to provide detailed spectral and morphological information about the observed $\gamma-$rays, in order to investigate their production mechanisms. To date, two competing scenarios have been proposed. According to the first one, the TeV $\gamma-$ray radiation can be generated by the high energy ($\gg 10$ TeV) electrons present in SuperNova Remnants (SNR), where they are responsible for X-ray synchrotron emission. In particular, TeV $\gamma-$rays can be produced through Inverse Compton (IC) scattering of Cosmic Microwave Background (CMB) photons or, alternatively, through non-thermal Bremsstrahlung in the field of the nuclei encountered in the medium. Unless the medium is dense, IC scattering is the dominant $\gamma-$rays production process.

In the second scenario, $\gamma-$rays are produced in the decay of the neutral pions ($\pi^0 \to \gamma\gamma$) generated in the hadronic interactions of Cosmic Ray ions with target material. In this interaction processes, the production of π^0s is expected to be accompanied by the production of charged pions, subsequently decaying in neutrinos and muons that in turn

give rise to secondary electrons. In this case, the $\gamma-$rays will carry on only a small part of the energy of the initial CR ion (typical expected values are of the order of $\sim 15\%$), therefore a possible observations of $\gamma-$rays with energies above 100 TeV would probe the spectrum of Cosmic Rays at energies near (or even beyond) the knee.

The detection of $\gamma-$ray emission at TeV energies for several SNRs is a strong hint for the latter predictions, but it cannot be considered a proof of the fact that SNRs can accelerate CRs unless the degeneracy between the leptonic and hadronic model is solved. To date, an unambiguous and conclusive proof of the SNR paradigm for the origin of CRs is still missing. However, multi-wavelength observations of young SNRs, ranging from radio to very high energy TeV $\gamma-$rays, can represent a fundamental tool for the investigation of the right scenario.

Young SNRs are ideal laboratories to study particle acceleration mechanisms at work because these objects are still in a phase of their evolution in which the shocks are strong and actively accelerating particles to the highest energies.

Two extremely interesting candidates are **RX J1713.7-3946** and **RXJ0852.0-4622** (Vela jr). They are both young SNRs characterized by absolute fluxes above 10 TeV, exceeding that of the Crab nebula, which is considered as standard candle in ground based $\gamma-$ray astronomy. In particular, the former has an integral flux equal to $F(> 1$ TeV$) \approx 1.6 \times 10^{-11} cm^{-2} s^{-1}$, while Vela Jr is characterized by an integral flux equal to $F(> 1$ TeV$) \approx 1.5 \times 10^{-11} cm^{-2} s^{-1}$.

From the observation of the TeV $\gamma-$ray emission alone, it is difficult to discriminate between leptonic and hadronic models. Fig. 1.4 shows the $\gamma-$ray spectrum for RX J0852.0-4622 observed with Fermi-Large Area Telescope (LAT) in the energy band range from 10^3 to 10^8 MeV and numerical models for the different models (Tanaka et al. [2011]). In this case, the observed spectrum seems to be better explained by the hadronic scenario than the leptonic one. Regarding RX J1713.7-3946, in 2002 the CANGAROO collaboration (Enomoto and Enomoto [2002]) produced the first evidence for the observation of $\gamma-$rays of π^0 origin. In Fig. 1.5 it is shown the energy spectrum of RX J1713.7-3946 taken by the Fermi Large Area Telescope and H.E.S.S., together with different numerical models of RX J1713.7-3946 $\gamma-$ ray spectra in the range from GeV to hundreds of TeV (Abdo [2011]). It was observed that the hard spectrum of RX J1713.7-3946 is weakly compatible with the conventional hadronic model. Therefore, this was assumed to constitute a clear evidence supporting the leptonic scenario, contrarily to the initial guess proposed by CANGAROO. However, under the assumption of a highly inhomogeneous Inter-Stellar Medium (ISM) distribution, the observed hard spectrum becomes compatible also with the hadronic scenario (Fukui [2013]). In particular, if the hadronic process is valid, the spatial distribution of the $\gamma-$rays is expected to correspond to that of the surrounding ISM. In order to test this hypothesis, a detailed comparison between the ISM protons and the high-resolution $\gamma-$ray image of H.E.S.S. has been performed by Fukui [2013], for both RX J1713.7-3946 and RX J0852.0-4622. A very good spatial correspondence between the ISM proton distribution and the TeV $\gamma-$ray distribution has been found, providing a strong support in favor of the hadronic scenario. However, even under these conditions a leptonic model consistent with the non-thermal X-ray distribution cannot be excluded.

Observations of multi-TeV $\gamma-$ray emission from extreme astrophysical environments could play a key role in our understanding of Cosmic Ray acceleration. This is a key
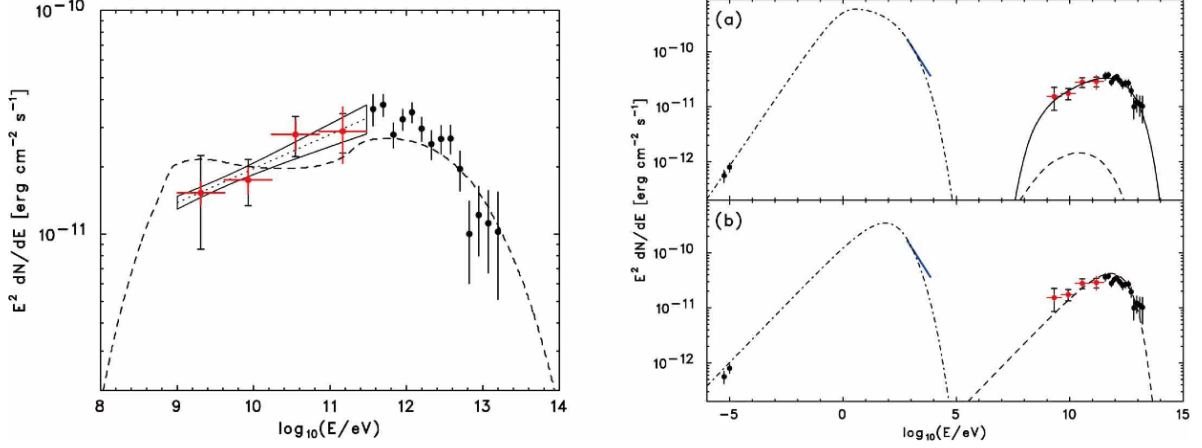
Figure 1.4: Energy spectrum taken by Fermi-LAT and numerical models for RX J0852.0-4662 in the range $10^3 - 10^8$ MeV. *Left panel*: the vertical red lines and the black caps indicate statistical and systematic errors, respectively. The dotted line shows the best-fit power-law obtained from the maximum likelihood fit for the entire $1 - 300$ GeV band. The dashed curve is the π^0-decay spectrum (hadronic model). *Right panel*: Broadband SED of RX J0852.0-4622 with (a) the hadronic model and (b) the leptonic model. The solid, dashed, and dot-dashed lines represent the contributions from π^0-decays, Inverse Compton scattering and synchrotron radiation, respectively (Fukui [2013]).
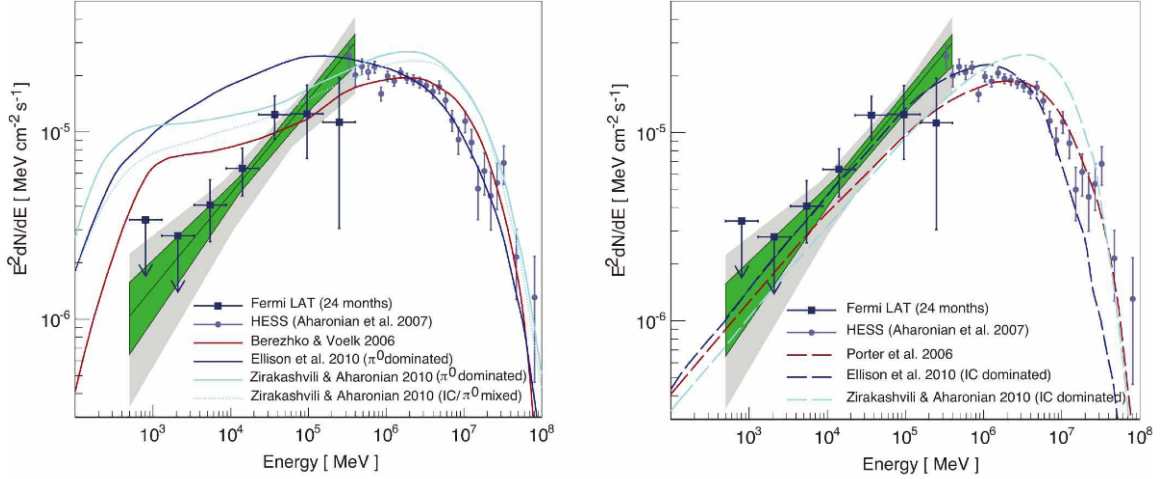
Figure 1.5: Energy spectrum taken by Fermi-LAT and numerical models for RX J1713.7 in the range $10^3 - 10^8$ MeV. Solid lines indicate the numerical model of the hadronic scenario (π^0-decay spectrum, left) and the leptonic scenario (Inverse Compton scattering spectrum, right). The green region shows the uncertainty band obtained from maximum likelihood fit of the spectrum assuming a power law between 500 MeV and 400 GeV for the default model of the region. The gray region depicts the systematic uncertainty of this fit obtained by variation of the background and source models. The black error bars correspond to independent fits of the flux of RX J1713.7-3946 in the respective energy bands. Upper limits are set at a 95% c.l. (Fukui [2013]).

22

science goal for future instruments that will extend the energy coverage of ground based $\gamma-$ray astronomy up to 100 TeV and beyond.

1.3.3 High energy neutrinos

As shown in the previous section, highly efficient particle acceleration environments, such as powerful outflows and shock waves, where high energy protons interact with matter or radiation around the astrophysical source, can in general be considered as candidate sources of high energy neutrinos. Indeed, proton-proton $(p - p)$ collisions and/or photohadronic $(p - \gamma)$ interactions in shock fronts lead to the production of mesons (essentially charged pions):

$$p + p \rightarrow \begin{cases} p + n + \pi^+ & 1/3 \text{ of all cases} \\ p + p + \pi^0 & 2/3 \text{ of all cases} \end{cases}, \tag{1.5}$$

$$p + \gamma \rightarrow \Delta^+ \rightarrow \begin{cases} n + \pi^+ & 1/3 \text{ of all cases} \\ p + \pi^0 & 2/3 \text{ of all cases} \end{cases}. \tag{1.6}$$

Neutral pions decay into $\gamma-$rays with a probability of $\sim 98.8\%$:

$$\pi^0 \rightarrow \gamma + \gamma \tag{1.7}$$

while charged pions generate neutrinos through leptonic decays:

$$\begin{aligned} \pi^+ &\rightarrow \mu^+ + \nu_\mu, \\ \mu^+ &\rightarrow e^+ + \nu_e + \bar{\nu}_\mu; \end{aligned} \tag{1.8}$$

The same processes occur for incident neutrons instead of protons, leading to the production of π^- particles:

$$\begin{aligned} \pi^- &\rightarrow \mu^- + \bar{\nu}_\mu, \\ \mu^- &\rightarrow e^- + \bar{\nu}_e + \nu_\mu; \end{aligned} \tag{1.9}$$

At high energies, also kaons can contribute to the spectrum (multipion production processes):

$$K^+ \rightarrow \mu^+ + \nu_\mu, \tag{1.10}$$

The second channel in 1.5 generates an extra neutrino from the beta decay of the neutron (decaying after a mean lifetime of $\tau_n \sim 10^3$ s), but this neutrino, besides arriving considerably later than the others, carries around 50 times less energy. However, it is possible to consider it in the computation of the neutrino flux:

$$n \rightarrow p + e^- + \bar{\nu}_e. \tag{1.11}$$

Under the hypothesis that pions with negative and positive charge occur equally, the chains described in 1.8 and 1.9 produce neutrinos in the flavor ratio, at the source, of:

$$\nu_e : \nu_\mu : \nu_\tau = 1 : 2 : 0, \tag{1.12}$$

with no production of tau neutrinos. However, for neutrinos coming from astrophysical sources and traveling large distances before reaching the Earth the mechanism of neutrino oscillations equalizes the flavor ratio to $1:1:1$, a crucial feature to take into account.

The expected neutrino flux can be estimated by assuming photo-hadronic interactions between the observed Ultra-High Energy Cosmic Rays (UHECR) and the observed photon spectra of cosmic sources or by proton-proton interactions of Cosmic Rays. Imposing energy conservation, the following relation is obtained:

$$\int_{E_\gamma^{min}}^{E_\gamma^{max}} E_\gamma \frac{dN_\gamma}{dE_\gamma} = K \int_{E_\nu^{min}}^{E_\nu^{max}} E_\nu \frac{dN_\nu}{dE_\nu}, \tag{1.13}$$

where E_γ^{max}, E_ν^{max}, E_γ^{min} and E_ν^{min} are the maximum and the minimum energy of photons and neutrinos, respectively. K is a scale factor, depending on the type of interaction. For $p-p$ interactions, $K \sim 1/3$, while for $p-\gamma$ interactions, assuming that the fraction of energy transferred by the proton to the charged pion is $< x_{p\to\pi} > \sim 0.2$ and that the four leptons produced by the decay of the pion carry an equal amount of energy, the relation between neutrino and proton energy is $E_\nu = E_p/20$.

Astrophysical high energy neutrino sources

In general it is possible to consider as candidate sources of high energy neutrinos all astrophysical sources characterized by a non-thermal emission, and in particular all the objects in which baryonic acceleration processes take place.

The most likely sources of Galactic Cosmic Rays are shell-type *Supernovae* explosions, releasing a large amount of their energy via the emission of MeV neutrinos and, in the case of Type-II explosions, of a TeV-neutrino flux, apart from the thermal neutrino emission prior to the optical outburst. It was Kamiokande II to observe, for the first time, MeV neutrinos in coincidence of SN 1987A. The expected neutrino flux for such a Supernova is compatible with the sensitivities of today neutrino telescopes. However, the current relic diffuse flux is about four orders of magnitude lower and cannot be tested (Becker [2008]).

Supernova Remnants (SNR) are, as discussed previously, among the main CR accelerator candidates. The maximum energy to which particles can be boosted turns out to be somewhat below the knee, at about 10^{14} eV (Katz and Spiering [2012]). However, by effect of interactions of Cosmic Rays with the magnetic fields in the acceleration region, energies of up to 10^{16} eV are reachable. In the framework of the hadronic scenario, the interaction processes between the protons accelerated in SNRs shocks and ambient medium are accompanied by the production of γ-rays and neutrinos. In principle, it should be possible to derive estimates or upper bounds on the flux of neutrinos from the observed γ-ray flux. However, as stated above, it must be taken into account that, according to the leptonic scenario, a component of the γ-rays flux is due to the Inverse Compton emission from electrons accelerated by the magnetic field ($\sim 10\mu$G). Shell-type SNR are expected to produce TeV neutrinos, whose detection would provide an unambiguous evidence for proton acceleration and hadronic emission from SNRs.

Another candidate galactic site for acceleration of hadrons beyond the knee (*Pevatron*) has been found in the *Cygnus* region by the MILAGRO collaboration (Atkins et al. [2005]). The multi-TeV γ-ray emission detected in this region is consistent with the flux

expected from a typical supernova remnant interacting with the interstellar medium. Therefore, this source is a good candidate for the production of high-energy neutrinos through proton-proton and proton-photon interactions.

Microquasars are galactic X-ray binary systems, characterized by relativistic radio jets, and candidate TeV neutrino sources. These objects are suspected to be baryonic accelerators up to ~ 10 PeV energies. The physical processes governing the formation of the accretion disk and the acceleration of nuclei in the jet are associated to an outburst of $\sim$TeV high-energy photons produced by photo-production of pions preceding the radio flares of the major ejection event. If such emission comes from hadronic processes, also high energy neutrinos are expected to be produced.

On the extragalactic side, the steeper energy spectrum requires a different acceleration mechanism. Numerous sites and models have been proposed as candidates for particle acceleration to energies beyond 10^{19} eV: the most plausible are Active Galactic Nuclei (AGNs) and Gamma-Ray Bursts (GRBs).

AGNs are compact regions located at the center of a galaxy, where a super-massive black hole (of $\sim 10^6$ to $\sim 10^{10}$ solar masses) accretes matter from the nucleus of the host galaxy. They are characterized by a TeV radiation in collimated jets of relativistic plasma, produced by the interaction of a relativistic baryonic outflow with the ambient medium or by the interaction of protons of extreme energy with the synchrotron photons produced by electrons spiraling in the jet magnetic field. In hadronic acceleration models, it can be assumed that for each class of AGN, the electromagnetic emission is correlated to a neutrino signal.

GRBs are cataclysmic events in which isotropic energies of the order of the solar mass ($M_\odot c^2 \sim 2 \times 10^{54}$ erg) are released in the form of a burst lasting only up to tens of seconds, making them the brightest events in the currently known Universe. The fireball model, currently the most widely accepted, assumes that in GRBs the large amounts of mass ejected by a central engine form successive plasma shells with typical Lorentz factors of $\Gamma = 100 - 1000$. Internal shock fronts form as the outer shells slow down and are hit by the inner shells, accelerating electrons and protons. Electrons are then cooled by synchrotron radiation, while protons can be accelerated up to energies as high as 10^{21} eV.

In such scenario, high-energy neutrinos are produced through the mechanisms described in Eq. 1.5 and Eq. 1.6, during the precursor event causing the GRB (when the jet is still forming and no electromagnetic radiation is escaping), during the explosion itself (prompt emission) and during the afterglow phase (when the shells run into the interstellar medium and external shocks are built up).

1.4   Detection strategies

During the past ten years, high-energy neutrino detectors have been improved in a way that currently makes it possible to cover five decades of energy. Today, some of the most optimistic models can already be used to constrain the physics of different astrophysical sources and in the next future the more realistic models are being challenged by the upcoming generation of neutrino detectors. A multimessenger connection between Cosmic Rays, photons and neutrinos of different wavelengths would be crucial in the pursuit of
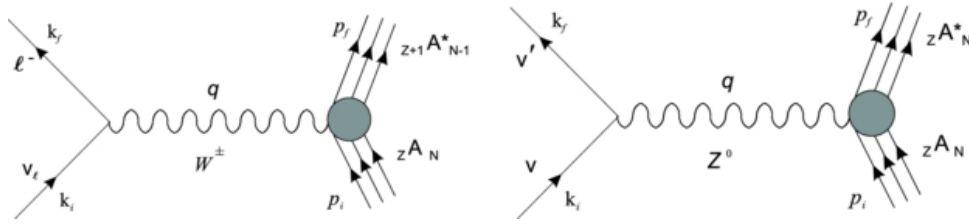
Figure 1.6: Feynmann diagrams of a ν_μ interacting with a nucleon N via CC (left) and NC (right) (Divari [2013]).

a deeper understanding of the fundamental processes driving non-thermal astrophysical sources. None of these messengers alone is able to give a complete picture.

Neutrinos are unique probes for the study of high-energy hadronic processes, however the advantages of excellent source pointing capability and unrivaled field of view are directly connected to the drawback of their very small interaction cross section.

Since neutrinos interact only through weak interaction, the number of processes that can be exploited for detection is relatively small. The most commonly used methods include the detection of secondary leptons, Cherenkov radiation or characteristic photons from secondary (annihilation) processes. The detection technique is dictated by the type of secondaries under analysis, while the size of the detector depends on the expected flux. They both depend on the energy range considered.

Cherenkov radiation

For high-energy astrophysical neutrinos, the currently most prominent detection technique consists in the detection of Cherenkov radiation in a transparent medium, such as ice or water. High-energy neutrinos impinging on the Earth can interact with a nucleon N of a nucleus either through a charged-current (CC) weak interaction:

$$\nu_l(\bar{\nu}_l) + N \to l(\bar{l}) + X \tag{1.14}$$

or through a neutral-current (NC) weak interaction:

$$\nu_l(\bar{\nu}_l) + N \to \nu_l(\bar{\nu}_l) + X, \tag{1.15}$$

where l is a lepton and X represents the hadronic remnants of N, that gives rise to hadronic showers. The CC reactions are weak interactions where a $W^\pm$ boson is exchanged and charged particles are created, while in NC interactions a Z^0 boson is exchanged, with the production of neutral particles (see Fig. 1.6). CC interaction cross sections are always larger than the corresponding NC interactions (NC cross section is about one third of the CC cross section). All flavors of neutrinos participating in NC interactions create hadronic showers, while for CC interactions the signature left by the charged lepton l depends on its flavor. Since the mass of electrons is considerably low compared to muons and taus, the favored energy loss process is Bremsstrahlung. Therefore, instead of leaving a track, electrons produce an electromagnetic shower. In contrast, high energy $\mu^{+/-}$ and $\tau^{+/-}$ travel longer distances before decaying, so they undergo only radiation losses and leave track-like signatures. Due to their long lifetime, the propagation track of the muon always extends beyond the shower. This makes possible the reconstruction of the track, providing directional information about the origin of the neutrino,
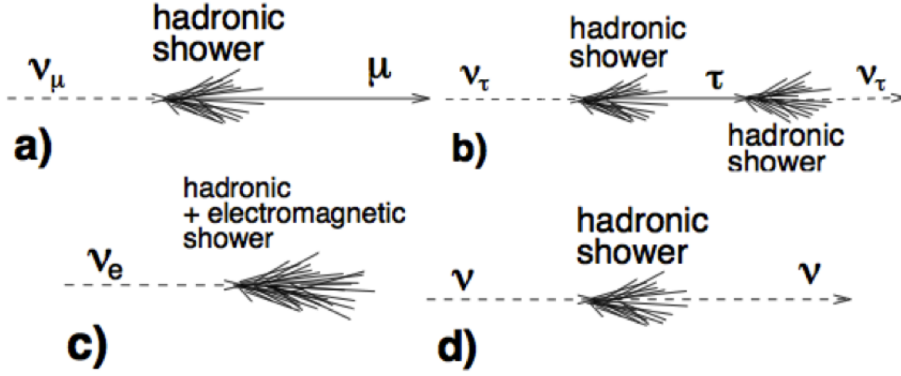
Figure 1.7: The signatures for the different types of neutrino interactions: a) muon hadronic shower produced by μ_ν CC interaction; b) double bang signature of a ν_τ CC interaction generating an hadronic shower, a second τ and a secondary hadronic shower; c) ν_e CC interaction producing both an electromagnetic and a hadronic shower; d) hadronic shower produced by a NC interaction.

with a resolution depending on the medium and on the kinematics of the interaction. For these reasons, muon neutrinos are particularly suitable for a good reconstruction in ice or water Cherenkov telescopes.

On the other side, the relatively short lifetime of tauons makes them show a very distinct signature. Indeed, tauons decay to 70% into hadronic channels, however for energies below a few PeV their decay path is short enough to produce a second hadronic shower, generating a further τ. In such conditions, it is not possible to distinguish the decay of the tau from the hadronic shower. On the contrary, if the energy of the tauon is higher than 1 PeV, it can travel several meters before decaying in a second shower (the so-called *double bang*). Under these conditions, tau cascades are reproduced within the Earth until the shower comes out of the Earth, while hadronic or electromagnetic air showers do not traverse the high column density. For this reason, tau cascades are particularly suitable for investigation of horizontal neutrino air showers. A detection with either an Imaging Air Cherenkov Telescope or an air-shower surface array is possible. For example, this approach is followed by the AUGER experiment in the case of surface arrays and by the MAGIC experiment in the case of IACTs (Fargion [2006]).

In Fig. 1.7, the signatures of the event topologies for the different types of neutrino interactions are shown. Several detectors are based on the effects of the propagation through a transparent medium to detect indirectly the high energy neutrino via its out-coming charged lepton. For both NC and CC reactions, the final state lepton follows the initial neutrino direction with a mean square root mismatch angle θ decreasing with the square root of the neutrino energy (Katz and Spiering [2012]):

$$\sqrt{\langle \theta^2 \rangle} \approx \frac{1.5°}{\sqrt{E_\nu[TeV]}}, \tag{1.16}$$

a resolution that is slightly worse than typical resolutions of high-energy γ-ray astronomy and orders of magnitude worse than those reachable by conventional astronomy.

If the lepton travels faster than the speed of light in a medium with index of refraction n, the atoms along the path of the particle track are first polarized and then relax rapidly
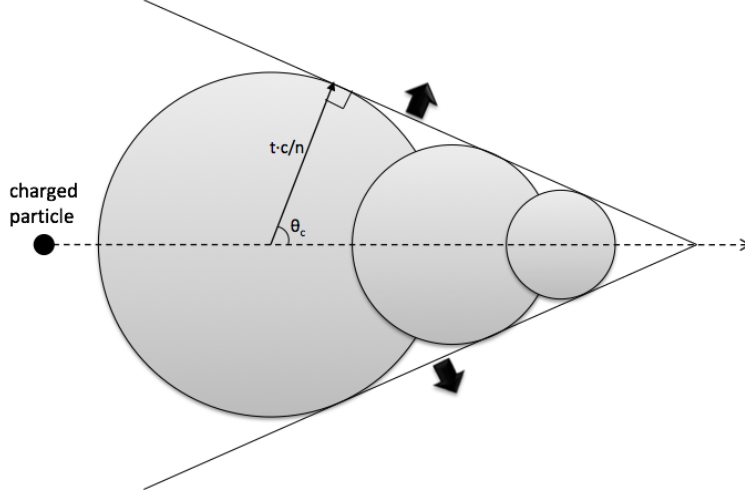
Figure 1.8: Cherenkov cone generated by a charged particle traveling faster than the speed of light in a medium.

leading to radiation. The light emitted by the excited molecules interferes positively, thus creating a light shock front. This kind of coherent photoemission is called *Cherenkov light*. The wave front forms a cone with apex coincident with the traveling particle and a characteristic opening half-angle θ_c given by the relation:

$$cos\theta_c = \frac{1}{\beta n}, \tag{1.17}$$

where $\beta = \nu/c$ and n depends on the frequency ν of the emitted photons, $n = n(\nu)$ (see Figure 1.8). For $\lambda = 550 nm$ the index of refraction for water is $n \approx 1.33$, therefore the average Cherenkov angle is $\theta_c \approx 43°$. The spectral distribution of Cherenkov photons per path length of an emitting particle with charge $\pm Ze$ is given by

$$\frac{dN}{dxd\lambda} = \frac{2\pi Z^2 \alpha}{\lambda^2} \cdot \left(1 - \frac{1}{\beta^2 \cdot n^2}\right) \tag{1.18}$$

where α is the fine structure constant. The energy loss per path length is therefore given by:

$$-\left(\frac{dE}{dx}\right) = \frac{2\pi z^2 \alpha h}{c} \int_{\beta \cdot n(\nu) \geq 1} \nu \left(1 - \frac{1}{\beta^2 \cdot n^2(\nu)}\right) d\nu. \tag{1.19}$$

This means that in the wavelength band $300 - 500\ nm$ a single charged particle emits approximately 3.5×10^4 photons per meter along the track in water.

Considering the case of under-water/under-ice neutrino telescopes, even though the production of the charged leptons is possible for all three flavors, generally only the tracks of muons are measured. This is due to the relatively long life time of the muons (compared to taus) and their ability to polarize the medium efficiently (compared to electrons), leading to a clear Cherenkov signal at energies $E_\nu \geq 100$ MeV.

An alternative approach based on the Cherenkov effect is the *Ring Imaging Cherenkov detection*. Over the last few decades, several neutrino and nucleon decay experiments

have been based on this technique, like Kamiokande (1983-1996, 3 kiloton) and Super-Kamiokande (in operation since 1996, 50 kiloton), that achieved many important scientific results, among which the most relevant are the discovery of neutrino oscillations and the current limits on neutrino mass.

The Ring imaging Cherenkov technique consists in the detection of the spatial and timing distributions of the Cherenkov photons with an array of photodetectors, in order to reconstruct position, direction and energy of the relativistic charged particles generated by neutrino interactions. This approach makes possible to discriminate charged muons ($\mu^{\pm}$) from electrons, positrons, and gammas. Indeed, these particles induce electromagnetic showers in the medium and hence are characterized by a different signature, with modified resulting ring patterns.

Ring Imaging Cherenkov detectors have excellent particle identification capabilities, with a good rejection efficiency for π^0 background. These features make possible to determine neutrino flavor compositions in both atmospheric and accelerator neutrinos and hence to achieve an excellent neutrino flavor oscillations detection capability.

Fluorescence

Several cosmic ray observatories rely on a completely different approach, based on the measurement of the conversion of energy from a CR shower into fluorescence.

This technique has proved to be extremely suitable for the detection of UHECRs. When a high energy Cosmic Ray collides with the Earth's atmosphere, it initiates a shower of secondary particles. The charged particles of this shower, mainly electrons and positrons, lose energy by inelastic collision with air molecules that in turn are excited and subsequently relax to the ground state partially by emitting radiation. The primary source of atmospheric fluorescence consists of molecular bands of the Second Positive (2P) system of N_2 and the First Negative (1N) system of N_2^+. In this case, the excitation energy is emitted isotropically in the form of visible and in the near-UV region between 300 and 400 nm.

Under the assumption that the fluorescence emission is proportional to the energy deposited by the shower, this technique can provide an estimate of the primary Cosmic Ray energy using the atmosphere as a calorimeter. Indeed, using imaging telescopes sensitive to UV light, it is possible to observe the longitudinal profile of the shower and therefore to estimate the number of charged particles in the shower.

The key parameter in this kind of approach is the so-called *fluorescence yield* (Y), defined as the number of photons fluoresced by an electron passing through one meter of air:

$$Y = \frac{N_\gamma}{N_e L}, \tag{1.20}$$

where N_γ is the number of emitted photons and N_e is the number of electrons that passed through a line of atmosphere of length L. Therefore, in the case of a purely electromagnetic shower, measuring the number of fluorescent photons makes possible to determine the number of electrons and hence the energy of the shower according to the following relation:

$$E_{em} = \frac{E_c}{X_0} \int_0^\infty N_e(X) dX, \tag{1.21}$$
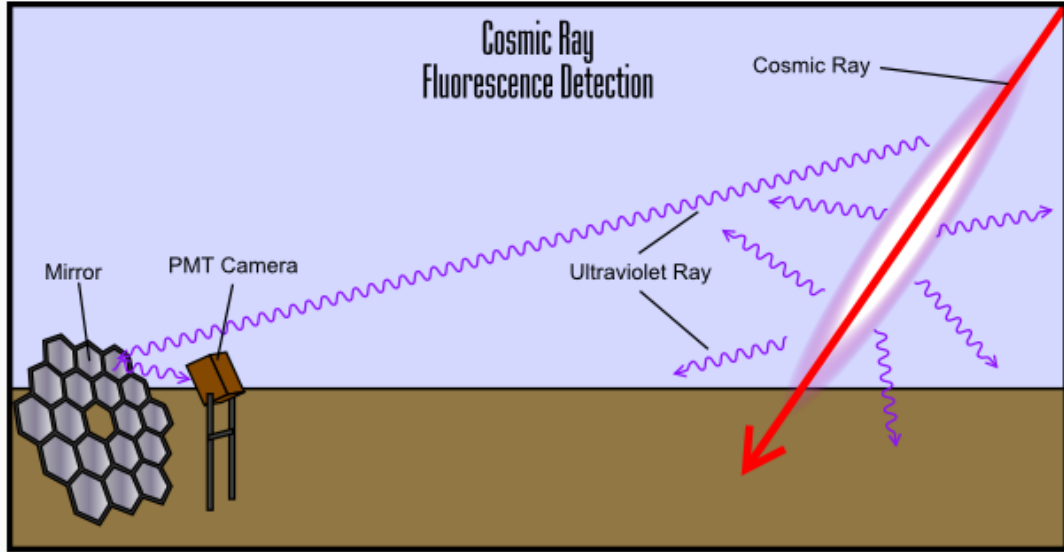
Figure 1.9: Fluorescence Telescopes working principle (http://www.telescopearray.org).

where X_0 is the electron radiation length in air and E_c is the critical energy of an electron in air.

Currently, the main systematic uncertainty in the determination of the energy of Cosmic Rays using this technique arises from the uncertainty in the fluorescence yield. Accurate measurements of this crucial parameter, as well as its dependence on atmospheric parameters (like pressure, temperature and humidity), started since the 1960s and are still ongoing, confirming the hypothesis that Y, up to some tens of MeV, is proportional to the energy deposit of the particle, dE/dX.

In the experiments based on the fluorescence technique, the fluorescence photons are collected using a lens or a mirror and imaged onto a camera located at the focal plane. The camera is typically composed by an array of photosensors that "pixelizes" the image, recording the arrival time and the number of photons on each pixel element (see Fig. 1.9). The main disadvantage of this technique is that fluorescence telescopes can operate only during clear moon-less nights ($10 - 15\%$ duty cycle). Therefore, a continuous monitoring of the atmospheric conditions, in particular the detection of clouds and aerosols, is required.

Chapter 2

Photon detectors in astroparticle physics

Photodetectors are indispensable in many areas of fundamental physics research, particularly in the Cherenkov experiments described in the previous chapter.

In general, a photodetector is a device that converts the energy of an absorbed photon flux into a measurable form (Saleh and Teich [1994]). Based on their operating principle, photodetectors can be broadly divided into three major categories:

- **thermal detectors**, whose operating principle is based on the conversion of photon energy into heat. There is no wavelength dependence, however rather low sensitivities and relative long time required to change their temperature make thermal detectors not suitable for most applications in photonics;

- **external photoelectric effect detectors**, in which the electrons generated by photoelectric effect are emitted into the vacuum, escaping from the material as free electrons;

- **internal photoelectric effect detectors**, based on the absorption of photons by some materials, typically semiconductors, resulting in electronic transitions to higher energy levels and consequently in the generation of mobile charge carriers. In such devices, the excited carriers remain within the material producing a measurable electric current.

The photoelectric effect was discovered by Hertz in 1887 (Hertz [1887]) during experiments with a spark-gap generator, in which he found an increase of the sensitivity by illuminating it with visible or ultraviolet light. The discovery was conclusively confirmed one year later by Wilhelm Hallwachs, however neither of the two was able to offer any theory of what had been experimentally observed.

According to the classical maxwellian wave theory of light, the kinetic energy of ejected electrons is determined by the amplitude of the incident photon flux. In contrast, in 1902 Lenard found a dependency of the electron energy on the frequency of the light (Lenard [1902]).

This paradox was finally resolved by Albert Einstein in 1905 (Einstein [1905], Nobel Prize in 1921), who for the first time assumed that *"the energy of a light ray spreading out from a point is not continuously distributed over an increasing space, but consists of a finite*
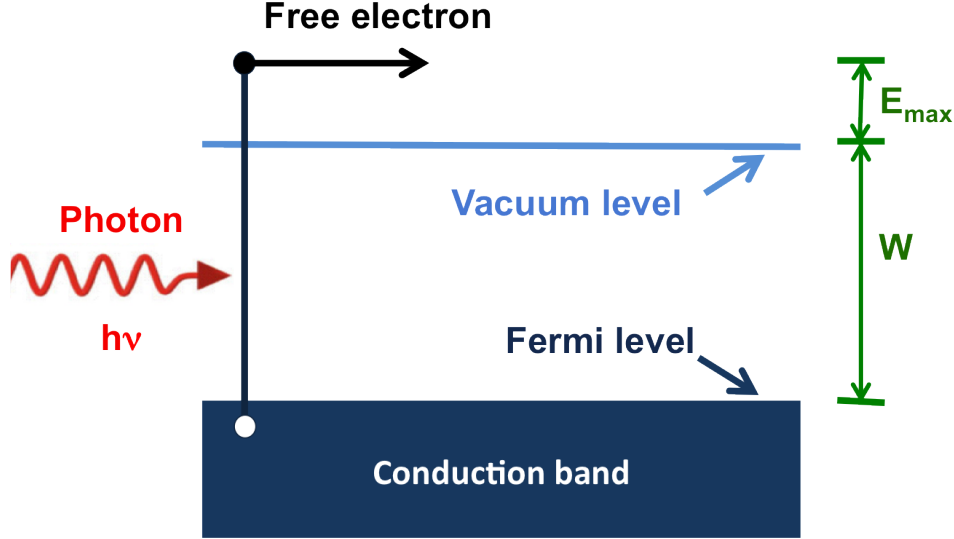
Figure 2.1: Photoelectric emission from metals.

number of energy quanta which are localized at points in space, which move without dividing, and which can only be produced and absorbed as complete units".

The radiation itself consists of quanta of energy $E = h\nu$, interacting with the electrons in the illuminated material like discrete particles, rather than as continuous waves. When photons strike a metal or a semiconductor, electrons absorb photon energy and become excited, diffusing toward the surface of the material. If the diffused electrons have enough energy to overcome the vacuum level barrier, they are emitted into the vacuum as photoelectrons. The fraction of emitted photoelectrons over the total number of photons impinging on the material is called *Quantum Efficiency* (η).

In the case of metals, photons in the visible band are in a large part reflected and thus lost to the photoemission process. Moreover, the generated photo-electrons rapidly lose their energy in collisions with the large number of free electrons in the metal through electron-electron scattering. This means that only a small fraction of electrons are able to reach the surface of the metal with sufficient energy to overcome the surface barrier. As a result of high reflectivity and very small escape depth of electrons ($\sim$ 1nm), the quantum efficiency for metals in the visible region is very low, typically of the order of $\sim 0.1\%$.

The maximum kinetic energy of photoelectrons for an incident photon flux of frequency ν is given by:

$$E_{max} = h\nu - W \tag{2.1}$$

where the work function W is the energy difference between the vacuum level and the Fermi level of the material, see Fig. 2.1. The work function represents the energy threshold for photoemission process to occur in materials: visible photons with energies less than W are prevented from producing photo-electrons. Typical working function values for pure metals are of the order of few eV (see Fig. 2.2). Only for a few metals (the alkali ones) the values of W are low enough to make them sensitive to visible light. In particular, Cesium has the lowest work function of all metals (about 2 eV), making it widely used in optical detectors based on the external photoelectric effect.
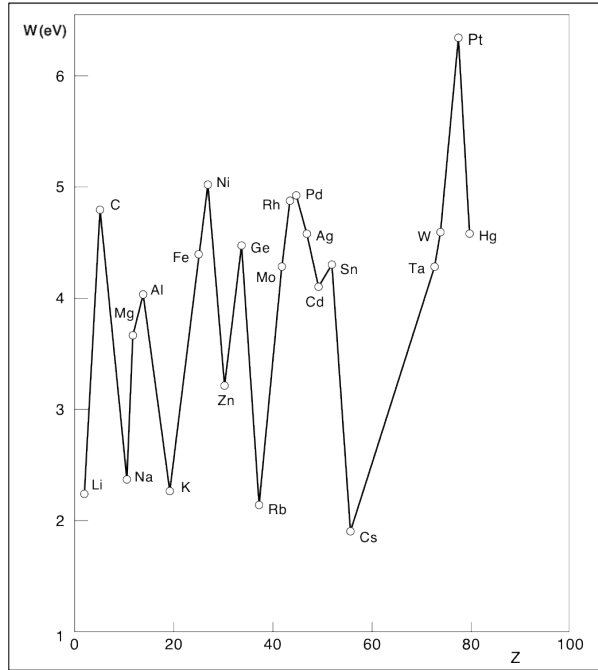
Figure 2.2: Work function for pure metals

In the case of semiconductors, photoelectrons are usually released from the valence band, where electrons are plentiful. In this case, the energy loss by electron-electron scattering is relatively low because very few free electrons are present. Therefore, the predominant energy loss mechanism is the scattering by phonon. As a result, for semiconductors the escape depth is much greater than in metals, typically of the order of tens of nanometers. The maximum kinetic energy is given by:

$$E_{max} = h\nu - (E_g + \chi), \tag{2.2}$$

where E_g is a forbidden-band gap (or energy gap) that cannot be occupied by electrons and χ is the electron affinity of the material, defined as the energy difference between the vacuum level and the bottom of the conduction band (see Fig. 2.3). In order to be sensitive to the visible light, the sum $E_g + \chi$ must be less than 3.25 eV (less than 1.6 eV to cover the whole visible region up to 780 nm). This condition is fulfilled only in some complex semiconductors. For certain materials, as NaKCsSb, the energy $E_g + \chi$ can be as low as 1.4 eV, thus obtaining longer threshold wavelengths with respect to those of any pure metal. Therefore, these materials are particularly suitable for operation in the near infrared as well as in visible and ultraviolet. Moreover, compared to metals, semiconductors have also lower reflection coefficients, thus absorbing a much higher fraction of the incident light. For all these reasons, semiconductors have a significantly higher quantum efficiency with respect to metals in a significantly wider wavelengths range. Typically, quantum efficiencies of tens of percents are achieved.

A significant improvement in the photoemission from semiconductors has been achieved with the development of negative-electron-affinity semiconductors, enhancing the probability that the electrons reach the surface of the material even for longer wavelengths with lower excitation energy. In this way, an escape depth as much as 100 times greater than
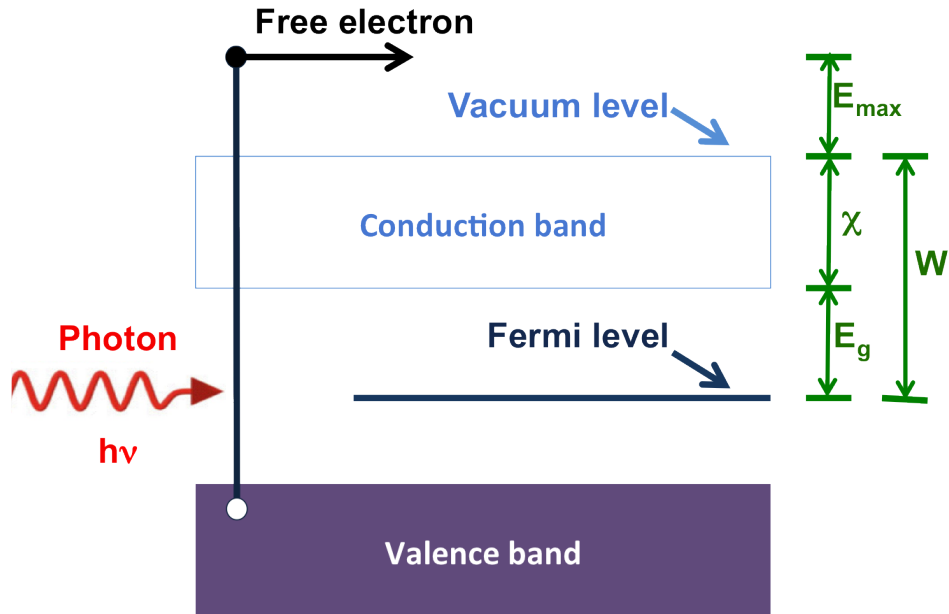
Figure 2.3: Photoelectric emission from semiconductors.

for standard materials is obtained, with the possibility to have an observable response even for photons with energies close to that of the band gap, where the absorption is weak. All this implies that a much higher photosensitivity is achieved.

Typically, the reduction of the electron affinity is obtained by means of a two steps process. In the first one the semiconductor is strongly p-doped, in order to shift all the energy levels towards lower values, although keeping the relative distances unaltered (see Fig. 2.4). The second step consist in depositing on the p-doped semiconductor a surface film of electropositive materials, typically Cesium. The atoms in this layer become polarized or ionized (through loss of an electron to a p-type energy level near the surface of the semiconductor) with their positive poles directed towards the vacuum and, therefore, acting as a surface dipole (see Fig. 2.5).

2.1 Photomultiplier Tubes

PhotoMultiplier Tubes (PMTs) are, by far, the most widely used photon detectors in all the fields of fundamental physics research.

The basic principle of this technology dates back to the beginning of the last century and still holds, more or less unaltered, in today's devices. However, in the last decades PMT technology has known a whirling evolution: new solutions have been developed, new materials have been introduced, new geometries have been realized. Today, PMTs have dimensions ranging from a few mm² up to 20 inches, with efficiencies optimized in a wide wavelength range, thus providing a valid solution in most of current applications. PMTs are vacuum photodetectors based on the external photoelectric effect. Schematically, a PMT is composed by a photoemissive material (called photocathode) where photoelectrons are generated, an electron multiplier system made of a dynode chain and an anode for electron collection, see Fig. 2.6. The photoelectrons emitted by the photo-
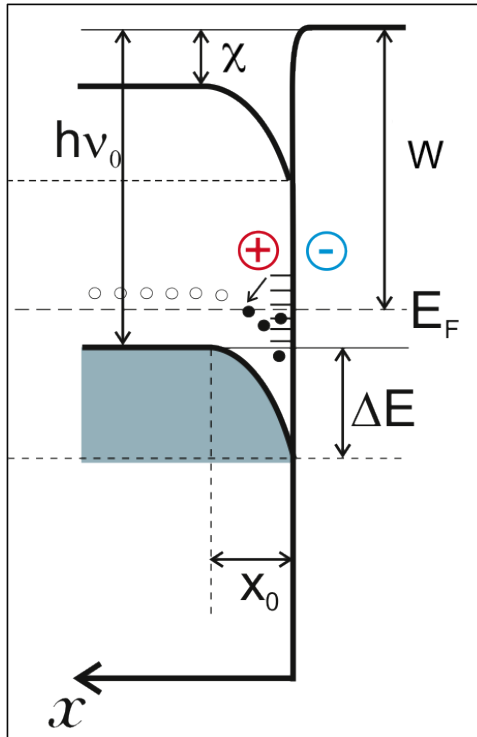
Figure 2.4: P-doped semiconductor.
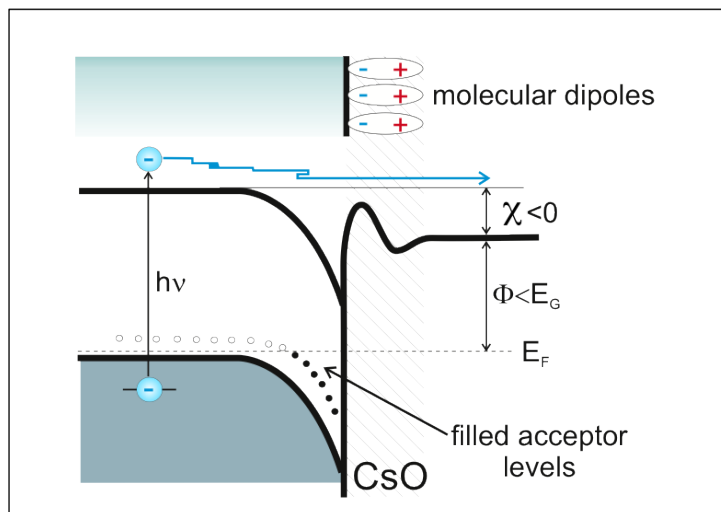
Figure 2.5: Semiconductor energy-band model showing negative electron affinity.

35
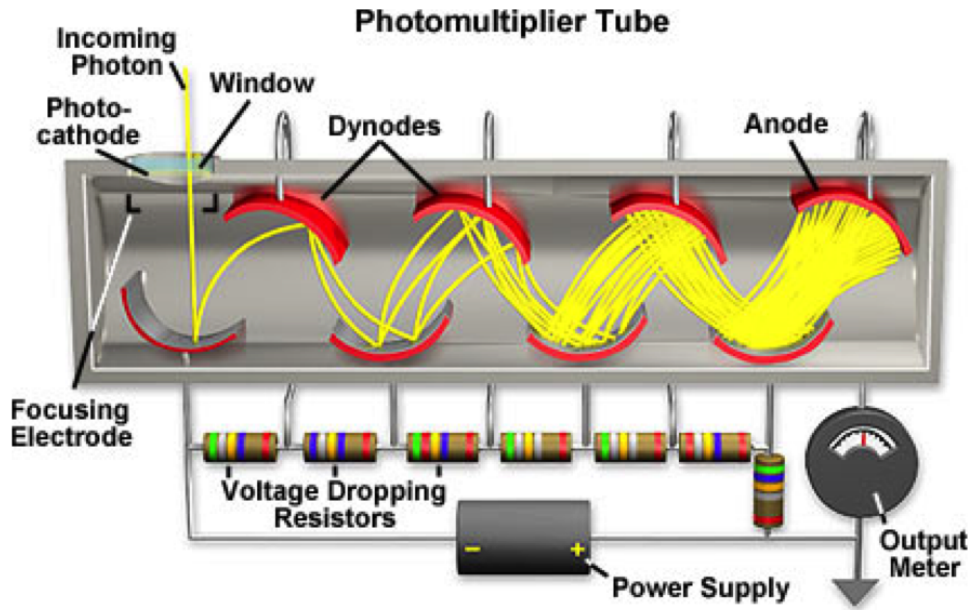
Figure 2.6: Schematic view of a PMT.

cathode are accelerated and focused by a focusing system towards the first dynode where they are multiplied by means of secondary electron emission. This secondary emission is then repeated for the successive dynodes, providing an electron multiplication factor ranging approximately from 10 to 10^2 at each step. The electron current multiplied in the cascade process through multi-stage dynodes, proportional to the incident photon flux, is then collected by the anode, kept at a high electric potential.

Since the realization of the first photomultiplier tube by Elster and Geitel in 1913, PMT technology has known decades of incessant progresses. Compound photocathodes were discovered, providing photoelectric sensitivities several orders of magnitude higher than previously used photocathode materials and achieving high sensitivity in a very wide range of wavelengths.

In 1935, Iams et al. (Iams and Salzberg [1935]) realized a triode photomultiplier tube with a photocathode combined with a single-stage dynode, while in 1936, Zworykin et al. (V.K. Zworykin et al. [1936]) developed the first PMT with multiple dynode stages. Three years later, in 1939, Zworykin and Rajchman (Zworykin and Rajchman [1939]) realized an electrostatic-focusing type photomultiplier tube, having the basic structure of all current PMTs (Hamamatsu-Photonics [2006]).

Photocathodes are traditionally classified by photoelectron emission process into a reflection mode and a transmission mode. In reflection mode photocathodes, usually made of a metal plate, the direction of emitted photoelectrons is opposite to the direction of the incident light. Conversely, transmission mode photocazzodes are usually deposited as a thin film on an optically transparent glass plate and photoelectrons are emitted in the same direction as that of the incident light.

Most transmission photocathodes are made of compound semiconductors consisting of alkali metals with a low work function or based on the combination of two or more kinds of alkali metals (bialkali and multialkali photocathodes, respectively) (Hamamatsu-Photonics [2006]).

The electron focusing system plays the critical role of optimizing the collection efficiency of photoelectrons and secondary electrons on the dynodes while keeping the electron transit time spread as small as possible. The collection efficiency of a dynode is defined as the ratio of the number of electrons impinging on its effective area to the number of (photo)electrons emitted at the previous stage, with typical values going from about 80% to more than 90%.

The dynodes are usually made of secondary emissive materials like alkali antimonide, Beryllium Oxide (BeO), Magnesium Oxide (MgO), Gallium Arsenide (GaAs) and Gallium Arsenide Phosphide (GaAsP), coated onto a substrate electrode made of nickel, stainless steel, or copper-beryllium alloy (Hamamatsu-Photonics [2006]).

2.1.1 PMT characteristics

PMTs have many attractive features, making them represent a unique solution in many application fields over the last decades. However, besides outstanding performances such technology suffers of some intrinsic drawbacks that will seriously limit their application, especially in the next generation of experiments.

First, the performances of PMT photocathodes show a strong dependance on the wavelength of the incident photon flux. Such dependence is referred to as the *spectral response* of the photocathode and is typically expressed in terms of radiant sensitivity and quantum efficiency (η), defined as the photoelectric current generated by the photocathode divided by the incident radiant flux at a given wavelength and as the number of photoelectrons emitted from the photocathode divided by the number of incident photons, respectively.

Given a photon striking with incident energy $E = h\nu$ on the surface of a photocathode, characterized by a reflection coefficient R and by an absorption coefficient k, the quantum efficiency can be expressed in probabilistic terms as (Hamamatsu-Photonics [2006]):

$$\eta(\nu) = (1 - R)\frac{P_\nu}{k}\left(\frac{1}{1 + 1/kL}\right)P_S, \qquad (2.3)$$

where P_ν is the probability that light absorption may excite electrons to a level greater than the vacuum level, P_S is the probability that electrons reaching the photocathode surface may be released into the vacuum and L is the mean escape length of excited electrons.

Gain

Dynodes are characterized by a parameter called *secondary emission ratio* (δ), defined as the number of secondary electrons emitted per primary electron. Therefore for the first dynode, indicating with I_k the photoelectron current striking it and with I_{d1} the secondary electron current emitted, the secondary emission ratio is given by:

$$\delta_1 = \frac{I_{d1}}{I_k}. \qquad (2.4)$$

In general, for the *n-th* dynode the secondary emission ratio δ_n can be expressed as:

$$\delta_n = \frac{I_{dn}}{I_{d(n-1)}}, \qquad (2.5)$$

where I_{dn} and $I_{d(n-1)}$ are the emitted and the impinging current of the $n-th$ dynode, respectively. Therefore, the overall current amplification of a PMT, called *gain*, is given by:

$$G = \alpha \cdot \delta_1 \cdot ... \cdot \delta_n, \qquad (2.6)$$

indicating with α the collection efficiency of the device.

In a PMT the gain is susceptible to variations in the high-voltage power supply, such as drift, ripple, temperature stability, input regulation and load regulation (Hamamatsu-Photonics [2006]). Fluctuations of the gain, and in particular the fluctuations of first dynode gain, seriously affect the photon counting capabilities of the device. Indeed, the number of secondary electrons released from the first dynode is not constant, with a broad probability approximable as a Poisson distribution. This is repeated through the second and subsequent dynodes until reaching the anode. Therefore, each output pulse obtained at the anode exhibits a certain distribution in pulse height because of statistical fluctuations due to cascade multiplication, non-uniformities of multiplication depending on the dynode position and electrons deviating from their favorable trajectories.

Typically, in large-scale Cherenkov experiments PMTs detect no more than few photons per event. Therefore, the single photoelectron response is crucial in determining the detector's response and the capability to discriminate different particle types and reconstruct particle positions, directions and energy (Brack et al. [2013]).

The single photoelectron regime corresponds to very low incident light levels conditions, in which no more than two photoelectrons are emitted within the time resolution of the PMT. In this case, although all events start with a single photoelectron, the statistical nature of PMT gain makes anode pulses vary in magnitude from one pulse to another. In Fig. 2.7 a typical PMT pulse height distribution in single photon condition is represented. It is called the Single Electron Response (SER) of the PMT and corresponds to the histogram of the time integral of anode output pulses, where the abscissa indicates the pulse height. The main peak is given by the sum of the contributions of signal and dark current pulses, originating from thermal electron emission at the photocathode and at the dynodes. The thermal electrons from the dynodes are multiplied less than those from the photocathode and are therefore distributed in the lower pulse height region. On the other side, the pedestal is due to electronic noise. The height of the main peak relative to the depth of the valley between the SPE pulses distribution and the pedestal is an indicator of the PMT's ability to distinguish true photons from electronic noise. A large Peak-to-Valley ratio means a low number of real photons occasionally producing low charges (populating the valley region of the SER together with upward fluctuations of the electronic noise) and hence a higher overall detection efficiency (Brack et al. [2013]). The high charge tail includes the contribution of multiple photoelectrons. The size of the tail, coupled with the width of the charge distribution, affects the PMT's ability to distinguish between single and two or more photons. In particular, even for slightly higher light levels (from 4 or 5 photoelectrons on), the peaks of multiple photons start to be completely superimposed to each other thus highlighting very bad photon counting performances of PMTs.
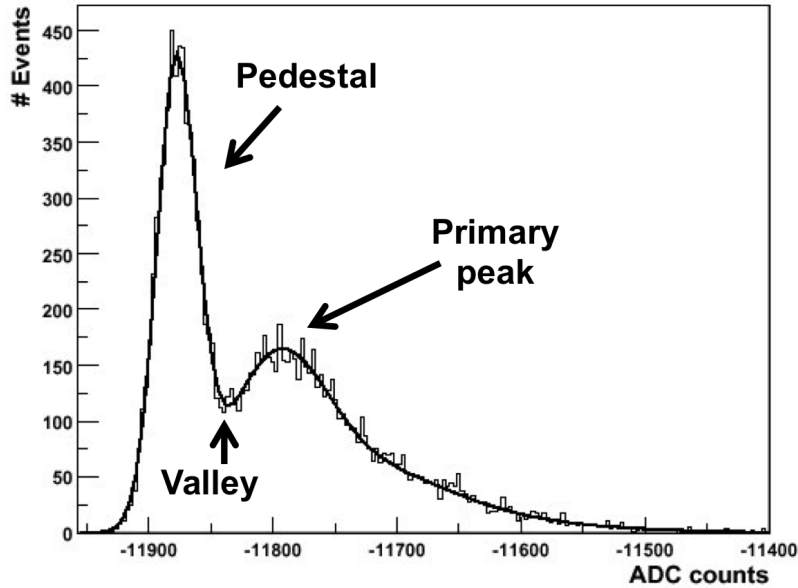
Figure 2.7: Typical Single Electron Response of a PMT.

Linearity

PMTs exhibit a good linearity in anode output current ranging from single photon condition to higher incident light levels, up to few hundreds of photons. In general, deviations from linearity are observed in correspondence to large amounts of incident light and are primarily caused by both anode and cathode linearity characteristics (Hamamatsu-Photonics [2006]). Indeed, for intense light pulses a large current flows in the latter dynode stages, increasing the space charge density and causing current saturation. The extent of these space charge effects depends on the dynode structure as well as on the electric field distribution and intensity between each dynode. Typically, in order to get a high output pulse current the voltage gradient between the anode and the last dynode is much higher than between dynodes. In this cases an accelerating grid between the last dynode and the anode is used, reducing the effects of space-charge limiting.

However, deviations from linear behavior can be obtained for PMTs even at low current levels, due to field non-uniformities and charge patterns on the insulator spacers in proximity of the ceramic end-plates.

Both cathode and anode linearity characteristics are dependent only on the incident light level if the supply voltage is constant, while no significative dependence on the incident light wavelength is observed. For PMTs a strong connection between linearity and gain holds. In general, any dynode type provides better pulse linearity when the supply voltage is increased, therefore the linearity increases with gain (see Fig. 2.8).

Stability

The output variation of a PMT with operating time spanning over periods longer than $\sim 10^3$ hours are referred to as the *life characteristics*.

The cathode sensitivity of a PMT exhibits good stability even after long periods of operat-
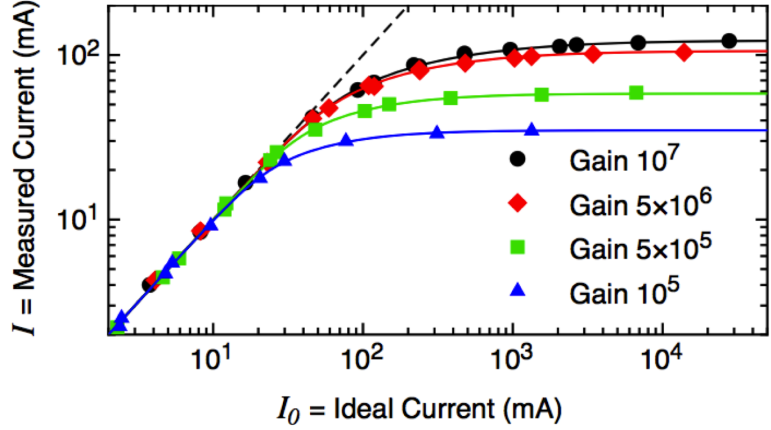
Figure 2.8: PMT linearity as a function of gain (Abbasi et al. [2010]).

ing time, therefore the life characteristics primarily depend on variations in the secondary emission ratio. In particular, PMT operating instabilities occur as an increasing fatigue effect, depending mainly on the magnitude of the average anode current, dynode materials and operation modes.

All PMTs have a maximum anode current rating, in order to limit space charge and fatigue effects, as well as power dissipation. In this case, the loss in sensitivity occurs as a result of a reduction in the secondary emission, particularly in the last stages of the photomultiplier where the currents are the highest. In general, a low current level operation produces less fatigue effects and in many cases can help to restore sensitivity losses produced by high-current operations.

Also dynode materials play a key role in PMT stability. Indeed, for cesium antimony dynode types, during periods of heavy electron bombardment, erosion of the cesium on dynode surface can occur, with the subsequent deposition on other areas within the PMT and, as a consequence, with a decrease in the overall sensitivity of the device. However, such sensitivity losses can be reversed during non-operation periods, when the cesium may again return to the dynode surfaces (Hamamatsu-Photonics [2006]). The sensitivity loss rate is lower during the initial operations and significantly increases after the tube has been in use for some hours, see Fig.2.9.

In addition to the life characteristics, also changes of a temporary nature can occur, usually referred to as *drift*. The drift characteristics depend on gain variations over short time scales and are linked to variations in the secondary emission ratio. In particular, such short timescale sensitivity losses could be caused by increases in the charge flow, causing insulator spacers to charge to a new potential, with the subsequent modification of inter-dynode potential fields. Drift per unit time generally improves with longer operating time and this tendency continues even if the PMT is left unused for a short time after operation. Aging or applying the power supply voltage to the photomultiplier tube prior to use can help to provide a more stable operation.
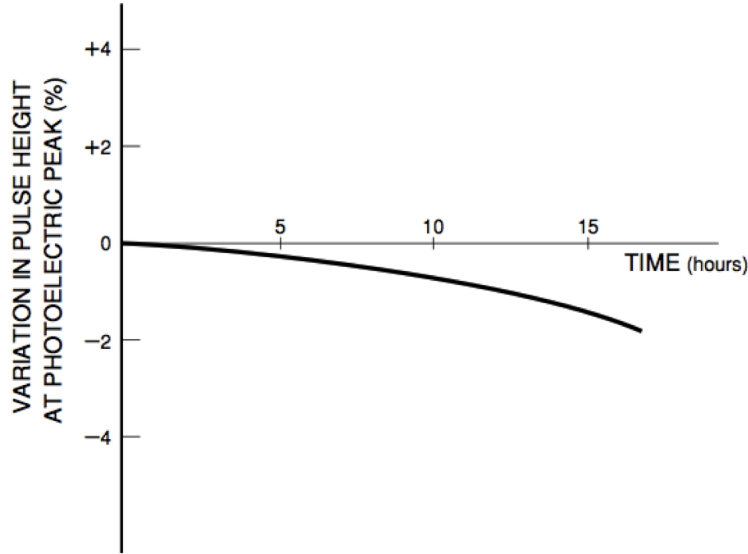
Figure 2.9: Typical PMT life characteristics (Hamamatsu-Photonics [2013]).

Transit Time Spread

Transit time (TT) is a key parameter in PMT performances. It is defined as the time for the current pulse to pass from cathode to anode in conditions of photocathode uniformly illuminated with single photons. The Transit Time Spread (TTS) represents statistical fluctuations in TT, introducing some limitations in the form of time resolution and pulse shape distortion. The TTS is defined as the standard deviation σ of transit time distribution, with typical values ranging from few to few tens of nanometers. Sometimes the TTS is expressed in terms of the FWHM of the distribution, equal to $\sim 2.35\sigma$.

The main contribution to TTS is given by the spread in the electron path length. For example, in a planar photocathode design the transit time is longer for edge illumination than for central regions because of the longer edge trajectories and the weaker electric field near the edge of the photocathode. However, even in a spherical geometry the transit time is slightly longer for edge trajectories than for axial trajectories because of the weaker electric field at the edge. Additional causes are also the spread in emission velocities, and (more weakly) in emission time, of the secondary electrons. Initial-velocity effects are the major limitation on the time response of the electron multiplier, due to the relatively high energy spread of secondary electrons compared to that of photoelectrons. The multiplier time response can be improved by increasing the supply voltage or the electric field intensity and adopting optimized dynode geometries. In general, the time response improves in inverse proportion to the square root of the supply voltage. Even the choice of materials affects the time performances of the dynode chain. Indeed, the advantage of a high-gain material (like GaAsP) is that the number of stages, and thus the total transit time, may be reduced, thus reducing also the energy spread of secondary electrons.

Other possible contributions to TTS are given by the variation of photoelectron emission velocities with wavelength ($v \propto \lambda^{-1/2}$) and by space charge effects.

41

Additional PMT drawbacks

PMTs are strongly sensible to external magnetic fields. Indeed, under the effect of a strong magnetic field photoelectrons and secondary electrons deviate from their normal trajectories, affecting both photoelectron collection efficiency and electron multiplier gain. This effect is critically dependent on focusing geometry and electron multiplier layout. However, it is possible to minimize it by using a mu-metal shield extending from the rear of the PMT to a distance of roughly half the diameter beyond the photocathode.

It is important to avoid using the PMTs beyond the maximum recommended high voltages. Indeed, in such cases some strong feedback effects may arise, resulting in unstable performances, high dark currents and possible permanent damages due to electrical breakdown under extreme conditions.

Moreover, PMTs are strongly sensitive to daylight, even in non-operational conditions. The exposure of the photocathode to normal light levels causes the excitation of photocathode, damage of the tube and increase of dark current level of up to an order of magnitude.

Finally, PMTs exhibit a high failure risk due to shocks and vibrations. In particular, shocks can give rise to photocathode damage and electrical connection failure, while vibrations can critically affect the internal structure of the device and produce loose materials which in turn can accumulate and cause internal short circuits. At the anode, shocks and vibrations can cause changes in electrode capacitance due to the movement of electrodes, manifesting as microphony.

2.2 Semiconductor photodetectors

As shown previously, PMT technology provides unique performances, specially in terms of high gain and wide bandwidth, making it the leading solution in practically all the applications based on photon detection. However, it suffers of some critical drawbacks described in the previous section and summarized as follows:

- difficult *photon counting*, due to fluctuations in the first dynode gain;

- reduced *linearity*, gain dependent;

- large *transit time spread*;

- complex and expensive *machanical structure*;

- *external magnetic fields* dependence;

- need of *voltage dividers*, increasing failure risks, complexity in the experiments designs and power consumption.

Such limits are something intrinsically correlated to PMT technology and in most cases are linked to the dynode chain, responsible of the electron multiplication stage. In the last years much effort has been done in order to overcome them and many improvements have been obtained, especially for what concerns quantum efficiency, gain and materials. However, due to the described features, todays PMTs cannot be considered as optimal
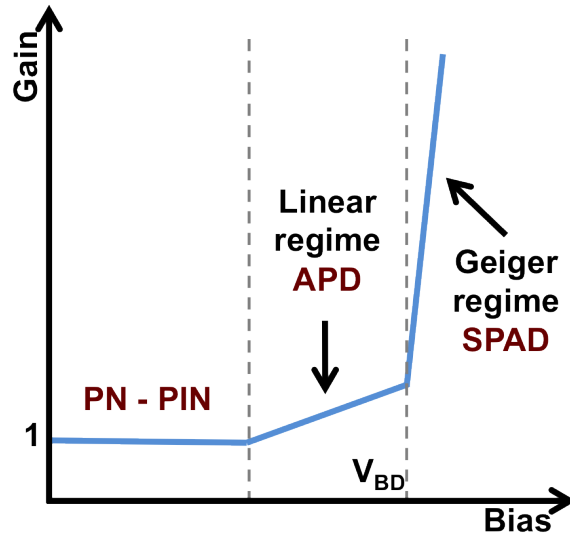
Figure 2.10: Gain regimes vs applied Bias.

solutions for the next generation of experiments aimed at the study of very high-energy (GRB, AGN, SNR) or extremely rare phenomena (dark matter, proton decay, zero neutrinos double beta decay, neutrinos from astrophysical sources) and based on photon detection. In such applications a radical improvement of photon detectors performances is required, especially in terms of linearity, gain, and photon counting capability.

In the last decades, some alternatives to PMTs, mainly concentrated on solid-state detectors, have been proposed. In particular, the recent strong developments of modern silicon devices have boosted this technology towards a new generation of photodetectors, based on the simple inverse pn junction. Depending on the internal gain, it is possible to distinguish three families of solid-state photon detectors (see Fig. 2.10):

- *PN or PIN photodiodes*, with essentially no gain;

- *Avalanche PhotoDiodes*, working in linear regime and reaching a gain of few hundreds;

- avalanche photodiodes in Geiger-Mode (G-APDs, more commonly referred to as *SiPMs*), operating in Geiger regime with gains between 10^5 and 10^6.

These solid-state devices exhibit important advantages over PMTs, namely higher quantum efficiency, lower operation voltages (and hence strongly reduced power consumption), weak sensitivity to external magnetic fields, robustness and compactness.

The starting point of semiconductor photodetector technology is represented by the development of the basic pn junction, in the 1940s. Since then, this field has known a whirling evolution, marked by some fundamental milestones. In 1959, Gärtner (Gärtner [1959]) investigated for the first time the potential of wider depletion regions achievable with a PIN structure, destined to become the most widely used format for photodiodes for decades and decades. Silicon was the first material to be proposed (and effectively to be used), but in the course of the years also other materials, like Germanium (Riesz [1962]), started to be taken into account. In the meantime, the avalanche multiplication

43

process started to be investigated (McKay and McAfee [1953]) and developed. Pioneering works in the development of solid state avalanche photon detectors were carried on in the 1960s, while in the following decades a very active field of experimental and theoretical researches was represented by the investigation of Geiger-mode avalanche. Such studies led to the development of a new generation of Geiger-mode photodetectors, like Single Photon Avalanche Diode (SPAD), Solid State PhotoMultiplier (SSPM) and Metal-Resistor-Semiconductor(MRS APDs), introduced between 1980s and 1990s. The last milestone was the development, in the first years of 21st century, of a new solid state photodetector operating in Geiger regime and subdivided into many cells connected in parallel over a common substrate: the Geiger-mode avalanche photodiode (G-APD, or SiPM).

In the last decade SiPM technology had an incredible evolution: current devices have reached unprecedented performances, especially concerning quantum efficiency, gain and photon counting capabilities. These devices became commercially available in the recent years and progresses are far from being over.

2.2.1 Physics of semiconductor photodetectors

Solid state photodetectors technology is based on the pn junction, realized by diffusing a donor impurity to a shallow depth into Silicon which is originally high purity p-type doped, having an abundance of holes (majority carriers) and few mobile electrons (minority carriers). The so-obtained surface layer is therefore n-type doped, with a high electron concentration. As the junction is formed, electrons diffuse away from the n-region into the p-region, leaving behind positively charged ionized donor atoms and recombining with the abundant holes. Analogously, holes diffuse away from the p-region, leaving behind negatively charged ionized acceptor atoms and recombining with the abundant mobile electrons. As a result, a very high resistivity space-charge region (called *depletion region*) is formed, almost totally depleted of mobile charge carriers. The thickness of this layer in each region is inversely proportional to the concentration of dopants in the region (Saleh and Teich [2007]).

When a photon impinges over the surface of the photodiode, it is absorbed with an absorption coefficient α. Electron-hole pairs can be produced by light if the energy of the incident photon is at least equal to the band gap energy E_{gap} of the semiconductor material to excite an electron from the valence to the conduction band:

$$E_{ph} = h\nu = \frac{hc}{\lambda} > E_{gap},\qquad(2.7)$$

therefore, the threshold wavelength λ_{th} for the photo-generation process is given by:

$$\lambda_{th} = \frac{hc}{E_{gap}} = \frac{1.24}{E_{gap}[eV]}[nm].\qquad(2.8)$$

In the case of Si at room temperature, the band gap energy is $E_{gap} = 1.12$ eV, therefore the threshold wavelength is $\lambda_{th} = 1100$ nm, while for Silicon photodiodes $\lambda_{th} = 320$ nm. Incident photons with wavelengths shorter than λ_{th} do not generate electron-hole pairs and therefore the incident light is just absorbed, with intensity decaying exponentially with the distance into the semiconductor. The absorption probability depends on the
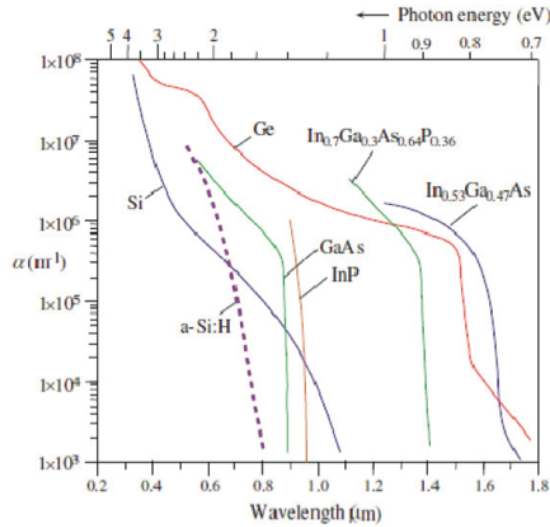
Figure 2.11: Absorption coefficient α as a function of incident photon wavelength for various semiconductors.

probability that the photo-generated electrons get over the energy band gap. For incident photons with energy close to that of the band gap, only the electrons directly at the valence band edge can be excited to the conduction band, therefore absorption is relatively low. As the photon energy increases, a larger number of electrons can be excited, resulting in a higher absorption probability. In Fig. 2.11 it is represented the absorption coefficient α for several semiconductors, as a function of the incident photon wavelength, λ. In particular, it is possible to observe that, unlike the case of direct band gap semiconductors (as GaAs, InP), for indirect band gap semiconductors (like Si) there is a long tail in absorption out to long wavelengths (Green and Keevers [1995]). The path of photons is determined by α: a low absorption coefficient implies poor light absorbed, and if the material is thin enough it will appear transparent to that wavelength. Therefore, for an incident photon flux, it is possible to distinguish three different cases for electron-hole pairs generation: outside the depletion layer, inside the depletion layer and at the edge. Electron-hole pairs generated away from the depletion layer are not under the effect of an electric field. For this reason, they just wander randomly and quickly recombine because of the abundance of recombination centers, thus not contributing to the output electric current signal. On the other side, pairs generated inside the space-charge region drift under the influence of the electric field: electrons move to the n-type doped region and holes in the opposite direction. As a result, a photocurrent is generated in the external circuit. In the case of photons absorbed outside the depletion region, but near the edge, there is a nonzero probability that the produced pairs enter the space-charge region by random diffusion and get quickly transported across the junction by effect of the internal electric field, thus contributing to the output current signal.

The probability that a single photon incident on the device generates an electron-hole pair contributing to the output signal is called *quantum efficiency* (η). It is defined as the ratio between the number of electrons collected per seconds (given by I_{ph}/e, where I_{ph} is the measured photocurrent) and the number of incident photons per second (given
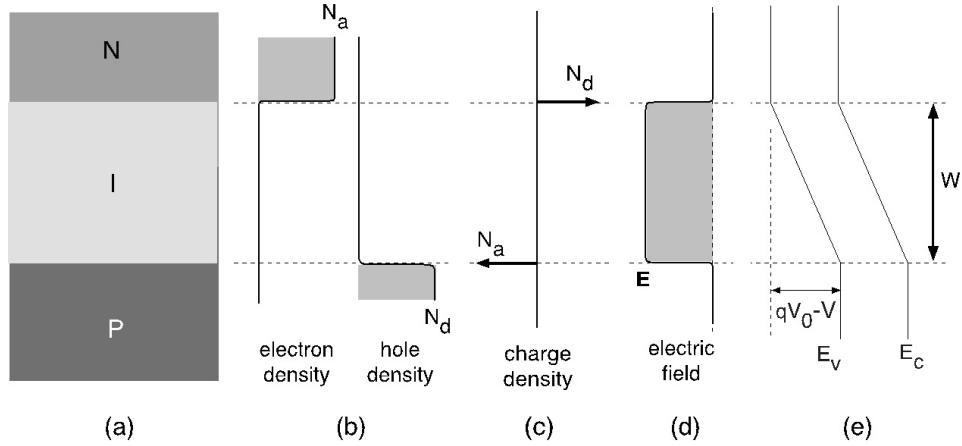
Figure 2.12: (a) Structure, (b) carrier distribution, (c) charge distribution, (d) electric field, and (e) band diagram of a PIN photodiode under reverse bias (Titus et al. [2011]).

by $P_o/h\nu$, with P_o the incident optical power). Therefore, η can be written as:

$$\eta = \frac{I_{ph}/e}{P_o/h\nu}. \tag{2.9}$$

The quantum efficiency of photodetectors is directly related to their *responsivity* (R), defined as the ratio between the output electric current and the incident optical power. Therefore:

$$\eta = \frac{I_{ph}/e}{P_o/h\nu} = \frac{Rh\nu}{e} = \frac{R[A/W] \times 1240}{\lambda[nm]} \times 100[\%]. \tag{2.10}$$

Many factors can affect the quantum efficiency of a photodetector: the absorption region depth, as previously shown; the probabilistic nature of the absorption process itself and the possible reflection of photons over the active surface of the device. In order to obtain a high quantum efficiency, it is required that thickness and depth of the depletion layer are optimized for the expected wavelength band of the incident light. Indeed, the absorption length of photons shows strong variations, ranging from about 10 nm, for near UV light, to more than 1 mm, in the infrared region.

2.3 PIN photodiodes

A PIN photodiode is obtained inserting a layer of intrinsic (or lightly doped) semiconductor material between the p-type and n-type doped regions of a standard pn junction. Such a configuration has been developed in order to obtain a significantly larger depletion region and thus to optimize photon collection. Indeed, the space-charge layer extends into each side of a junction in a range inversely proportional to the doping concentration. Therefore, in both the p-i and i-n junctions the space-charge layer penetrates so deeply into the i-region that under certain doping conditions it can be fully depleted. As a result, the PIN photodiode can be considered as a standard pn junction with a depletion layer that encompasses the entire intrinsic region (see Fig. 2.12). In order to get an increased space-charge layer, a reverse bias is applied to the diode junction, offering better
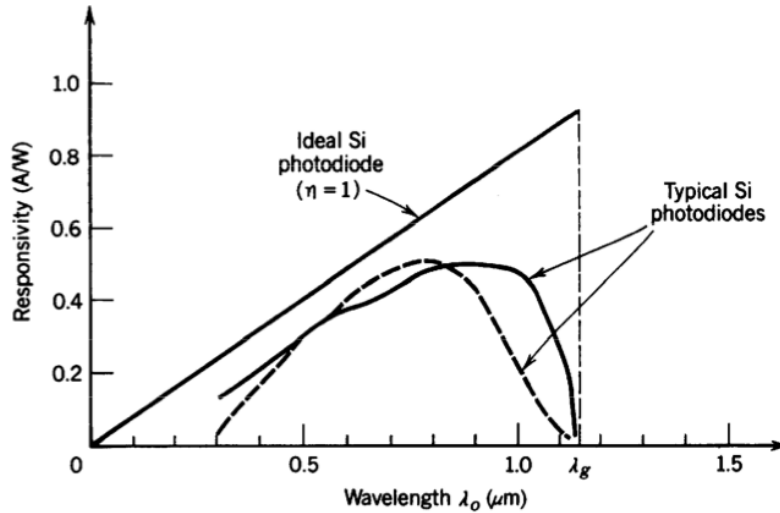
Figure 2.13: Responsivities versus incident photon wavelength (λ_0) for ideal and typical Silicon PIN photodiodes.

performances for high bandwidth and high dynamic range applications but introducing a noise current which reduces the signal-to-noise ratio. PIN photodiodes are among the most widely used solid state photodetectors today. However, they do not provide any internal amplification of the output signal. This means that the number of charges generated is equal to the number of detected photons and therefore the employment of PIN photodiodes is suitable only for applications in which a large amount of photons (roughly at least $\sim 10^4$) is simultaneously detected by the device and in particular for optical communications. Apart a larger depletion layer, increasing the photodetection efficiency, PIN photodiodes offer several advantages over standard pn junctions. The ratio between the diffusion length and the drift length of the device is reduced, resulting in a greater proportion of the generated current being carried by the faster drift process (Saleh and Teich [2007]). Moreover, the increased width of the depletion layer increases the transit time, while reducing the junction capacitance. As a consequence the time constant of the device ($\tau = R_L C_J$, where R_L is the load resistance and C_J the junction capacity) is reduced, implying a faster response. Typical response times of PIN photodiodes are of the order of tens of picoseconds. In Fig. 2.13 the responsivities as a function of incident photon wavelength (λ_0) for ideal and typical Silicon PIN photodiodes are shown. λ_g is the band gap cutoff wavelength. (Saleh and Teich [2007]).

2.4 Avalanche Photodiodes

Avalanche PhotoDiodes (APDs) are strongly reverse-biased photodiodes, providing internal amplification and thus sensitive to even extremely weak signals. The very high electric field over the junction converts each detected photon into a cascade of electron-hole pairs. Indeed, the generated primary charge carriers are strongly accelerated, acquiring enough energy to generate new pairs by impact ionization due to collisions with the crystal lattice. These "collision-generated" secondary electron-hole pairs are themselves accelerated by the electric field to a sufficiently high kinetic energy to trigger further impact ionization
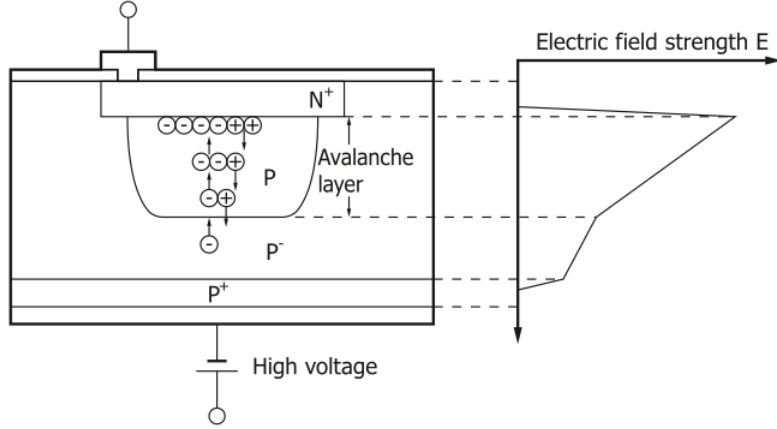
Figure 2.14: Schematic diagram of APD structure (Hamamatsu-Photonics [2013]).

events. The result is that a single absorbed photon can generate a cascade of impact ionization events that produces an avalanche effect and thus a strong internal mechanism of photogenerated current amplification.

Compared to PIN photodiodes, APDs provide a higher signal-to-noise ratio and are used in a wider variety of applications.

An optimal geometry for an APD should maximize photon absorption (as in the case of a PIN photodiode), while keeping as thin as possible the multiplication region, in order to keep uniform the electric field and thus to minimize the possibility of localized uncontrolled avalanches produced by the strong electric field. The typical design of an APD is shown in Fig. 2.14. Photons are absorbed in a large intrinsic or lightly doped region (typically a very lightly doped p region, p^+ or π) and drift across it entering into a thin $p - n^+$ junction where a sufficiently strong electric field triggers the avalanche progress. The probabilities (per unit length) for electrons and holes to generate secondary pairs by impact ionization processes are called *ionization coefficients* and are typically indicated with α and β, respectively. Therefore, the inverse coefficients $1/\alpha$ and $1/\beta$ represent the average distances between consecutive ionizations. An important parameter for characterizing the performances of an APD is the *ionization rate ratio* (k), defined as the fraction between α and β.

In Silicon, the ionization rate of electron is larger than that of holes, therefore electrons provide the major contribution to the multiplication process. For this reason, the optimal design for an APD is that in which only electrons are able to start the avalanche processes and hence in which the electron-hole pairs are generated at the p edge of the depletion layer.

Gain

In the impact-ionization avalanche process, each absorbed photon creates in average a finite number M of electron-hole pairs. The value of the multiplication factor M depends on the probability of impact ionization:

$$1 - \frac{1}{M} = \int_0^W \alpha \exp\left[-\int_x^W (\alpha - \beta)dx'\right] dx, \tag{2.11}$$

48
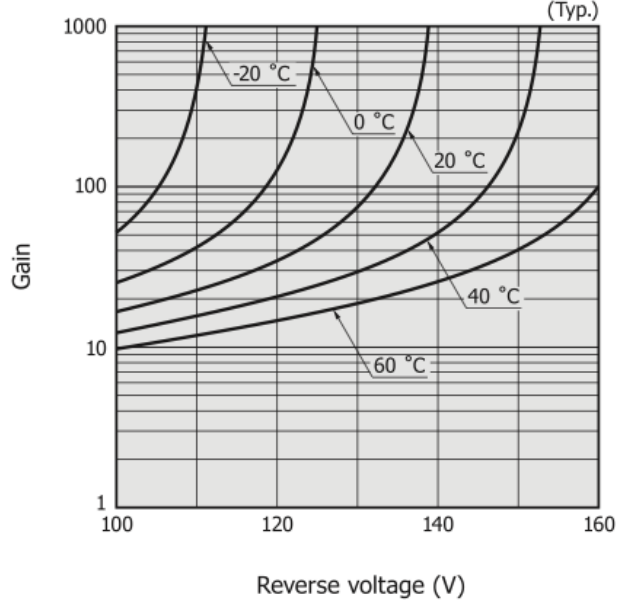
Figure 2.15: Temperature characteristics of Hamamatsu S2382 APD structure (Hamamatsu-Photonics [2013]).

where W is the width of the depletion layer. The impact ionization coefficients are themselves strongly dependent on the reverse bias applied (V_{bias}), therefore the multiplication factor can be empirically approximated by:

$$M = \frac{1}{1 - \left(\frac{V_{bias}}{V_{BD}}\right)^n},$$
(2.12)

with V_{BD} the breakdown voltage of the device and n a parameter depending on the material (Miller [1957], Titus et al. [2011]).

APD are said to operate in a *linear* regime, because the number of collected carriers is proportional to the number of absorbed photons with proportionality factor M. The typical values of the multiplication factors range between several tens to few hundreds, making APDs not an optimal solution for applications where signals of a few photons only need to be detected.

In addition, the gain of APDs exhibits a temperature-dependent behavior. In particular, the gain at a fixed reverse voltage decreases as temperature rises. Indeed, in correspondence of higher temperatures, the crystal lattice starts to vibrate more and hence the possibility that an accelerated carriers collides before triggering a further impact ionization event increases (see Fig. 2.15).

Timing

The timing performances of an APD are determined by the following factors:

- RC time constant;

- drift time;

49

- multiplication time;

- diffusion time of carriers generated outside the depletion region.

In order to improve the time response of an APD, the most immediate solution consists in the reduction of the RC time constant. This is achievable by reducing the sensitive area of the device while realizing a thicker depletion area. However, a wider depletion layer has the effect to lengthen the drift time of charge carriers. Indeed, the speed of the electrons in the depletion layer tends to saturate to values approximately of the order of 10^7 cm/s for electric fields of about 10^4 V/cm, therefore the larger is the path, the longer is the time required to cover it.

Moreover, charge carriers generating the impact ionization avalanche process collide repeatedly with the crystal lattice. Therefore, the multiplication time has the effect to increase the time required to move through the depletion layer. Such time increases with the gain and starts to become critical for gains of the order of several hundreds. This means that on average the time response of the APD is longer with respect to the case of a standard PN or PIN photodiode.

The effect of diffusion time of the charge carriers generated outside the depletion layer has typical values of few microseconds and arises if the depletion layer depth is higher than the penetration depth of the incident photon flux in Silicon. In order to reduce such effect, it should be necessary to increase the reverse bias voltage and to optimize the surface layers depending on the expected wavelength of the light to be detected.

2.5 Silicon Photomultipliers

Due to its relatively low internal amplification ($\sim 10^2$), the APD cannot be the ideal device to address the challenge of detecting, timing and quantifying low-light signals down to the single-photon level.

Single photons can be detected efficiently by avalanche diodes operating in Geiger mode, known as Single-Photon Avalanche Diodes (SPADs). SPADs are essentially APDs operating with a reverse bias voltage above the breakdown point. In such bias conditions, the electric field generated within the depletion layer is so high ($\sim 10^5$ V/cm) that even a single carrier injected inside the space charge region can trigger a self-sustaining Geiger avalanche, amplifying the original photoelectron into a macroscopic current flow.

In order to stop the avalanche current and, then, to restore the initial bias conditions enabling the detection of new incoming photons, a so-called *quenching* mechanism is required. Typically, quenching is realized by means of a passive circuit in which the current drawn by the photodiode during the Geiger breakdown is limited by a high-impedance load ($R_Q > 100$ kΩ) connected in series, as shown in Fig. 2.16. In Fig. 2.17 the equivalent circuit of SPAD breakdown process is represented. In the steady state, the diode capacitance C_D is charged at a reverse voltage higher than the breakdown point ($V_{BIAS} > V_{BR}$). As a carrier traverses the high electric field region (switch closed in Fig. 2.17), initiating an avalanche discharge, the new state of the system can be modeled adding to the basic circuit shown in Fig. 2.16 a voltage source V_{BR} with a series resistor R_S in parallel to the diode capacitance. R_S (~ 1 kΩ) includes both the resistance of the neutral regions inside the silicon and the space-charge region resistance. Therefore, as the avalanche
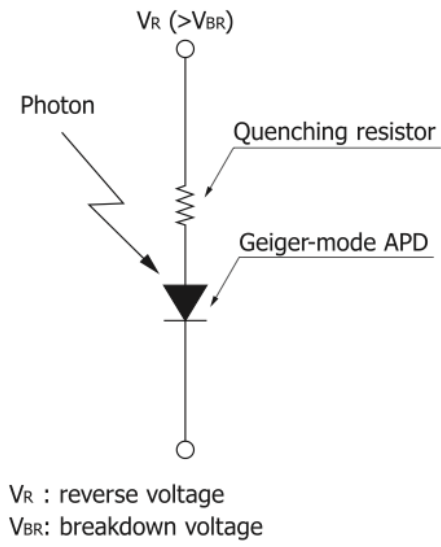
Figure 2.16: Quenching resistor of a Geiger-Mode APD (Hamamatsu-Photonics [2013]).
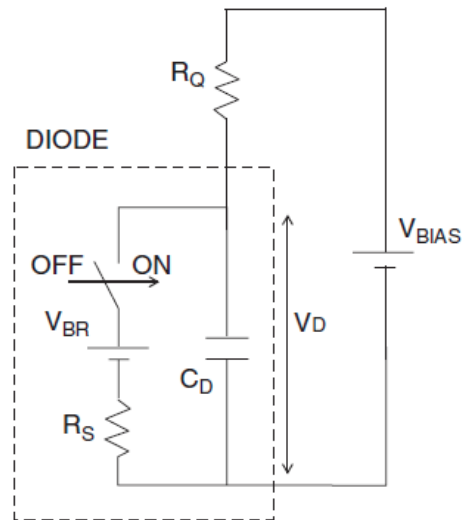
Figure 2.17: Equivalent circuit of SPAD breakdown.
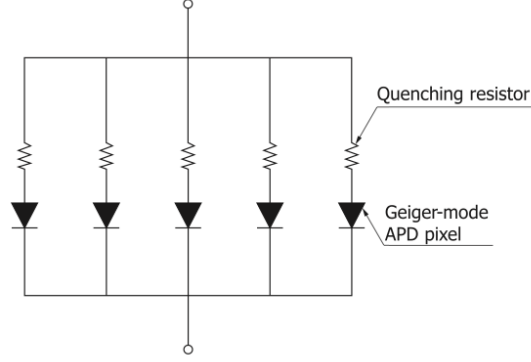
Figure 2.18: Equivalent circuit of a SiPM (Hamamatsu-Photonics [2013]).

is initiated, C_D discharges through the series resistance down to the breakdown voltage with a time constant $\tau_D = R_S C_D$, typically of the order of few hundreds of ps.

As the voltage on C_D decreases, the current flowing through the quenching resistor tends to the asymptotic value of:

$$I_f = \frac{V_{BIAS} - V_{BR}}{R_Q + R_S}. \tag{2.13}$$

In this final phase, if R_Q is high enough (at least some hundreds of $k\Omega$), the diode current is so low that a statistical fluctuation brings the instantaneous number of carriers flowing through the high-field region to zero, quenching the avalanche (Barbarino et al. [2011]). When the avalanche process is halted, the switch is again open and the circuit is back in its initial configuration, with the diode capacitance charged back at V_{BR}. Then, C_D recharges to the bias voltage with a time constant $\tau_R = C_D R_Q$ and the device becomes ready to detect the arrival of a new photon. Therefore, the output current caused by the Geiger discharge is a pulse waveform with a short rise time, while the output current when the Geiger discharge is halted by the quenching resistor is a pulse waveform with a relatively long fall time, with recovery time constant τ_R. For this reason, although extremely easy to realize, this solution sets severe limitations on the device performances, especially in terms of dead time and maximum admissible photon counting rate (Neri et al. [2011]).

The main limit of SPADs is that the output signal is the same regardless of the number of interacting photons. Indeed, a single photodiode operating in Geiger mode works as a photon-triggered switch, with a binary "ON" or "OFF" state, and therefore it only provides information on whether or not a signal has been detected, without providing an output proportional to the intensity of the incident photon flux.

In order to overcome this lack of proportionality, the photodiode can be segmented in an array of small, electrically and optically isolated micro-cells. All these pixels operate in Geiger mode, have their own quenching resistor and are connected in parallel to a single output. This structure is called *Silicon PhotoMultiplier* (SiPM, in Fig. 2.18 the equivalent circuit is shown). Unlike APDs, in order to achieve a good optical insulation among the micro-cells, the photosensitive surfaces of SiPMs contain some inter-pixel insulating sections that cannot detect light. Moreover, in order to stop the breakdown process, all the pixels require a quenching resistor, which is typically mounted on the surface of the device (see Fig. 2.19). For these reasons, some photons incident on the
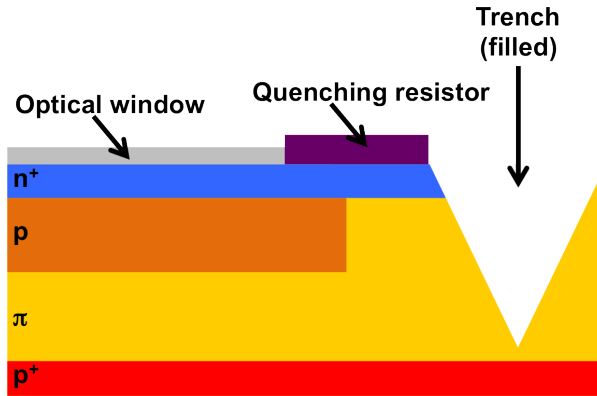
Figure 2.19: Schematic view of a SiPM cell.
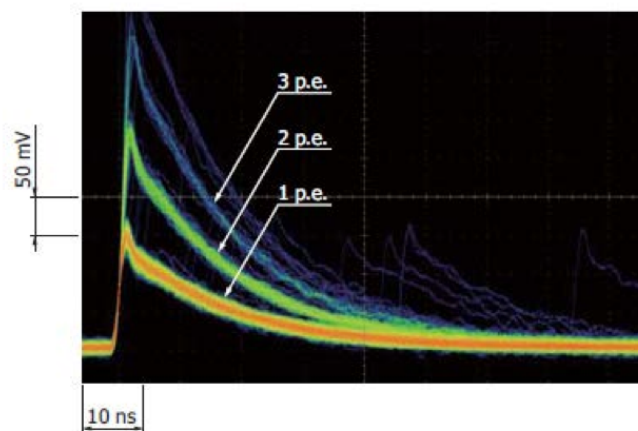
Figure 2.20: Pulse waveform of a SiPM overlaid for multiple triggers (Hamamatsu-Photonics [2010]).

detector surface are not detected, thus significantly reducing the sensitive area of the device. The ratio between the effective (useful) and the total detector surfaces is called *fill factor* (ff): it depends on the design and on the layout of the pixels only and has typical values ranging between $\sim 30\%$ and $\sim 80\%$. When activated by a photon, each element gives the same current response. Since all the pixels are connected to one readout channel only, the output pulses of SiPM pixels overlap each other, creating a single output pulse. The output signal of the device is therefore equal to the sum of the single outputs of the micro-cells and hence it is proportional to the number of pixels hit by the incident photon flux. In Fig. 2.20 it is possible to see the typical output of a SiPM under extremely low illumination, where the responses for multiple triggers are overlaid. The pulse height varies accordingly to the number of detected photons and individual waveforms are very well distinguishable, thus highlighting the excellent photon counting capabilities of SiPMs and their extreme suitability for single photon detection applications. Silicon PhotoMultipliers offer a highly attractive solution in the field of photon detection, with performances going beyond the low light detection capabilities of the standard PMTs while keeping all the benefits of a solid-state device. Indeed, SiPMs are characterized by fast response, excellent time resolution and wide spectral response and, in addition, show a weak sensitivity to external magnetic fields, high resistance to

mechanical shocks and excellent uniformity of response. In the next section, the basic performances of SiPMs will be discussed in details.

2.5.1 SiPM characteristics

Gain

The gain (G) of the SiPM is determined by the number of carriers generated during a Geiger avalanche process. In particular, the gain is defined as:

$$G = \frac{Q}{e}, \tag{2.14}$$

where Q is the charge of the pulse generated from each pixel during the breakdown process and e is the charge of the electron. Q depends on the diode capacitance and on the applied overvoltage:

$$Q = C_D(V_{BIAS} - V_{BR}), \tag{2.15}$$

therefore the gain can be expressed as follows:

$$G = \frac{Q}{e} = \frac{C_D(V_{BIAS} - V_{BR})}{e} = \frac{1}{e}\frac{(V_{BIAS} - V_{BR})}{R_Q}R_Q C_D = \frac{I_{max}\tau_R}{e}, \tag{2.16}$$

where I_{max} is the maximum output current during breakdown and τ_R is the pulse rise time constant.

Starting from Eq. 2.16, the gain fluctuations are given by:

$$\frac{\delta G}{G} = \frac{\delta V}{V} \oplus \frac{\delta C_D}{C_D}. \tag{2.17}$$

The contribution of voltage fluctuations is mainly due to doping densities, following a Poisson distribution with $\delta V \geq 0.3V$. On the other hand, the contribution of diode capacity fluctuations is in general less important. It is linked to cell-to-cell non-uniformities (in terms of active area and volume) and typically is controlled within a level of the order of few percents.

In order to measure the gain of a SiPM it is mandatory to measure the charge of the pulse generated from each pixel during the Geiger discharge process. Due to the unique photon counting capabilities of SiPMs, the output of each pixel is extremely uniform and highly quantized. Therefore, each signal detected by a SiPM corresponds to a quantized output pulse, as shown in Fig. 2.20. If such pulses are integrated, the obtained charge spectrum shows well defined peaks, each one corresponding to a different number of fired pixels (see Fig. 2.21).

The separation between each pair of adjacent peaks (in pC) is constant and is equal to the charge released by the pixels in correspondence of a single Geiger discharge (SensL [2011]). The so-measured values of Q can thus be used to accurately calculate the gain, based on Eq. 2.14. The gain of a SiPM has typical values ranging between 10^5 and 10^6 and shows an excellent linearity as a function of the reverse applied overvoltage. Fig.2.22 shows the gain curve of a Hamamatsu device (S10362-11-025U), measured following the approach described above (Barbarino et al. [2011]).

Based on Eq. 2.16, it is possible to obtain the value of the diode capacitance C_D from the
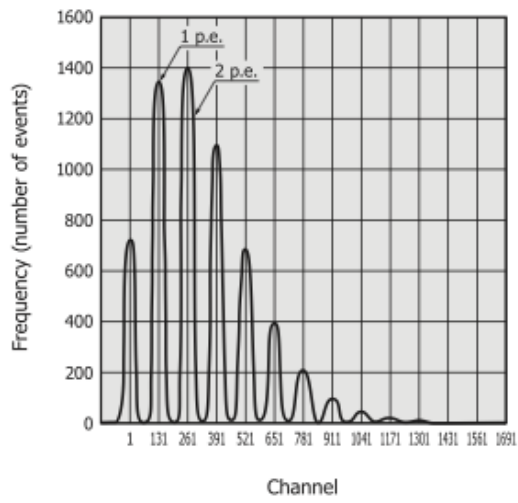
Figure 2.21: Typical charge spectrum of a SiPM (Hamamatsu-Photonics [2013]).
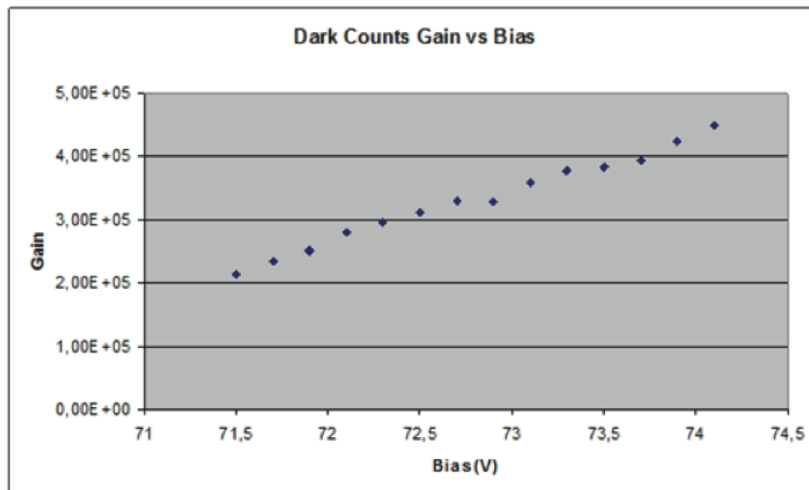
Figure 2.22: Gain vs voltage of Hamamatsu S10362-11-025U.

linear fit of the gain curve. Indeed, indicating with b the slope of the fitting straight line, the diode capacitance is given by $C_D = be$, where e is the charge of electron. Moreover, extrapolating from the fitting line the voltage value corresponding to G=0 it is possible to estimate the breakdown voltage.

As for APDs, also the gain of SiPMs exhibit a dependence on the ambient temperature. Indeed, as the temperature rises, the crystal lattice vibrations become stronger, thus increasing the probability that charge carriers collide with the lattice before triggering the Geiger avalanche process.

Photon Detection Efficiency

The Photon Detection Efficiency (PDE) of a SiPM is the statistical probability that an incident photon will produce a Geiger pulse from one of the SiPM micro-cells. It is defined as ratio of the number of detected photons to the number of incident photons during photon counting where the pulsed light enters the SiPM. The PDE can be expressed as follows:

$$PDE = \eta \times ff \times P_{trigger}, \tag{2.18}$$

where η is the quantum efficiency of Silicon, ff is the fill factor and $P_{trigger}$ is the avalanche initiation probability (or trigger probability), that takes into account the fact that not all generated photoelectrons are able to initiate an avalanche.

The intrinsic quantum efficiency of Silicon has typical values ranging between 80% and 90% and strongly depends on the thickness of topmost layers and of the depletion area. Indeed, in order to maximize the photon conversion process for the expected incident wavelengths, an efficient absorption of photons is required and hence an optimal thickness of the surface layers and a sufficiently large depletion region. Taking into account the probability of reflection of photons on the device surface ($\mathcal{R}$) and the absorption coefficient α in Silicon, the quantum efficiency can be expressed as:

$$\eta = (1 - e^{-\alpha x})(1 - \mathcal{R}), \tag{2.19}$$

where x is the position in which the electron-hole pair is generated.

The triggering probability $P_{trigger}$ depends on the position where the primary electron-hole pairs are generated and on the applied overvoltage ($V_{BIAS} - V_{BR}$). In a standard $n^+ - p - \pi - p^+$ structure, if the electron-hole pair is generated in the upper side region, the electron is directly collected at the n^+ terminal. In such conditions, only the holes are forced to pass the whole high-field region, triggering the avalanche process, while electrons do not provide any contribution. Conversely, when the pair is generated in the bottom side (p), the situation is symmetrical and only electrons contribute to the triggering probability. For this reason, considering that, in Silicon, the triggering probability of electrons (P_e) is higher (of about a factor 2) with respect to holes (P_h), a photon conversion happening in the p region would maximize the triggering probability. In the case of a $n^+ - p - \pi - p^+$ structure, long wavelengths are favored for photon conversion in the p region. In order to maximize the quantum efficiency also for short wavelengths, the entrance window and the upper n^+ layer should be made as thin as possible or, as an alternative, a higher overvoltage should be applied, considered that P_h increases with the internal electric field.

For each electron-hole pair generated, the probability that neither the electron nor the
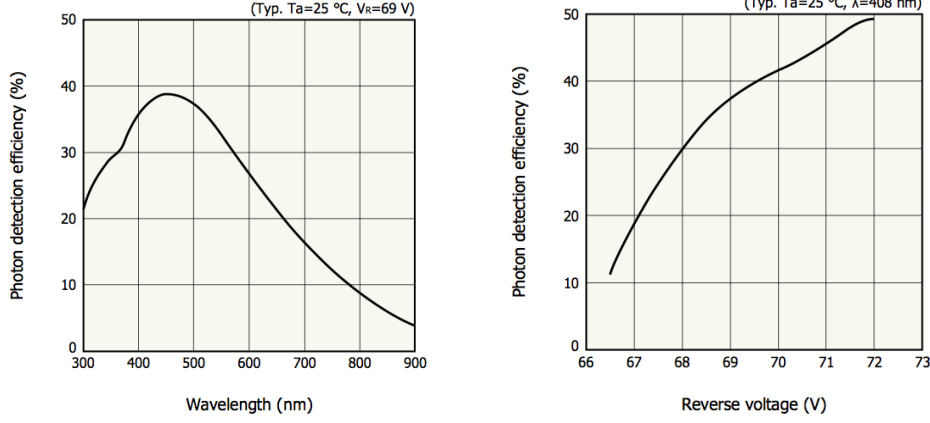
Figure 2.23: PDE vs wavelength (left) and PDE vs bias (right)

hole causes an avalanche is given by $(1 - P_e) \cdot (1 - P_h)$. Consequently, the probability $P_{trigger}$ that either the electron or the hole initiates a breakdown avalanche is given by

$$P_{trigger} = P_e + P_h - P_e P_h. \tag{2.20}$$

Therefore, the PDE can be written as:

$$PDE = (1 - e^{-\alpha x})(1 - \mathcal{R}) \times ff \times (P_e + P_h - P_e P_h). \tag{2.21}$$

The PDE can be calculated in terms of the responsivity of the SiPM according to the following equation:

$$PDE = \frac{R\,hc}{G\,\lambda e} = \frac{1240}{\lambda[nm]}\frac{R}{G}, \tag{2.22}$$

where:

- R is the responsivity;

- G is the gain of the SiPM;

- h is the Planck constant;

- c is the speed of light;

- e is the charge of the electron;

- λ is the wavelength of the incident photons;

Analogously to the APD case, the responsivity of the SiPM is defined as the average photocurrent produced per unit incident optical power. The PDE shows strong dependences on bias and wavelength. In particular, it increases as the reverse voltage increases, while the dependence on wavelength is directly correlated to the responsivity (see Fig. 2.23).
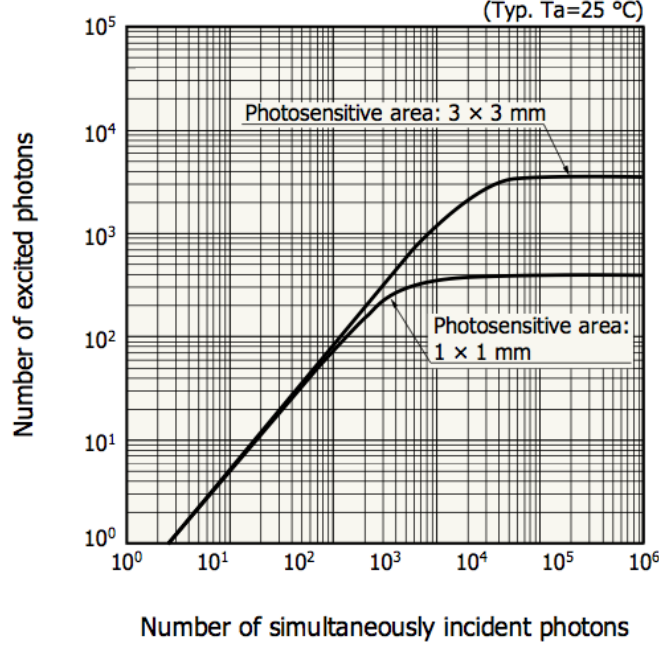
Figure 2.24: Dynamic ranges for 50 μm pitch SiPMs, with active surfaces of 3×3 mm^2 and 1×1 mm^2 (3600 and 400 pixels, respectively) (Hamamatsu-Photonics [2013]).

Dynamic Range

The dynamic range of a detector is defined as the range of incident photon fluxes over which the detector is able to provide a useful output. In the case of SiPMs, this range extends from the lowest detectable signal level (defined as the mean signal that yields SNR = 1) to the optical signal level that results in all of the SiPM pixels simultaneously fired. For higher light levels, the output of the detector saturates, until some of the micro-cells have recovered back to their steady state. In other words, the average number of photons per cell should be less than 1. Under low light intensity conditions, corresponding to a number of detected photons much smaller than the number of cells, the output of SiPM is fairly linear. As the number of incident photons increases, also the probability that two or more photons enter into the same pixel increases. And since the output of each micro-cell, due to the Geiger breakdown, is the same regardless of the number of incident photons, the output linearity degrades as the number of incident photons increases and then saturates when the number of photons is about equal to the number of cells, see Fig. 2.24. The dynamic range of a SiPM is therefore a function of the total number of micro-cells ($N_{\mu c}$) and of the PDE of the device. In particular, it is limited by the condition that

$$\frac{N_{ph} \times PDE}{N_{\mu c}} < 1, \tag{2.23}$$

where N_{ph} is the number of incident photons.

The number of fired pixels (N_{fired}) as a function of the number of incident photons and of PDE is given by:

$$N_{fired}(N_{\mu c}, \lambda, V) = N_{\mu c} \times \left[1 - \exp\left(\frac{-N_{ph} \times PDE(\lambda, V)}{N_{\mu c}}\right)\right]. \tag{2.24}$$

Being dependent on the PDE, N_{fired} is wavelength and overvoltage dependent, as shown in the previous section. In order to increase the dynamic range of a SiPM, one of the most immediate solutions could be to increase the number of available micro-cells. However, as $N_{\mu c}$ increases, the fill factor of the device drops dramatically, thus decreasing the PDE.

Time performances

After incident photons penetrate inside the depletion region, triggering a Geiger breakdown, a time interval is required for the generated pulse to be seen in output. Such time is called *transit time* and its jitter, that determines the time resolution of the SiPM, is called *Transit Time Spread* (TTS), with typical values of the order of $\sim 10^2$ *ps*. In general, the TTS of a SiPM decreases as the applied overvoltage and/or the number of incident photons increase.

The avalanche breakdown is an extremely fast process, therefore very good timing performances, even for single photons, can be expected for a SiPM. Some small fluctuations in the avalanche process can arise just in case of lateral spreading by diffusion and by the photons emitted in the avalanche (Barbarino et al. [2011]).

The time required for pixels to restore the steady state conditions is called *recovery time* and depends on the photosensitive area and on the pixel size. In particular, it typically ranges from few tens of nanoseconds (for pitches of $\sim 10\mu m$) to few hundreds of nanoseconds (for pitches up to $100\mu m$). If a photon absorption process occurs before the output pulse is completely restored, then a small pulse is output, which does not reach the gain set by the operating voltage.

Noise

As shown in the previous sections, SiPMs have extremely attractive features, such as high gain, high PDE, excellent timing and wide spectral range. However, several noise sources seriously affect SiPM performances, thus setting severe limitations to the possible applications and to the design of the device itself.

- **Dark Counts**

As shown before, SiPM pixels are not able to provide information about the intensity of the incident photon flux: the output pulse produced by the detection of one photon is completely indistinguishable from that produced by the detection of many simultaneous ones. This means that each carrier injected inside the depletion layer can trigger a Geiger breakdown and fire the relative pixel, even in case of a single thermally generated electron or hole. Such pulses, called *dark pulses*, are identical in shape to the photon-generated pulses and represent a source of noise for the device at the single photon level. Indeed, higher level dark pulses can arise only if two or more thermally generated carriers trigger an avalanche within the response time of the device. Therefore, dark pulses rates dramatically decrease as the number of photoelectrons increases.

Such noise, arising from the random motions of mobile carriers in resistive electrical materials at finite temperatures, is called *dark noise* and the number of dark pulses per second is called *dark count rate*. In principle, since the magnitude of dark pulses is practically a constant (single photon level), it should be possible to discriminate it simply by setting a threshold or, if an external trigger for the incident light is available,
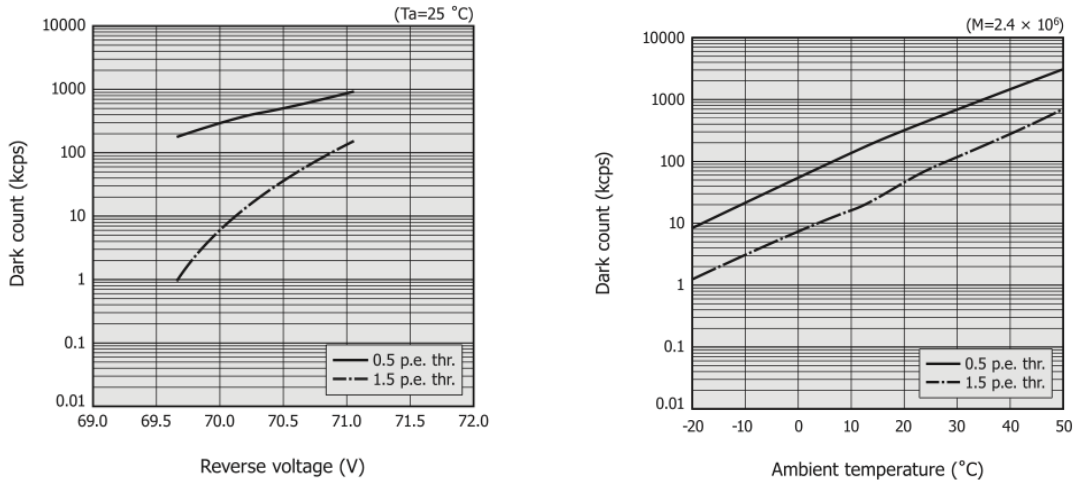
Figure 2.25: Dark counts rate as a function of reverse voltage (left) and ambient temperature (right) (Hamamatsu-Photonics [2013]).

by setting a proper time gate.

In general, since the occurrence of dark pulses is not constant, but follows a Poissonian distribution, the noise contribution is usually assumed to be equal to the square root of the dark count rate. Typically, current SiPMs have dark count rates ranging between few tens and some hundreds of kcps (kilo-counts per second) per mm^2 of active surface. The dark count rate shows a strong dependence on the applied overvoltage, on pixel size and on temperature. As shown in the previous sections, the trigger probabilities (for both electrons and holes) is a function of the applied bias. Therefore, as the overvoltage increases, also the probability that thermally generated pairs trigger a Geiger breakdown (and hence the dark count rate) increase (see Fig. 2.25, left panel). Moreover, the probability that an electron-hole pair is thermally generated increases with the number of generation-recombination centres. Therefore, the sensitive surface of the device and the depletion layer thickness should be kept as low as possible in order to reduce the dark count rate. Other improvements can be achieved by minimizing impurities and crystal defects of Silicon.

By definition, since dark pulses are produced by thermally-generated carriers, the dark count rate increases with the ambient temperature (see Fig. 2.25, right panel). The dependence of the dark count rate (for a threshold of 0.5 photoelectrons, $N_{0.5\ pe}$) as a function of the ambient temperature is given by the following expression:

$$N_{0.5\ pe}(T) \approx A T^{\frac{3}{2}} \exp\left[\frac{E_g}{2kT}\right], \tag{2.25}$$

where A is an arbitrary constant, T the absolute temperature, E_g the bandgap energy of Silicon and k the Boltzmann constant (Hamamatsu-Photonics [2013]).

- **Afterpulses**

Another factor that significantly affects the signal-to-noise ratio of a SiPM is the phenomenon of afterpulses. During the Geiger avalanche process, some charges carriers can
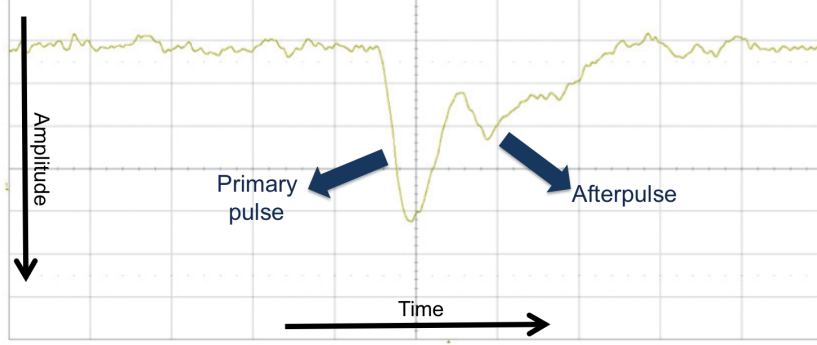
Figure 2.26: Primary pulse and afterpulse observed at the oscilloscope.

be temporarily trapped by some impurities inside the crystal lattice and thus generate a further breakdown after they are released. Such delayed pulses, called *afterpulses*, are secondary breakdowns that can occur after a dark pulse or after a photon absorption event.

The amplitude of the afterpulses has a significant dependence on the time delay at which they occur, with respect to the primary pulse time. Indeed, afterpulses with short time delay are smaller than standard pulses because in this case the quenching circuit has not yet kept the diode capacitance C_D to the operation voltage V_{BIAS}, and so the cells are not completely recharged. However, they have the effect to lengthen the recovery time (see Fig.2.26). Conversely, if the carrier is released after the recovery time has elapsed, the generated afterpulse is indistinguishable from a standard pulse generated by a photon or by a dark count.

The probability P_{ap} that an afterpulse occurs with a time delay t after the primary Geiger breakdown is given by (Kishimoto [1991]):

$$P_{ap}(t) = N_c P_t \frac{\exp(-t/\tau)}{\tau} P_{trigger}, \tag{2.26}$$

where N_c is the number of carriers produced during the primary breakdown, P_t is the probability that carriers remain trapped inside the lattice, depending on the carrier flux during the avalanche and on the number of traps, and τ is the trap lifetime, depending on the position of the impurity that captures the carrier. Both N_c and $P_{trigger}$ increase linearly with the applied overvoltage, therefore an overall quadratic dependence on ΔV holds. This means that, in order to keep the afterpulse probability low, it is necessary to limit the bias voltage.

In standard SiPMs, the afterpulse probability varies with the applied overvoltage in the range from about 10% to more than 20%. However, the new generation of Hamamatsu MPPCs (Multi Pixel Photon Counters, commercial name of SiPMs) have reached an unprecedented low afterpulse probability, due to use of improved materials and wafer process technologies, with values drastically reduced to less than 0.3% (Hamamatsu-Photonics [2014a]).

- **Crosstalk**

In addition to dark counts and afterpulses, another important component of the SiPM noise is the optical *crosstalk*.
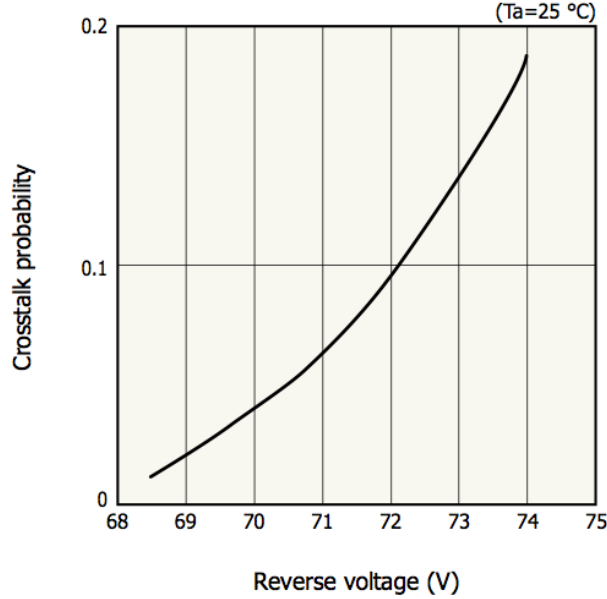
Figure 2.27: Crosstalk probability as a function of the applied voltage (Hamamatsu-Photonics [2013].

During a Geiger avalanche process, in each microcell there are photons emitted by the carriers near the junction, accelerated by the high electric field. Typically, emission occurs in the near infrared region with, in average, up to three emitted photons per pixel having energies above the band gap of the Silicon. Such photons are able to travel relatively long distances through the device and therefore there is a non-zero probability that they penetrate inside a neighboring microcell, initiating a further Geiger breakdown process. The crosstalk probability ($P_{\chi t}$) is the probability that an avalanching microcell will trigger a further avalanche in a second microcell. $P_{\chi t}$ depends on the design of the device (in particular on the distance between neighboring microcells) and has a quadratic dependence on the applied overvoltage. Indeed, $P_{\chi t}$ depends both on the carrier current during the avalanche and on the gain of the device (both $\propto \Delta V$, see Fig. 2.27). Typical values are of the order of few tens of percents, however the new generation of SiPMs shows a far lower crosstalk probability (less than 10%, Hamamatsu-Photonics [2014a]). The crosstalk process is extremely fast and happens almost simultaneously with respect to the primary breakdown. Consequently, a single photon may generate signals equivalent to a 2, 3 or more photoelectrons events. For this reason, $P_{\chi t}$ can be estimated from the fraction of the count rate of events with more than one photoelectron ($N_{1.5pe}$) to that at the single photoelectron level ($N_{0.5pe}$), in randomly triggered events without external light.

$$P_{\chi t} = \frac{N_{1.5pe}}{N_{0.5pe}} \tag{2.27}$$

Indeed, at low bias voltage, a signal corresponding to two or more photoelectrons should be considered crosstalk-related because of the low probability that all the electrons producing the Geiger breakdown are thermally generated.
The crosstalk probability can be reduced operating at a relatively low gain and (up to one order of magnitude) realizing dedicated designs based on trenches filled with opaque material between the cells, acting as optical insulators.
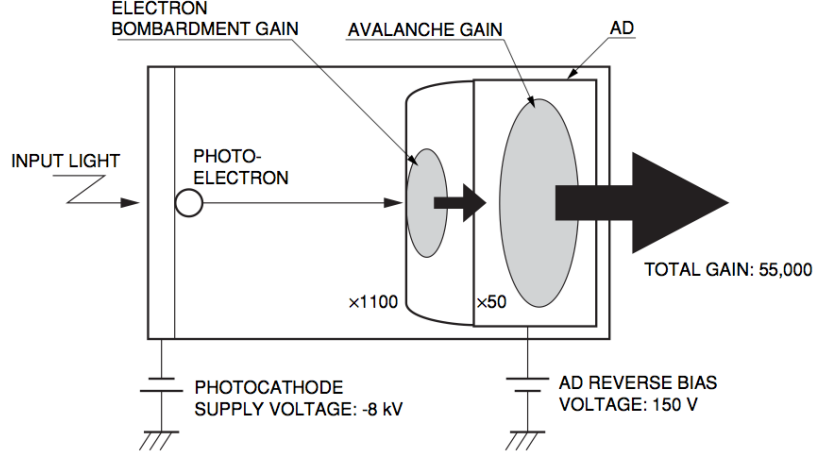
Figure 2.28: Schematic diagram of HPD (Hamamatsu-Photonics [2013]).

2.6 Hybrid PhotoDetectors

Hybrid PhotoDetectors (HPDs) technology is based on an innovative approach in which the large sensitive surface of a standard PMT meets up the high electron resolution and the excellent response stability of APD technology. As for a PMT, in an HPD the incident light impinges on a photocathode, where photoelectric conversion occurs. The so-generated photoelectrons are then accelerated by a high-intensity electric field (of a few kilovolts up to a dozen of kilovolts) applied to the photocathode and focused towards an APD, where electron-hole pairs are generated proportionally to the incident energy of the photoelectrons. In substance, in this configuration the APD replaces the standard dynode chain of PMTs as electron multiplication stage, thus providing less fluctuations during the multiplication process and hence a significantly higher electron resolution (see Fig. 2.28).

As shown in Sec. 2.4, the intrinsic gain of APDs is of the order of few hundreds, a too low value to generate (alone) a measurable output current. However, an additional decisive contribute can be provided by the so-called *bombardment gain*: as the energy of photoelectrons increases, the APD response grows accordingly. For this reason, a strong dependence holds between the photocathode supply voltage and the electron bombardment gain, shown in Fig. 2.29. As the high voltage applied to the photocathode accelerates the photoelectrons to an energy high enough to pass through the insensitive surface layer of the APD and hence to reach its space charge region, a fairly linear trend can be observed. Therefore, a voltage threshold V_{thr} can be identified, above which the electron bombardment gain increases pretty linearly with the applied voltage, with values ranging from few hundreds to ~ 1500.

The Avalanche PhotoDiode inside an HPD typically generates one electron-hole pair per incident energy of approximately $3.6eV$. This value corresponds to the inverse slope of the straight line in Fig. 2.29. Therefore, the expression of the bombardment gain (G_B) is given by:

$$G_B = \frac{V_{BIAS} - V_{thr}}{3.6}.$$

(2.28)
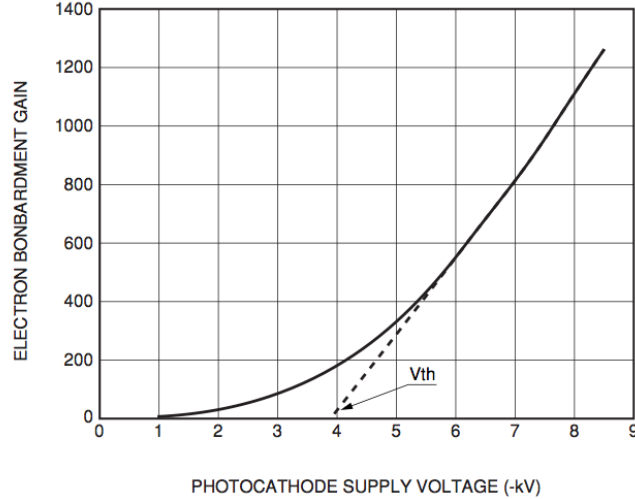
Figure 2.29: Electron bombardment gain characteristics (Hamamatsu-Photonics [2013]).

Taking into account the further internal multiplication factor provided by the APD (G_{APD}), the overall gain of the HPD can be expressed as follows:

$$G = G_B \cdot G_{APD}. \tag{2.29}$$

For the APD, it is difficult to maintain stable operations if the reverse bias voltage is set near the breakdown voltage, therefore typical values of G_{APD} not exceeding one hundred are realized.

In this way, overall HPD gains up to few 10^5 are easily achievable, still slightly lower than the gain of a standard PMT but high enough to generate well measurable output signals. However, for extremely low light conditions the use of a low-noise amplifying stage may be required.

2.6.1 HPD performances

As described in the previous section, the gain mechanism in an HPD is based on the combination of electron bombarding gain and APD intrinsic gain, instead of the standard dynode chain secondary emission process. In this way, a significative reduction of gain fluctuations and, as a consequence, strongly improved photon counting capabilities are achieved with respect to conventional PMTs: typically, the pulse height distribution of an HPD exhibits well separate peaks for incident light levels up to 5 photoelectrons.

In general, an HPD exhibits many advantages in applications where quantitative property, reproducibility and stability are essential factors. Besides the very good linearity achieved by means of bombarding and APD, the main source of improvement is represented by the absence of the dynode chain:

- *Afterpulses* are strongly reduced. In an HPD the only possible contributions are thermal electron emission at the photocathode and ionization of residual gases left in vacuum: the dynode chain-related afterpulses, representing the main afterpulse source in standard PMTs, are avoided;

- *Drift and life* are improved. As shown in Sec. 2.1.1, both drift and life characteristics are strongly dependent on gain variations over short and long timescales, respectively. For this reason, they are related to deterioration of the dynodes and caused by variations in the secondary emission ratio, arising in the dynodes only and practically negligible in APDs;

- an excellent *uniformity* is achievable. Indeed, the bombardment gain depends only on the potential difference between the photocathode and the APD (and hence on the applied HV). This means that the photoelectrons generated in correspondence to each point of the photocathode are accelerated to the same energies, thus providing a very uniform response, determined only by the photocathode sensitivity uniformity and the AD gain uniformity.

- *Transit Time Spread* is drastically reduced to typical values of the order of few hundreds of picoseconds. This is related to the short time response of the HPD, due to the very small diode capacitance of the APD;

All these features make HPDs a serious candidate for many photon detection-based applications. In the last years this technology has known a whirling development that led to the realization of many devices, with always better performances and higher sensitive surfaces. Currently, Hamamatsu photonics is developing a 20-inch HPD, a size decisively unimaginable just a couples of year ago.
However, some intrinsic limitations of HPD technology, in particular its limited gain, are boosting the research in the field of photodetectors towards new concepts of devices.

Chapter 3

VSiPMT

As shown in the previous chapter, SiPM technology offers excellent performances and interesting features, making it an extremely valid alternative to standard PMTs. Single photon counting capability, high quantum efficiency, very high internal gain, excellent time response, low power consumption, weak sensitivity to magnetic fields and robustness are just some of the many strong points of SiPMs, that therefore arise as ideal photodetector candidates for all the next generation of astroparticle physics experiments based on scintillation phenomena, Cherenkov or fluorescence radiation.

However, the employment possibilities of SiPMs are strongly limited by their significantly small sensitive surface. Indeed, mostly due to thermal dark currents and to Silicon wafer costs, todays SiPMs have dimensions that never exceed few tens of mm^2. For a SiPM, the dark noise scales almost linearly with the area of the device. For currently commercial SiPMs, the typical value of dark count rate at room temperature is ~ 100 kcps/mm^2. This means that for a 10×10 mm^2 SiPM the expected value of dark count rate is of the order of tens of Mcps. Moreover, a strong increase of dark noise produces an increase of power consumption, optical crosstalk and afterpulse rate.

In order to overcome such limit, and thus to increase the sensitive surface of SiPMs, several approaches can be followed. One possibility can consist in collecting photons, for example by means of a plastic scintillator, and then conveying them towards the SiPM, using wavelength shifting fibers. Such solution would allow to implement both tile scintillation calorimetry in strong magnetic fields and readout of time of flight or trigger scintillators for the next high-energy physics experiments. Alternatively, light could be collected with optical concentrators like Winston cones (Winston and O'Gallagher [2003]) or pyramidal light guides (Barbarino et al. [2012]). However, it has been shown (Barbarino et al. [2011]) that the increase of sensitive surface by means of optical concentrators is paid in terms of overall quantum efficiency and of angular acceptance. For this reason, this solution is suitable only for applications in which the expected light intensity is not extremely low and in which the direction of the incident radiation is known a priori. A different solution to obtain an increased sensitive surface can be the realization of a matrix of SiPM elements on a single substrate. In this kind of solution, to keep the dark count rate as low as possible is a crucial task. Indeed, a parallel connection of the SiPM elements would imply a drastic increase of dark noise, therefore a dedicated readout channel for each single SiPM is mandatory. SiPM matrices have been extensively studied and currently several devices are already commercially available (see for instance

Hamamatsu-Photonics [2014a]). Dimensions up to 16×16 mm^2 have been achieved, while the dead area between the sensitive surfaces of the individual detectors have been significantly reduced, thus optimizing the overall fill factor ($> 60\%$). However, the high dark noise level makes extremely difficult to boost this solution towards the typical sensitive surfaces of PMT technology.

A third approach consists in the combination of the SiPM with the standard PMT technology. This idea leads to a new concept of photodetector, called *VSiPMT* (Vacuum Silicon PhotoMultiplier Tube), combining the excellent performances of SiPMs and the large sensitive surface of PMTs (Barbarino et al. [2008]). Such device is made of a vacuum glass PMT standard envelope, with a photocathode for photon-electron conversion and an electrostatic focusing system that accelerates and focuses the generated photoelectrons towards a small focal area covered by a SiPM. The electron multiplication stage is the heart of the device and undoubtedly represents a revolutionary innovation with respect to the standard PMT technology. Such design is expected to provide many advantages and unprecedented performances, making VSiPMT an outstanding solution for a wide range of applications, especially in the field of astroparticle physics.

Indeed, an electron multiplication stage realized by means of a SiPM instead of a standard dynode chain has many strong features. A SiPM is able to provide a very high internal gain ($10^5 - 10^6$), needing only a small amplification (~ 10) to be comparable (or even higher) with respect to the gain of a typical dynode chain. Photon counting capabilities of SiPMs are nowadays unrivalled, incomparably better than those achievable by PMT dynodes. Time response is faster and no voltage divider is required, thus drastically decreasing the power consumption of the device.

Vacuum glass envelope, photocathode and electrostatic focusing system are standard and well known technologies: the feasibility of the VSiPMT is crucially correlated to the performances of SiPMs as electron multipliers. SiPMs have been invented, developed and optimized for photon detection, therefore in order to test their behavior as electron multiplier a huge preliminary work has been carried on, divided into three steps:

- characterization of a special non-windowed SiPM with a laser source;

- simulation of electron backscattering over SiPM surface;

- test of the SiPM response to an electron source.

The extremely positive results achieved in this preliminary phase encouraged Hamamatsu Photonics, World leader company in PMT and SiPM manufacture, to realize some prototypes of VSiPMT. In the following section some highlights about the preliminary work and an accurate description of the characterization of the prototypes will be provided.

3.1 The preliminary phase

In order to test the feasibility of the VSiPMT it was mandatory to investigate the performances of SiPM as an electron detector. As described in the previous chapter (see Fig. 2.19), all commercial SiPMs have an optical window, realized for protection purposes and with a negligible absorption in the visible regime. Such a surface layer would represent an obstacle for incident photoelectrons, therefore in a VSiPMT a non-windowed SiPM

is required. Hamamatsu has realized a special custom series of SiPMs, not available commercially, without protection layer. In order to investigate the performances of such detector, intended to constitute the heart and the innovative mark of the VSiPMT, the first step of the preliminary phase consisted in full characterization of this SiPM with a laser source.

3.1.1 Characterization with a laser source

The SiPM used in the preliminary phase for the characterization with a laser source and for the following steps is a Hamamatsu S10943-8702 MPPC (see Fig. 3.1). The SiPM

(a)   (b)
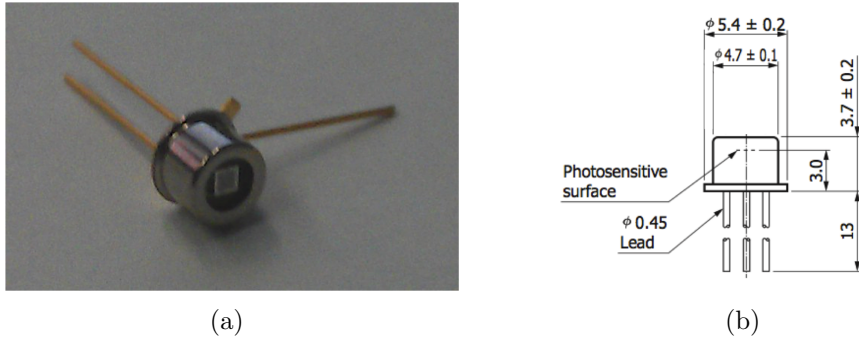
Figure 3.1: (a) Hamamatsu S10943-8702 MPPC - (b) Dimensional outlines

has a total active surface is 1×1 mm^2, with 25 μm pitch for a total of 1600 pixels and a fill factor of 30.8%. The spectral response ranges between 320 and 900 nm, with a peak sensitivity wavelength of $\lambda_p = 440$ nm at which corresponds a PDE of 25%.

The first step consisted in the test of the static characteristics of the device. Reverse and forward current-voltage (I-V) characteristic curves have been obtained, in order to determine the values of the breakdown voltage (V_{BR}) and of the quenching resistance (R_Q). Results are shown in Fig. 3.2.

From the inverse I-V curve, it can be observed that breakdown occurs at $V_{BR} = 70$ V. The value of the global resistance extracted from the forward characteristics is $R_{SiPM} \sim 145 \ \Omega$. Therefore, given the relation:

$$R_{SiPM} = \frac{R_Q}{N_{\mu c}}, \tag{3.1}$$

where $N_{\mu c}$ is the number of pixels, the quenching resistance results to be $R_Q = 230$ kΩ. The experimental setup for the characterization of the SiPM is shown in Fig. 3.3. The light source is composed by a Hamamatsu PLP (Picosecond Light Pulser) mod. C10196 and a by Laser head with wavelength emission $\lambda = 407$ nm. All the tests were performed in a dark box in order to avoid contaminations from background photons. The laser, pulsed at a frequency of 100 kHz, is connected via an optical fiber to a system of two $99\% - 1\%$ beam splitters in cascade configuration, in order to reduce the beam intensity. The 1% output of the first splitter is fed as input to the second stage splitter, whose 1% output is used as light source of the SiPM. In this way, a 10^4 attenuation factor is achieved, allowing to reach extremely low light level, down to single photon condition. The 99% output of the second splitter is sent to a Newport mod. 815 power meter, in
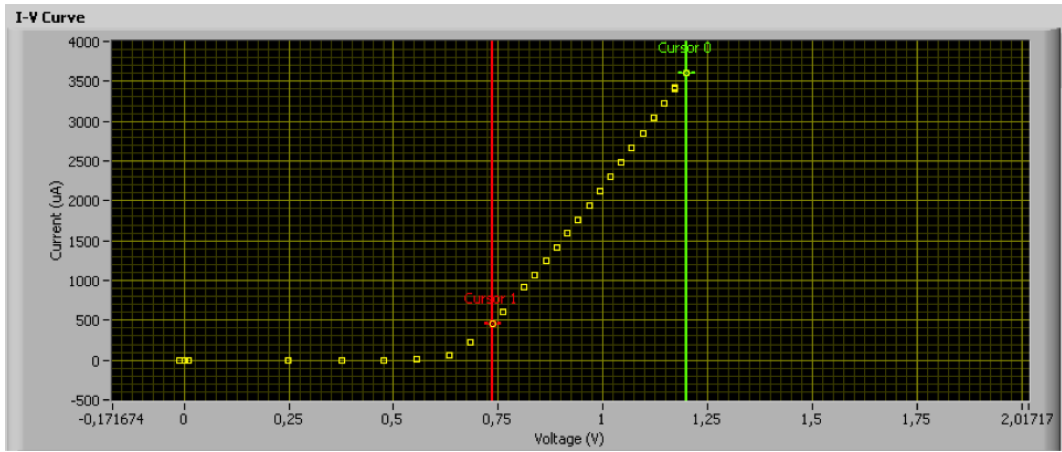
(a)
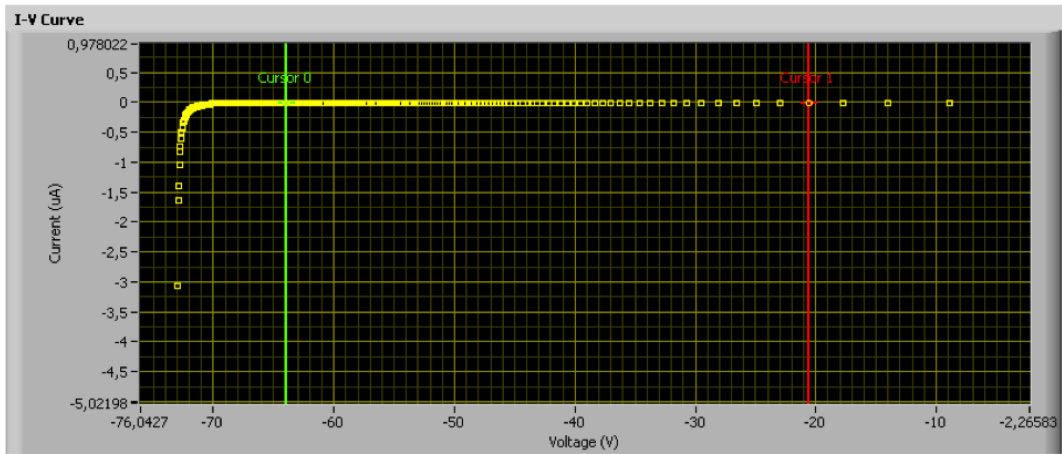
(b)

Figure 3.2: Forward (a) and Reverse (b) current-voltage (I-V) characteristic curves of the SiPM
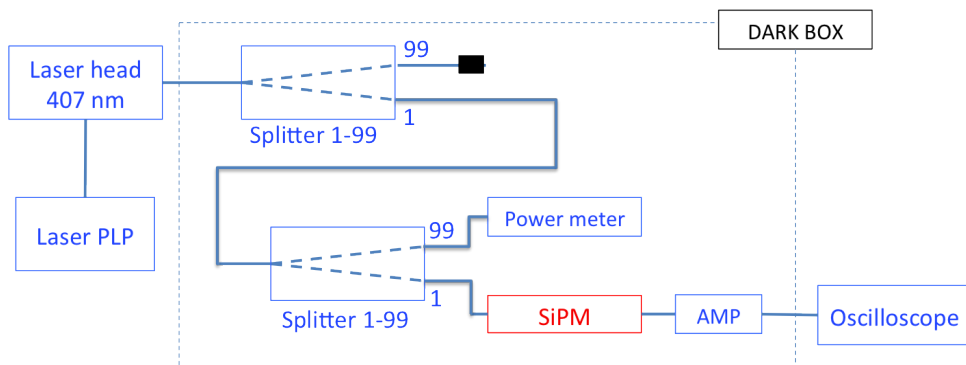
Figure 3.3: Scheme of the bench test for the SiPM with laser source and beam splitters.
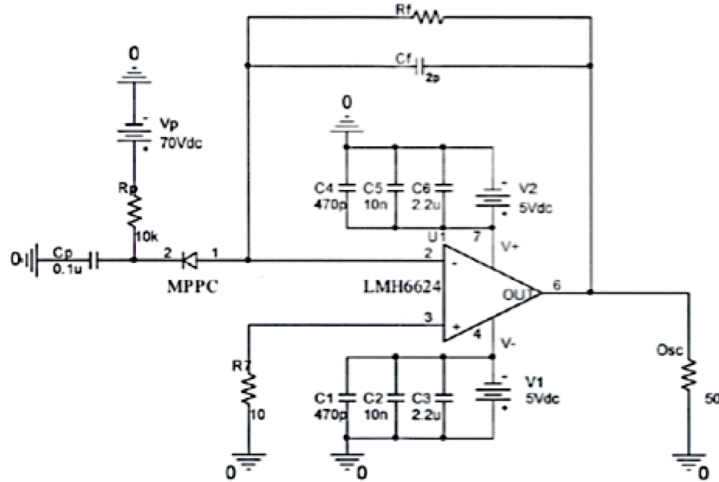
Figure 3.4: Schematic diagram of the SiPM amplification board.

order to monitor the value and the stability of the light source.

The readout circuit of the SiPM is shown in Fig. 3.4. Bias voltage is provided to the SiPM through a polarization resistor $R_P \sim 10 \ k\Omega$ and the output current is fed as input (I_{in}) to a circuit based on an operational amplifier in inverting configuration. The chip used is a LMH6624 by National Semiconductor, powered at $\pm 5 \ V$. The amplifier operates in current-to-voltage mode, therefore the output is directly proportional to the input current flowing through the reaction resistance R_f.

R_f determines the amplification trans-resistance gain, therefore (Barbarino et al. [2011]):

$$V_{out} = -I_{in} \cdot R_f. \tag{3.2}$$

The amplified signal is then sent to a LeCroy WaveRunner 104 Mxi oscilloscope for readout.

In Fig. 3.5 the output signals of the SiPM and the relative amplitude spectrum are shown. The SiPM is kept in conditions of very low intensity incident light and the oscilloscope is triggered in synch with the laser. The responses for multiple triggers are overlaid and the histogram of the peak values for each trigger is displayed. The waveforms corresponding to different numbers of fired pixels are very well distinguishable and the peaks of the histogram are well separated, indicating great gain uniformity and excellent photon counting capabilities of the SiPM under study.

As previously shown in Section 2.5.1, the gain of a SiPM can be calculated as the fraction between the charge of the pulse generated from each pixel during the breakdown process and the charge of the electron. Integrating the output waveforms of the SiPM for each trigger, it is possible to measure the charge of all single pulses. Again, as a consequence of the excellent photon counting performances of the SiPM, the histogram of charge values (shown in Fig. 3.6, blue histogram) exhibits very well separated peaks. The differences between all the possible couples of adjacent peaks correspond to the charge a single fired pixel, therefore the gain of the SiPM can be obtained just dividing these values by the charge of the electron.

The readout circuit in use makes possible to obtain a second estimate of the SiPM gain
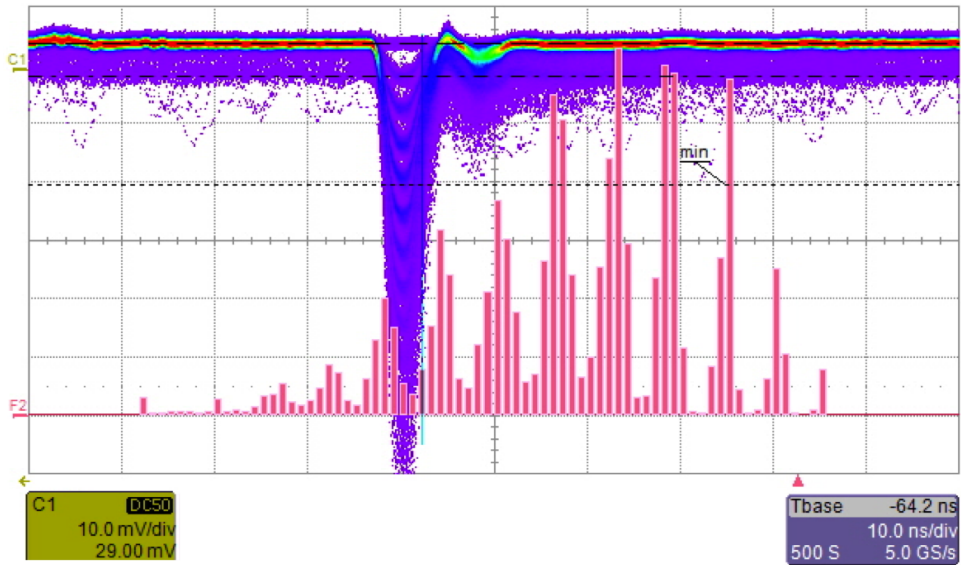
Figure 3.5: SiPM output waveforms and amplitude spectrum.
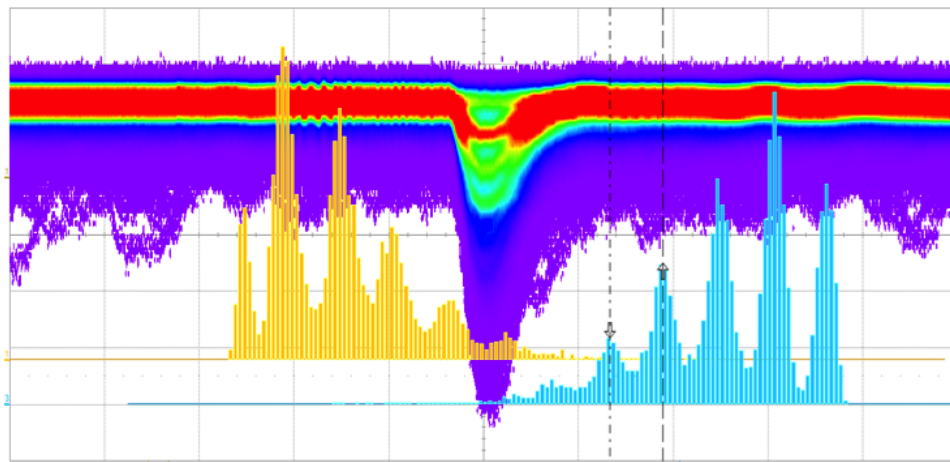
Figure 3.6: SiPM waveforms and gain measurement. Amplitude (yellow) histogram binning: 5 mV. Charge (cyan) histogram binning: 50.0 pVs.
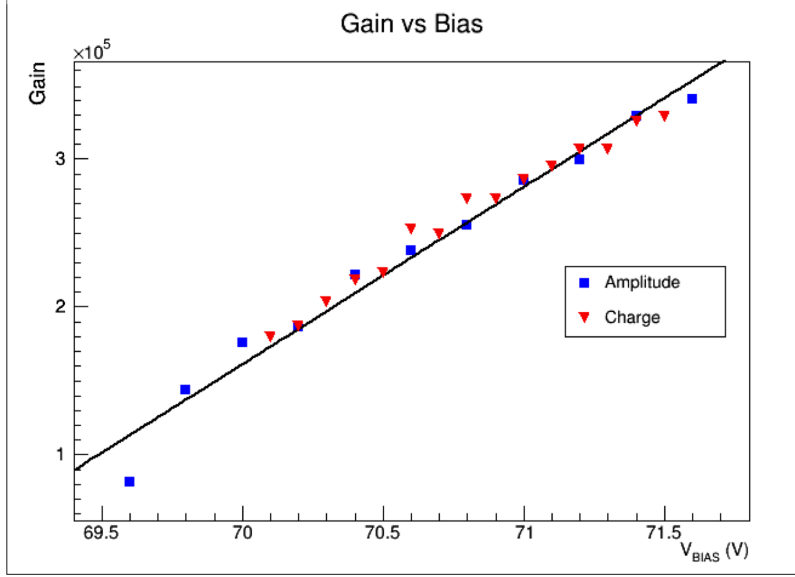
Figure 3.7: Gain vs applied bias calculated with charge and amplitude methods.

with an alternative method, based on the distances between adjacent peaks in the amplitude histogram described above (see Fig. 3.6, yellow histogram). Analogously to the previous case, this difference represents the amplitude of the waveform corresponding to a single photon (V_{1pe}). Indeed, combining Equations 2.16 and 3.2, the following expression of single pixel charge as a function of V_{1pe} can be found:

$$Q = \frac{V_{1pe} \cdot t_f}{R_f},\tag{3.3}$$

where t_f is the fall time of the waveforms. For the SiPM under study, the measured value of fall time at 70.8 V is $t_f = (2.0 \pm 0.5)$ ns.

In order to investigate the dependence of the gain of the SiPM on the applied overvoltage, the gain has been measured with both methods for several values of bias voltage. The results, plotted in Fig. 3.7, show that the gain of the SiPM ranges, depending on the applied bias, between $\sim 2 \times 10^5$ and $\sim 3.5 \times 10^5$ with a very good linearity and an excellent agreement between the two methods used. As a further step, the dark counts rate as a function of the supply voltage has been measured. Results are shown in Fig. 3.8. It can be observed that, for a 0.5 photoelectrons threshold level, the dark count rate varies almost weakly with the applied overvoltage. The measured values, of the order of few hundreds of kcps, are in good agreement with expectations. The characteristics of the SiPM are summarized in Table 3.1.1.

3.1.2 Electron beam simulation

The second step of the preliminary phase consisted in the realization of a Geant4-based simulation (already published in Barbarino et al. [2013b]), aimed at the investigation of the performances of the SiPM as an electron detector.

In such operation mode, the electron-hole pairs are created by ionization. Therefore, photoelectrons impinging on the surface of the SiPM need to be accelerated at energies

72
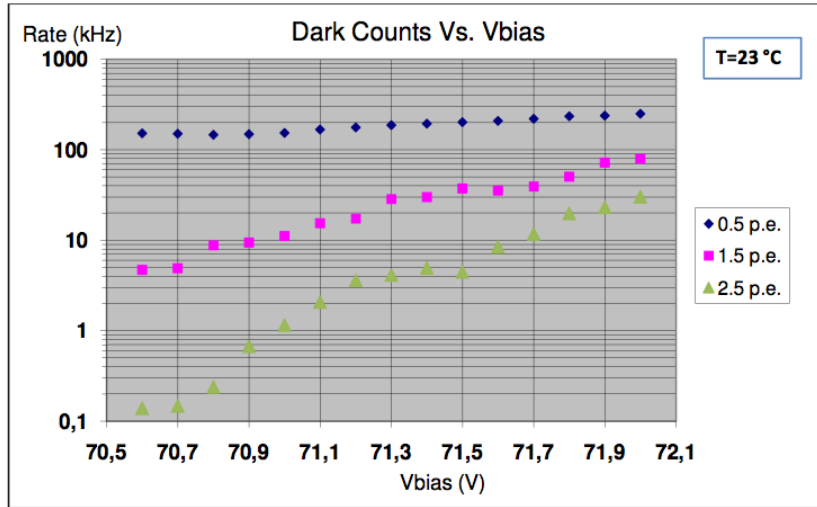
Figure 3.8: Dark counts rate of the SiPM as a function of the supply voltage.

HAMAMATSU S10943-8702

		0.5V o-v	1V o-v
Number of pixels		1600	
Fill Factor		30.8%	
Time resolution (FWHM)		250 ps	
Operating Voltage		70.1 V	
Gain		2.75×10^5	3.00×10^5
Dark Count Rate	0.5 pe	150 kcps	200 kcps
	1.5 pe	5 kcps	15 kcps
	2.5 pe	140 cps	2 kcps
	3.5 pe	75 cps	250 cps
Crosstalk Probability		$< 3\%$	$< 14\%$
Afterpulse Probability		$< 4\%$	$< 16\%$

Table 3.1: Critical parameters of HAMAMATSU S10943-8702 MPPC for 0.5V and 1V overvoltage.

above the energy threshold for the ionization process to occur.

In order to evaluate the electron energy loss in the SiPM, and hence their path inside the device, the most important process that must be taken into account is Multiple Coulomb Scattering (MCS). Indeed, the electron trajectories in Silicon is not a straight line because MCS has the effect to continuously deviate them from their initial direction. Therefore, in order to obtain an estimate of the range of electrons in Silicon, the approach that has been used consists in the so-called Continuous Slowing Down Approximation (CSDA), based on the assumption that electron energy loss in Silicon occurs gradually and continuously, thus neglecting fluctuations in energy loss.

Another important factor to take into account is the backscattering of electrons over the surface of the SiPM. Backscattering can be due to elastic collisions between the electrons of the impinging beam and the atomic nuclei of the target (primary electrons) or to anelastic collisions between electrons and atomic electrons of the medium (secondary electrons). In the low-energy range, the latter is the most relevant energy loss process for electrons. The ratio between the number of backscattered electrons (n_{bs}) and the total number of impinging electrons (n_t) is called *backscattering coefficient* (η) (Cohen et al. [1965]):

$$\eta = \frac{n_{bs}}{n_t}, \tag{3.4}$$

while the *backscattering energy fraction* (q) is defined as the ratio between the backscattered energy and the incident energy of the beam:

$$q = \frac{E_{incident} - E_{released}}{E_{incident}}. \tag{3.5}$$

For a SiPM operating as an electron detector, the concept of PDE is replaced by that of Electron Detection Efficiency (EDE), defined (analogously to Eq. 2.21) as:

$$EDE = (1 - \eta) \times ff \times (P_e + P_h - P_e \cdot P_h), \tag{3.6}$$

where P_e and P_h are the electron and hole breakdown initiation probabilities, respectively. In a n^+pp^+ structure, if the range of electrons in Silicon is too short, the electron-hole pairs are generated before the high field region. In this case, the generated electrons drift towards the n^+ layer giving no contribution to the triggering probability, while the holes pass through the full high field region. Therefore, the triggering probability is given by P_h. Conversely, if electron-hole pairs are generated beyond the high-field region, only electrons contribute to the triggering probability. Considered that the trigger probability for electrons is about a factor 2 higher than that for holes, the second case is preferable. The optimal case is that in which the pair is generated inside the high field depletion region. Indeed, if this condition holds, both carriers, traveling in opposite directions, contribute to the avalanche triggering probability, that therefore is maximized.

A reduced thickness of n^+ layer would allow to maximize the triggering probability for lower electron ranges, while a SiPM with a p^+nn^+ structure would be better optimized for electron detection. Indeed, in this case the probability that the breakdown is due to electrons is higher, thus implying a higher triggering probability.

The electron backscattering and the optimal energy required to maximize the triggering probability have been investigated by implementing a Geant4-based simulation. For the incident electron beam, several combinations of initial energies (ranging from 1 to 20

keV) and directions (from 0° to 75°) have been considered, simulating all the typical low-energy electromagnetic processes. Interaction processes have been simulated using as a reference the G4EmLivermorePhysics model, obtained by the combination of the model for standard electromagnetic processes with the model for low-energy electromagnetic processes and validated in the range from 990 eV to 100 GeV. The SiPM has been modeled as a 5 mm Silicon box, with a 0.15 μm deep SiO_2 resistive surface layer.

In the first set of simulations, a normally incident electron beam has been considered, with different energies ranging between 1 and 20 keV. Backscattering coefficient (η), backscattering energy fraction, total released energy and range of electrons in Silicon have been estimated, as shown in Fig. 3.9. Based on these simulations, it was found that

(a)

(b)

(c)

(d)
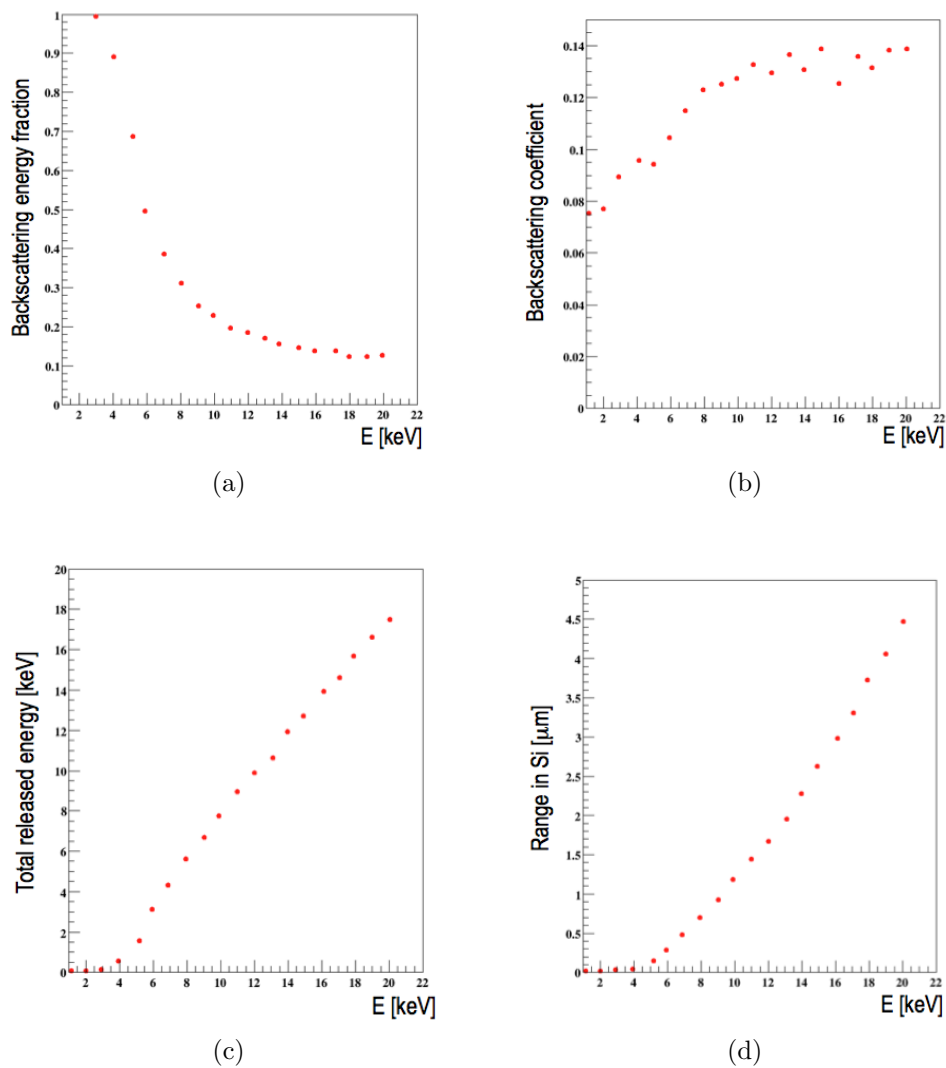
Figure 3.9: (a) Backscattering energy fraction - (b) Backscattering coefficient - (c) Total released energy - (d) Range of a normally incident electron beam as a function of the incident energy.

the backscattered energy fraction for a normally incident electron beam decreases as the incident beam energy increases, the backscattering coefficient grows from 0 to 10 keV and

then it reaches a plateau region, while the range in Silicon increases with the incident energy. In particular, it was possible to observe that the energy threshold for electrons to penetrate inside the SiPM and to produce electron-hole pairs in the p layer is given by $E_{thr} = 10$ keV. Indeed, at this energy, normally incident electrons penetrate for 1.2 μm inside Silicon, with a reduced backscattering coefficient ($\eta = 12.6\%$). Therefore, at 10 keV the expected value of the EDE is given by:

$$EDE_{10keV} \approx ff \times (1 - \eta_{10keV}) = 0.308 \times 0.874 \approx 27\%. \tag{3.7}$$

In a second run of simulations, electron beams with energy equal to E_{thr} and angle of incidence θ varying between 0° and 75° have been simulated. Again, backscattering coefficient (η), backscattering energy fraction, total released energy and range of electrons in Silicon have been estimated. Results as shown in Fig. 3.10.

(a)   (b)

(c)   (d)
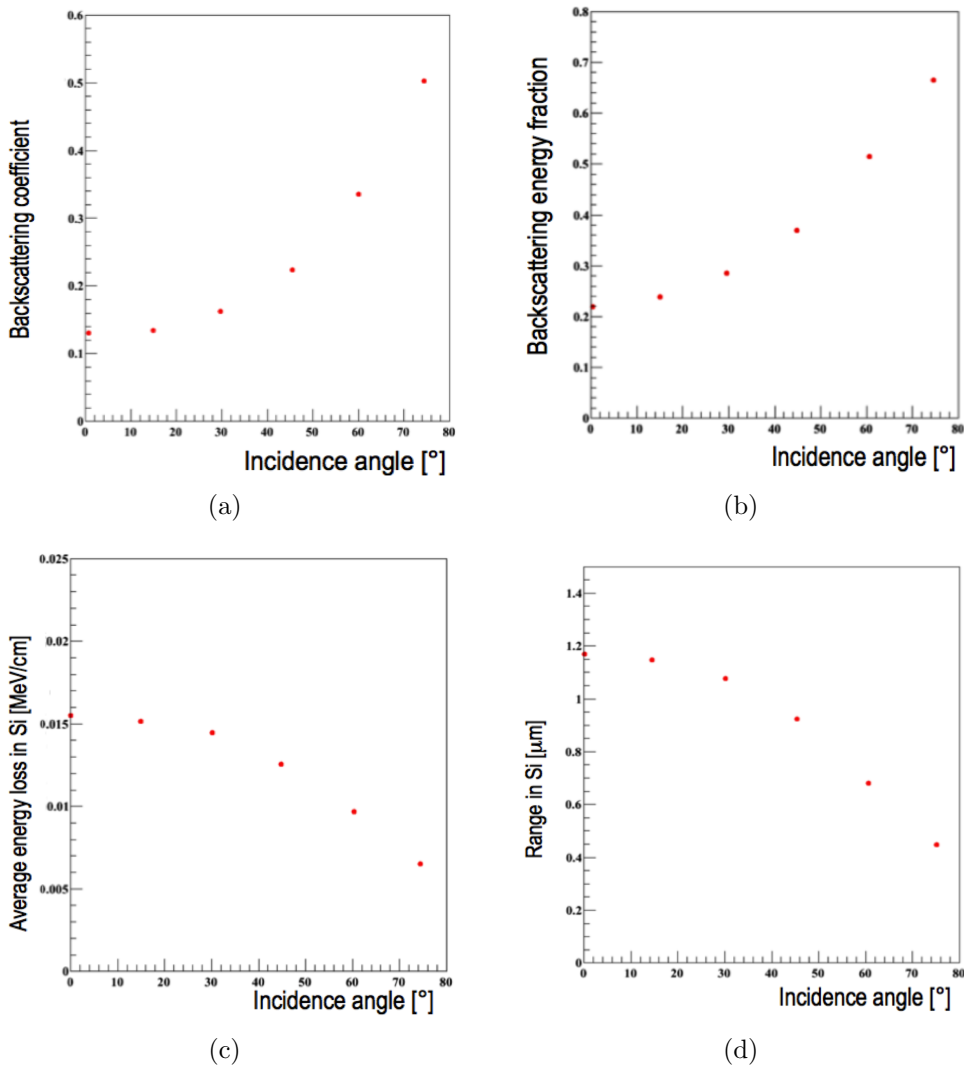
Figure 3.10: (a) Backscattering coefficient - (b) Backscattering energy fraction - (c) Average energy loss in Silicon - (d) Range of a 10 keV electron beam as a function of the angle of incidence

This simulation shows that the performances of the SiPM as an electron detector get
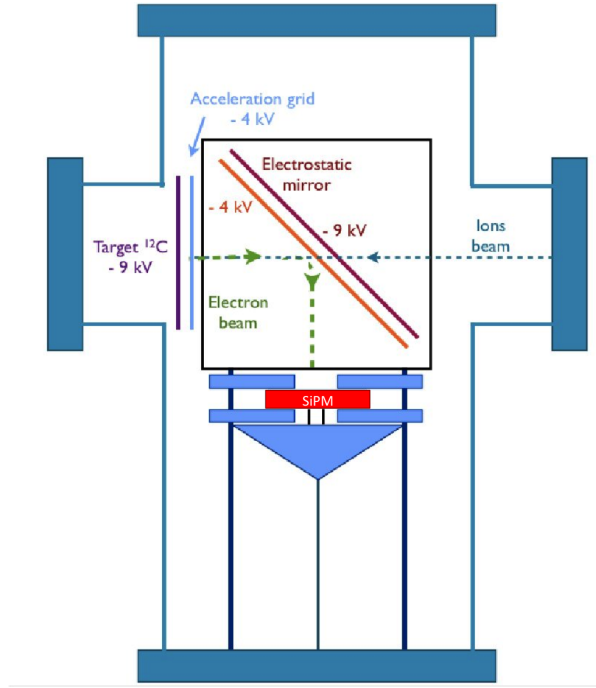
Figure 3.11: Experimental setup: an ion beam scatters over a carbon foil. Backward electrons are accelerated and deflected by a set of electrostatic grids towards the SiPM.

significantly worse as the angle of incidence of the electrons increases. Indeed, for a fixed electron beam energy of 10 keV, as the angle of incidence increases, the average energy loss in Silicon and the range in Silicon of electrons decrease while the backscattering coefficient and the backscattered energy fraction drastically increase ($\eta = 12.6\%$ and $q = 0.22$ for normal incidence, while $\eta \sim 50\%$ and $q = 0.68$ for $\theta = 75°$).

3.1.3 Electron beam test of SiPM

The last step of the preliminary phase consisted in the test of the response of the SiPM to an incident electron beam. According to the results obtained by the Geant4-based simulation, in order to optimize the penetration of electrons in Silicon, and thus to maximize the triggering probability, it is required to accelerate the beam up to energies of ~ 10 keV.

The experimental setup and the results of the test have already been published in Barbarino et al. [2013a]. In order to extract and accelerate the electron beam to the required energy, it has been realized the experimental setup shown in Figure 3.11.

An ion beam is extracted in a TTT-3 linear accelerator and used to bombard a thin (30μg /cm^2) ^{12}C foil. In the collisions between ions and target atoms in the carbon foil, excited electrons are created, transported through the bulk to the surface and finally transmitted through the surface potential barrier. In such scattering processes, forward and backward secondary electrons can be emitted.

The test has been performed collecting the backwards electrons, accelerating them up to 9 keV and sending them towards the SiPM, that is grounded. In order to avoid the SiPM to intercept the incident ion beam and backscattered protons, a deflection of the
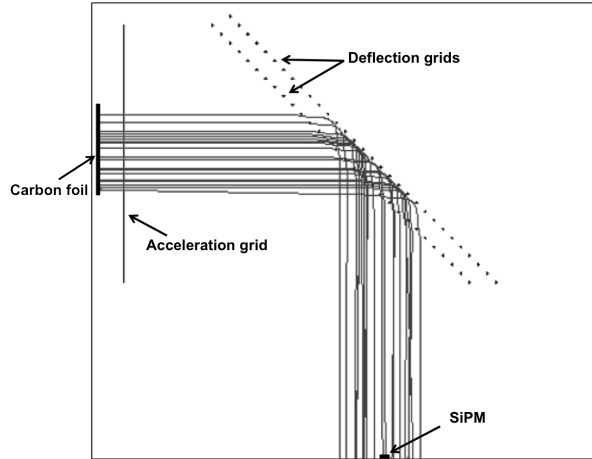
Figure 3.12: Monte Carlo simulation of electron trajectories.

electron beam is required. Acceleration and deflection of backward electrons are achieved by means of a system composed by an electrostatic grid and an electrostatic mirror.

The electrostatic grid is kept at -4 kV and exploits the potential difference with respect to the ^{12}C target to collect and accelerate the backward electrons towards the electrostatic mirror. The latter is composed by two plane and parallel grids, oriented at 45° with respect to the direction of the incident electron beam. The first grid of the mirror has the same potential of the acceleration grid while the second one has the same potential of the carbon foil. In this way, the electron beam is deflected with an angle of emission equal to the angle of incidence as shown in the Monte Carlo simulation in Fig. 3.12, thus realizing a 90° overall deflection.

The test consisted in the bombardment of the ^{12}C foil with an 8 MeV $^{3+}$C beam and with a 2 MeV proton beam, in order to obtain an evidence of the electron counting capability and an estimate of the efficiency of the SiPM. As shown in Barbarino et al. [2013a], the SiPM exhibits a good electron counting capability and a value of the efficiency in accordance with the value expected on the base of the Geant4-based simulation.

3.2 VSiPMT prototypes

The extremely encouraging results obtained in the preliminary phase convinced Hamamatsu Photonics, World leader company in the field of photodetectors for both PMT and SiPM technologies, to realize two prototypes of VSiPMT.

The working principle of the device is shown in Fig. 3.13 (bottom right picture): the incident photons pass through a Borosilicate Glass square window (7×7 mm^2) and impinge on a circular GaAsP photocathode (3 mm diameter), where photo-electron conversion occurs. The entrance window does not transmit ultraviolet radiation (the cut-off wavelength is ~ 300 nm), with a refractive index of 1.50 at 400 nm. The spectral transmittance curve is reported in Fig. 3.14.

The GaAsP (Gallium Arsenite Phosphate) photocathode offers high quantum efficiency optimized for the detection of visible light. Fig. 3.15 shows the photocathode spectral response: the peak value of QE, corresponding to an incident wavelength of $\lambda \approx 500$
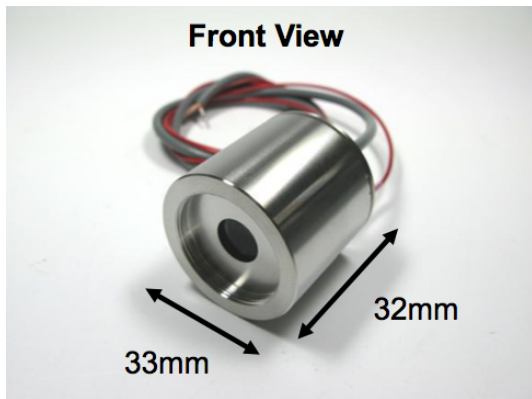
(a)
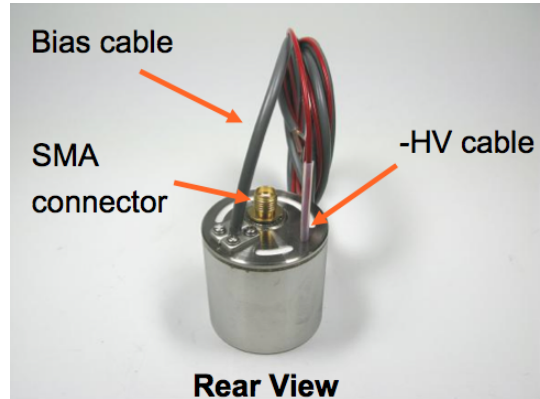
(b)
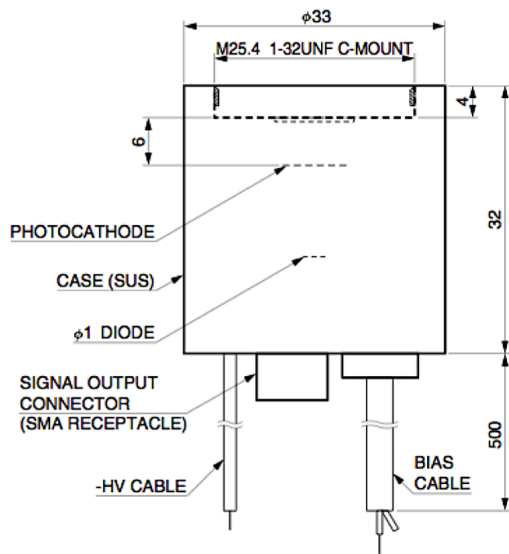
(c)
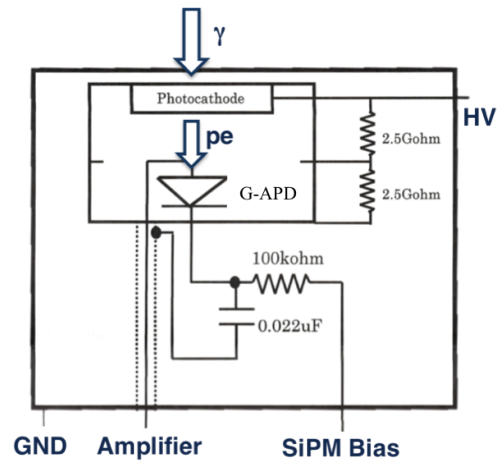
(d)

Figure 3.13: VSiPMT prototypes: Front view picture (a) - Rear view picture (b) - Dimensional outlines (c) - Working principle (d).
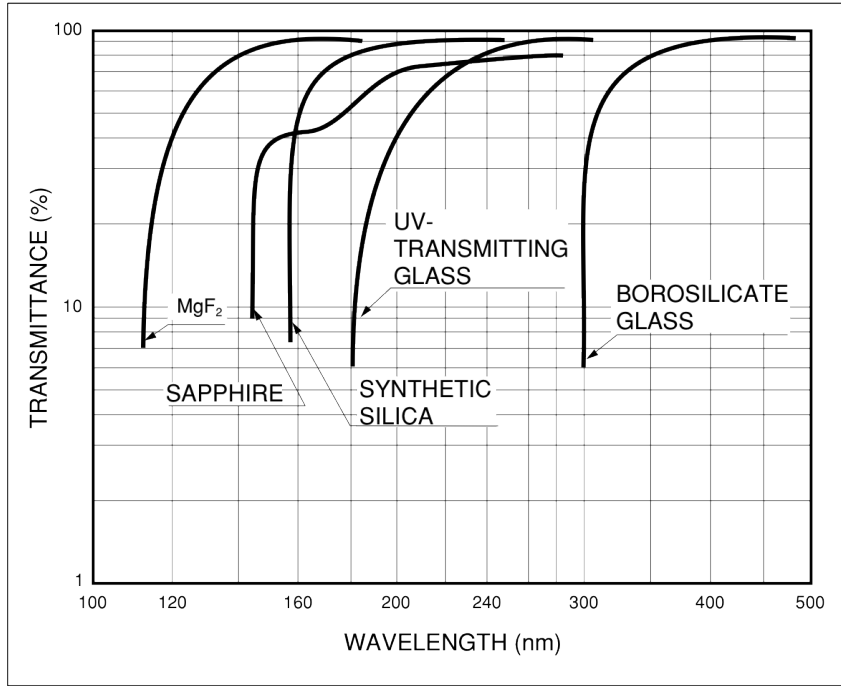
Figure 3.14: Spectral transmittance of window materials.

nm, is actually coincident with the theoretical 50% maximum quantum efficiency of a photocathode-based device. The generated photoelectron are then focused towards a G-APD where the electron multiplication process takes place. As shown in Fig. 3.13 (bottom right picture), the single stage focusing system is composed by a focusing ring kept at half potential with respect to the HV applied to the photocathode, through a two-resistors voltage divider circuit (2.5 GΩ each).

The system is housed into a cylindrical (diameter: 33 mm , length: 32 mm) Steel Use Stainless (SUS) case, with only three connections: two power supply cables (one for the photocathode HV the other for the G-APD bias) and one SMA connector for output signal readout (see Fig. 3.13, top pictures). On the top of the cylindrical case, a C-MOUNT thread has been realized in order to facilitate the connections to other devices.

Hamamatsu has realized two prototypes, both with an electron multiplier stage composed by a special 1×1 mm^2 MPPC without protective entrance window (in order to maximize electron penetration inside Silicon) and realized in a p^+nn^+ configuration for EDE optimization, as previously explained. For this reason, a lower value of E_{thr} is expected, with respect to the results of the simulations described in Section 3.1.2. The only difference rely in the different pitch of the two MPPCs used: in the first one (serial number ZJ5025) the pixel size is of 50 μm, for a total of 400 pixels, while the second one (serial number ZJ4991) has a pitch of 100 μm, for 100 pixels in total. The static characteristics of the devices are shown in Fig. 3.16.

The two prototypes have been extensively studied, in order to investigate the performances and the limits of the devices. The characterization consisted in the following tests:

- SPE response;

80

Photocathode Spectral Response
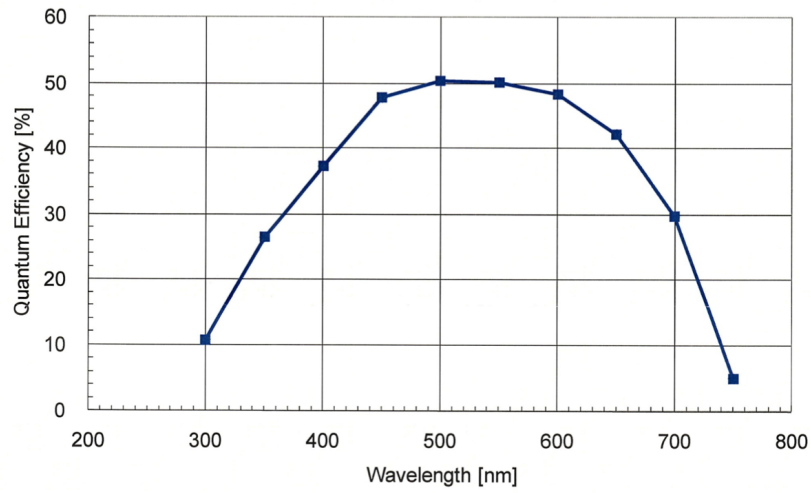
Figure 3.15: Photocathode spectral response.
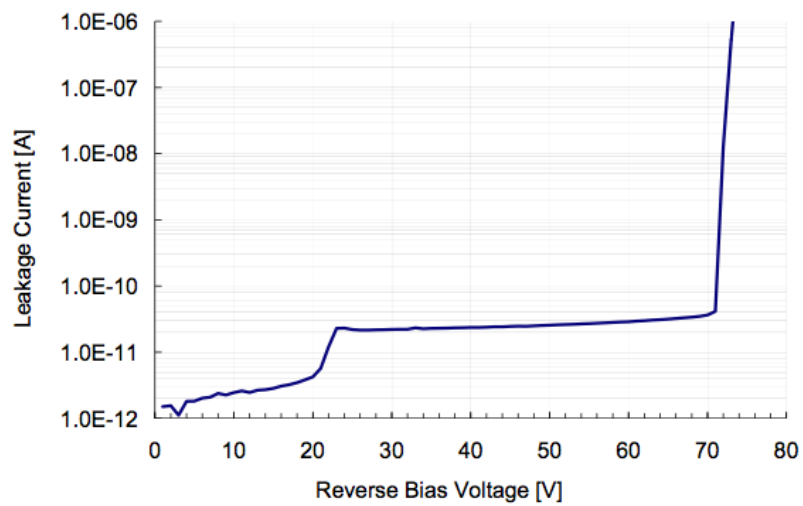
Figure 3.16: Leakage Current.

81

- photon spectra;

- time stability;

- gain;

- detection efficiency;

- dark counts;

- afterpulses;

- response homogeneity;

- Transit Time Spread.

In the following sections a detailed description of the experimental setup and of the results will be provided.

3.2.1 Detector front-end

The output signal of the G-APD, as measured in the preliminary phase (see Section 3.1.1), has an amplitude of the order of few milliVolts. Therefore, an adequate amplification stage is required in order to drive a transmission line towards the acquisition electronics. The requirements for the amplification circuit are mild for what concerns the amplification coefficient (a factor $10 - 20$ is enough), while timing constraint are more stringent. The output signal of the device has a very short rise time (of the order of few nanometers), therefore a high frequency amplifying circuit is required.

Three amplifiers have been realized, with gains of 10, 15 and 20, respectively. The amplification circuit (basic scheme shown in Fig. 3.17, right panel) is based on a 5 GHz Operational Amplifier (AD8009 OpAmp by Analog Device) used in non-inverting configuration, with a 50 Ω input impedance and driving a 50 Ω output line.

Due to the very high impedance of the divider (5 GΩ), the current driven from the supply is very low (of the order of a half μA), so the power needed for the High Voltage supply is negligible. Therefore, the amplifier circuit is the main power dissipation source for a VSiPMT. The measured power consumption is below 5 mW, a value significantly low if compared to the power consumption of a standard PMT voltage divider. Undoubtedly, this represents one of the most important advantages of VSiPMT technology.

3.2.2 The experimental setup

The experimental setup realized for the characterization of the two prototypes is schematically shown in Fig. 3.18. The light source is composed by a Hamamatsu PLP (Picosecond Light Pulser) mod. C10196 and a by Laser head with wavelength emission $\lambda = 407$ nm and pulse duration of 85 ps. The laser light is driven through an optical fiber inside a shielded dark box, where the tests have been performed. The intensity of light is regulated by means of a U-bench fiber port with a system of calibrated grey filters (the variable attenuator in Fig. 3.18, see also Fig. 3.19, left picture). After the attenuation stage, the light is split in two channels: the first one is used to illuminate the VSiPMT,

(a)   (b)
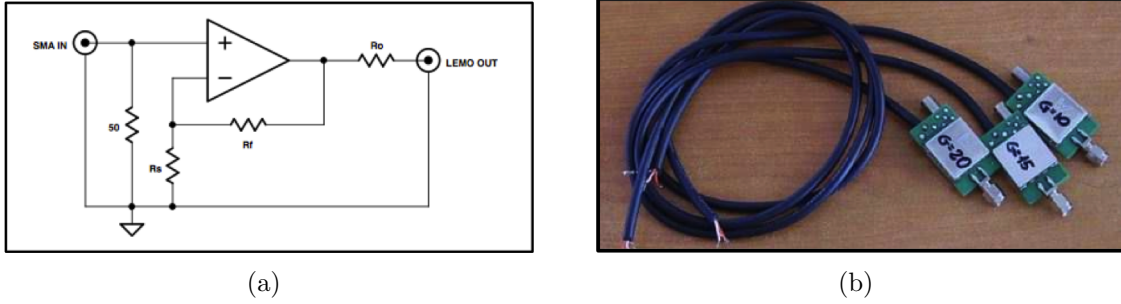
Figure 3.17: VSiPMT output signal amplifiers: Schematic circuit (a) - The three amplifiers realized (b).
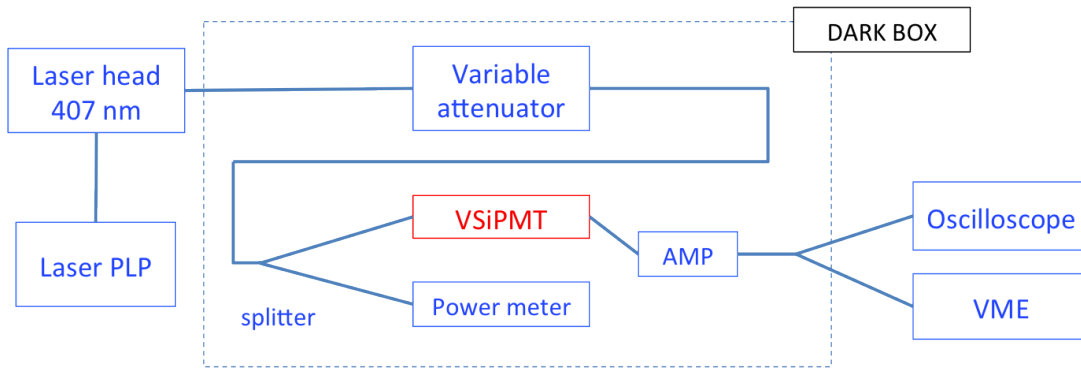
Figure 3.18: Experimental setup for the characterization of VSiPMT prototypes.

while the second one is sent to a Power Meter probe (Newport Model 2936-C, ~ 10 fW resolution) in order to measure the value of the laser output and to monitor its stability during data taking. The VSiPMT is connected directly to the optical fiber by a FC/PC to C-MOUNT adapter, guaranteeing for perfect alignment and good stability (see Fig. 3.19, right picture). The output signal of the VSiPMT is amplified by the circuit described in the previous section and then sent, through a lemo cable, to both an oscilloscope (LeCroy WaveRunner 104 Mxi, 1 GHz Analog Bandwidth, 8 bit resolution) and a VME chain, based on a flash ADC Waveform Digitizer (CAEN V1720E, 8 Channel 12bit 250 MS/s).

3.2.3 Photon spectra

Fig. 3.20 shows a typical output waveform of the 50 μm device (ZJ5025): the pulse has a very short rise time (of the order of the nanosecond) and a fall time of ~ 40 ns. The 100 μm pitch prototype (ZJ4991) has the same rise time but a larger fall time ($\tau_R = C_D R_Q \approx 100$ ns), due to the larger diode capacitance (C_D) arising from the larger active volume of each micro-cell.

The photon counting capabilities of the VSiPMT have been investigated illuminating the photocathode with a very low intensity laser beam. The oscilloscope-based data acquisition has been performed using the synchronization signal of the laser source as trigger and overlaying the responses for multiple triggers in an infinite persistency. Fig. 3.21 shows the output waveforms of the ZJ5025 device and the corresponding amplitude spectrum.
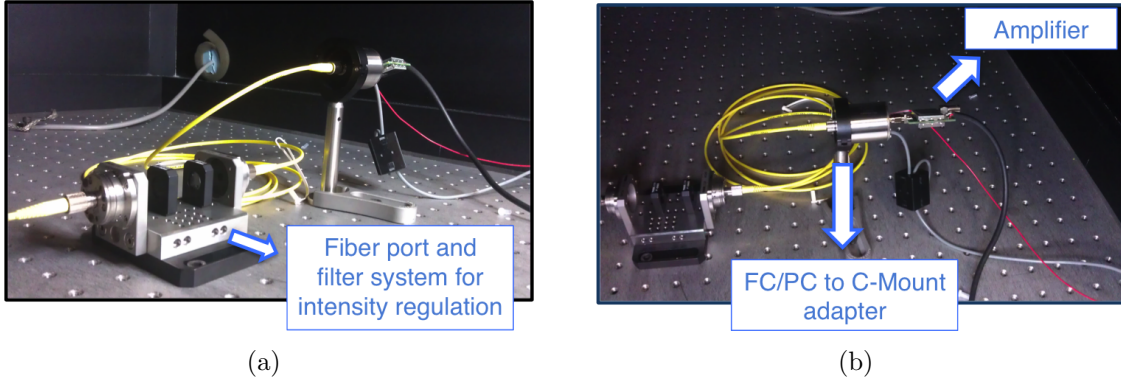
Figure 3.19: Light intensity regulation system (a) - VSiPMT-fiber connection (b).
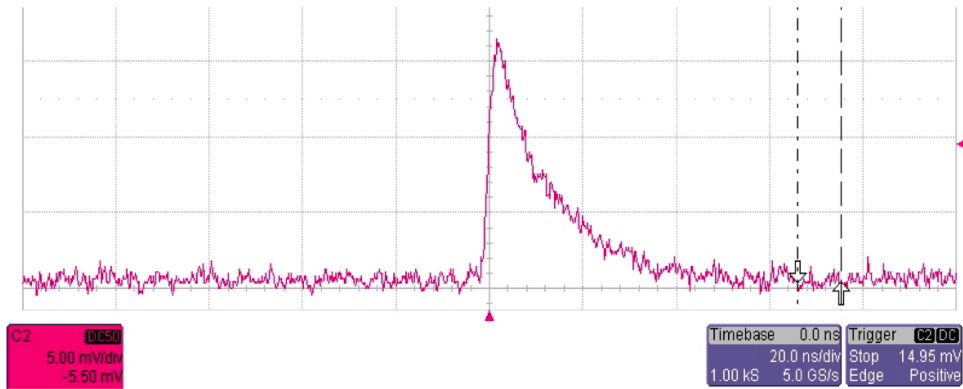
Figure 3.20: Typical ZJ5025 output waveform.
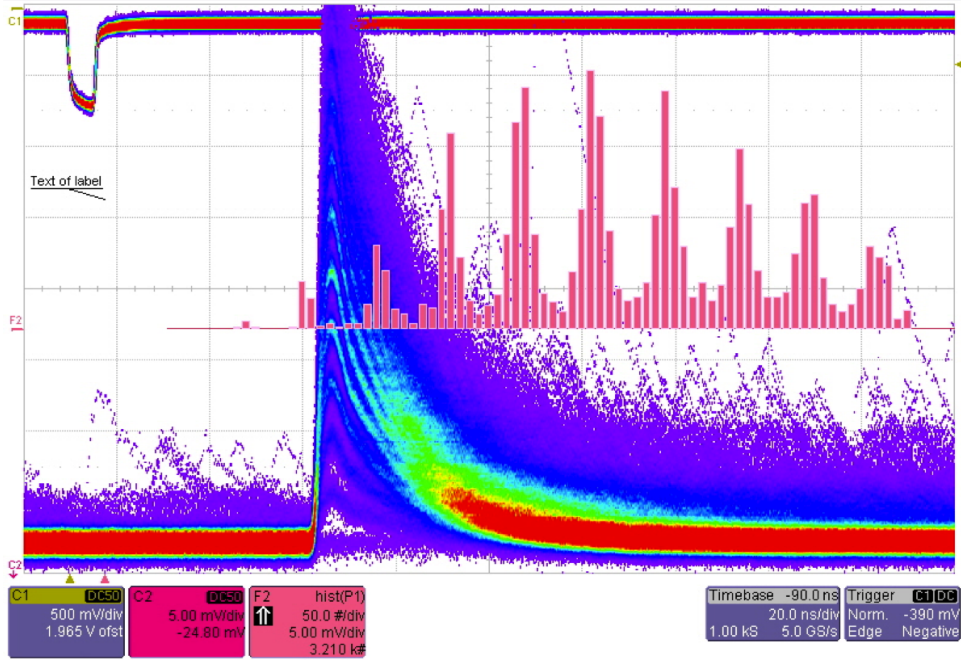
Figure 3.21: ZJ5025 output waveforms and amplitude spectrum.
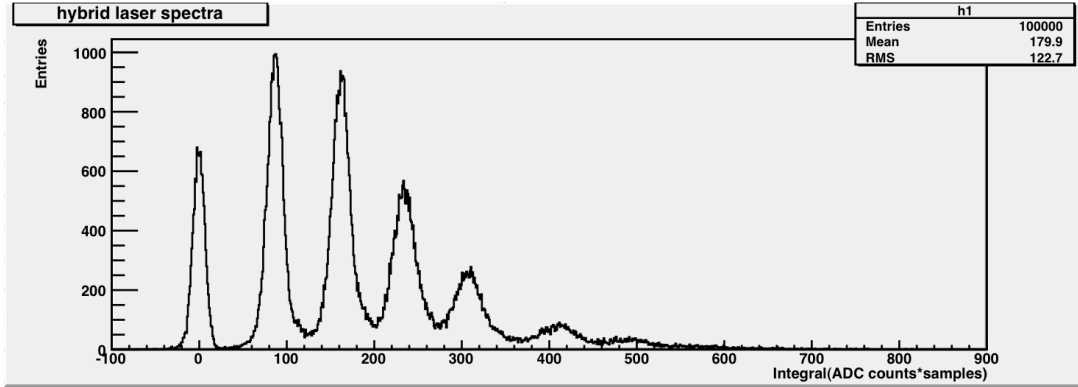
Figure 3.22: ZJ5025 charge spectrum.

Waveforms corresponding to different numbers of fired pixels are very well separated, the same for the peaks in the amplitude spectrum. This is a demonstration of the **excellent photon counting capabilities** of the VSiPMT prototypes. In the waveforms collected in Fig. 3.21 it is possible to count separately the number of events ranging from single fired pixel to nine fired pixels condition, a performance simply unreachable by standard PMTs and even by the recently developed HPDs.

A similar measurement has been performed by means of the VME DAQ chain (results are shown in Fig. 3.22). In this case, the VSiPMT was kept under slightly lower light intensity conditions. 100.000 waveforms have been acquired and for each of them the integral in a time window of 100 ns has been calculated, after subtracting the value of the baseline introduced by the amplification circuit. The resulting charge spectrum confirmed the outstanding photon counting performances of the device.

3.2.4 SPE response and stability

Investigating the response of the two prototypes under Single Photo-Electron (SPE) conditions allowed to measure two crucial parameters: the peak-to-valley ratio and the SPE resolution. The results (shown in Fig. 3.23) are excellent: the measured value of peak-to-valley ratio is 65, with an improvement factor of several tens (≈ 30) with respect to a standard PMT, while the measured SPE resolution (less than 18%) turns out to be improved of a factor ≈ 2. These results imply that for a VSiPMT a far better signal discrimination is achieved, since it is better separated from the background with respect to the PMT case.

In order to study the time stability of the SPE response of the two prototypes, 100.000 waveforms with low intensity laser light have been acquired every 20 min for 20 hours. As shown in Fig. 3.24, the VSiPMT exhibits an extremely stable SPE response, with a mean deviation not exceeding the 2% over the whole data-taking period.

The time stability of the two prototypes has been investigated also for high intensity illumination, in order to investigate possible fatigue effects of the device. The Multi-photon response of two prototypes has been studied setting three different light levels (corresponding to 26, 52 and 65 photoelectrons, respectively) and acquiring for each of them 100.000 waveforms every 20 minutes for 100 minutes in total. The results shown in Fig. 3.25 indicate that, for all the three different incident light levels, NO drop in

85
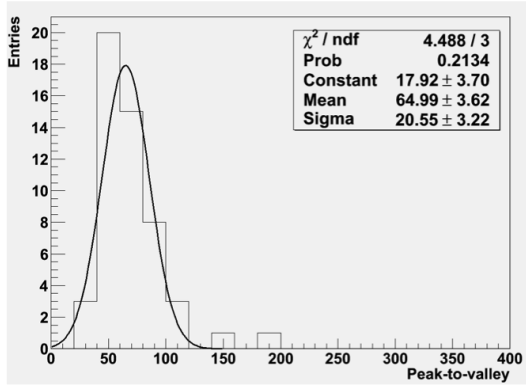
(a)
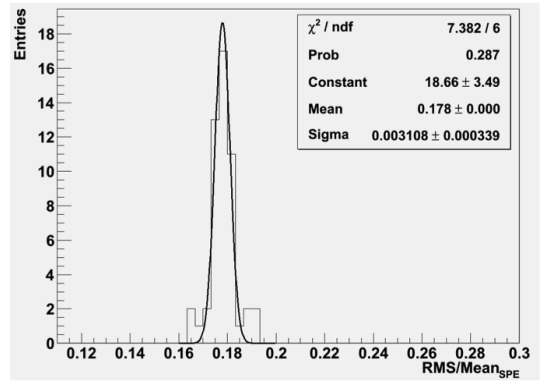
(b)

Figure 3.23: VSiPMT SPE response: Peak-to-Valley ratio (a) - SPE resolution (b).
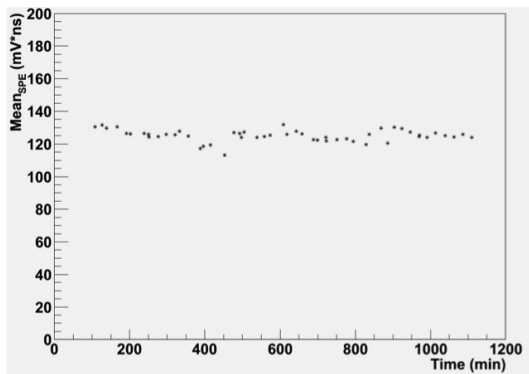
(a)
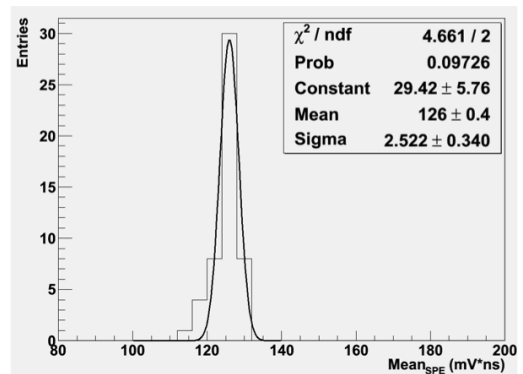
(b)

Figure 3.24: VSiPMT time stability: SPE response over time (a) - SPE response distribution (b).
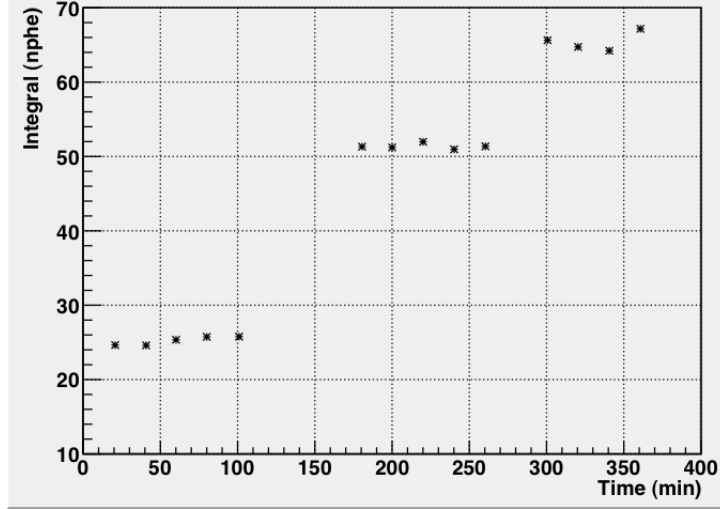
Figure 3.25: ZJ4991 Multi-photon response.

the multi-photon response on the 100 minutes of data-taking time can be observed. This means that on this time scales the VSiPMT shows NO fatigue effect on high illumination.

3.2.5 Detection Efficiency

The Photon Detection Efficiency (PDE) of the VSiPMT can be defined as the product of the photocathode Quantum Efficiency (QE) and the G-APD Electron Detection Efficiency (EDE):

$$PDE_{VSiPMT} = QE_{photocathode} \times EDE_{G-APD}. \tag{3.8}$$

However, neglecting the contribution of backscattering and under the reasonable assumption that for photoelectrons with energy above the energy threshold defined in Sec. 3.1.2 the Geiger avalanche trigger probability is 1, the EDE of the G-APD can be considered, in a first approximation, to be coincident with the fill factor (see Eq. 3.7). Therefore, the PDE of the VSiPMT turns out to be:

$$PDE_{VSiPMT} = QE_{photocathode} \times ff_{G-APD}. \tag{3.9}$$

The fill factors of the two G-APDs for the ZJ5025 and the ZJ4991 prototypes are 0.61 and 0.78, respectively. Therefore, correspondingly to the wavelength of the laser source in use (≈ 0.38 @ $\lambda = 407nm$, see Fig. 3.15), the following values of PDE are expected:

$$PDE_{ZJ5025} = QE_{photocathode} \times ff_{G-APD} = 0.38 \times 0.61 \approx 0.23 \tag{3.10}$$

$$PDE_{ZJ4991} = QE_{photocathode} \times ff_{G-APD} = 0.38 \times 0.78 \approx 0.30 \tag{3.11}$$

For each prototype, a measurement of the PDE as a function of the HV applied to the photocathode has been performed. Keeping the devices under very low light conditions (few photons per pulse), the PDE has been calculated as the ratio between the output signal

87
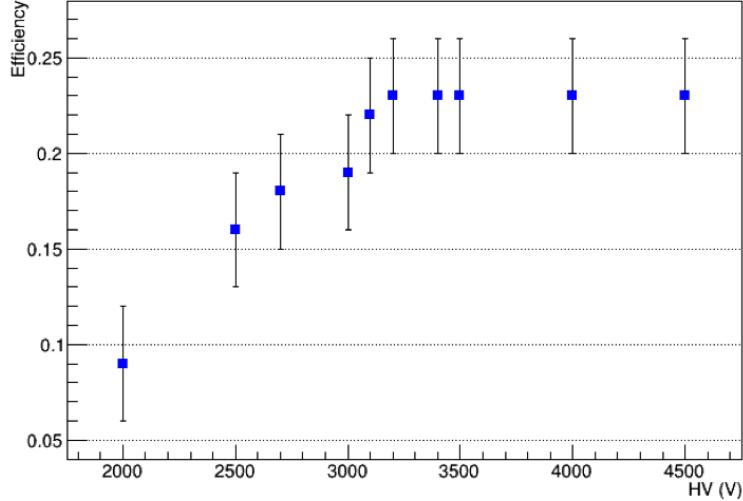
Figure 3.26: PDE of the ZJ5025 prototype as a function of photocathode HV.

of the VSiPMTs and the incident laser beam intensity, measured by means of the power meter. The resulting curve, shown in Fig. 3.26, exhibits a linear trend until it reaches a plateau region at -3.2 kV, extending beyond -4.5 kV. Therefore, it is possible to conclude that for the p^+nn^+ G-APD in use the energy threshold is $E_{thr} = 3.2$ keV, a value that is, as expected and predicted, significantly lower with respect to the simulated 10 keV energy threshold for a standard n^+pp^+ G-APD. Moreover, the wide plateau region indicates that the performances of the VSiPMT are independent on the High Voltage applied to the photocathode, representing an outstanding breakthrough and an unprecedented feature in the field of large surface photodetectors. Indeed, as shown in the previous chapter, for both standard PMTs and HPDs a strong relationship between HV and gain holds. Simply, this is not true for a VSiPMT. The reason is that in the case of a VSiPMT the high gain is obtained only by means of the Geiger avalanche process inside the G-APD. For all the photoelectrons accelerated to energies above E_{thr}, the range in the Silicon is high enough to let them reach the depletion region and hence to generate the avalanche breakdown process. Unlike HPDs, no electron bombarding gain is required, therefore in a VSiPMT the HV is needed only to accelerate the photoelectrons above the threshold and to transfer them towards the G-APD. This means that, in order to achieve a stable gain, for a VSiPMT it is mandatory to stabilize only the G-APD bias voltage, responsible of the Geiger breakdown process, without the high voltage stabilization required for PMTs and HPDs. This represents a very strong advantage, considered that an easy-to-stabilize gain is a key feature in practically all applications.

The low value of E_{thr} (with respect to the simulations results) obtained with a p^+nn^+ structure is further reducible just reducing the thickness of the SiO_2 surface layer of the G-APD. In this way, it would be possible to reach the plateau region at even lower photocathode voltages.

After setting the energy threshold, the efficiency uniformity of the photocathode has been tested. It has been realized a XY scan of the entrance window surface by means of a micro-metric two-axes motorized pantograph integrated in an automatic DAQ system (see Fig. 3.27, left picture). The 7×7 mm^2 square surface of the window has been

scanned at steps of 0.2 mm and for each step the value of the PDE has been measured. Results shown in Fig. 3.27 (right picture) indicate that over all the surface of the 3 mm $\varnothing$ photocathode the PDE is very uniform, in each point ranging between 20% and 25%, with only few boundary effects.

(a)   (b)
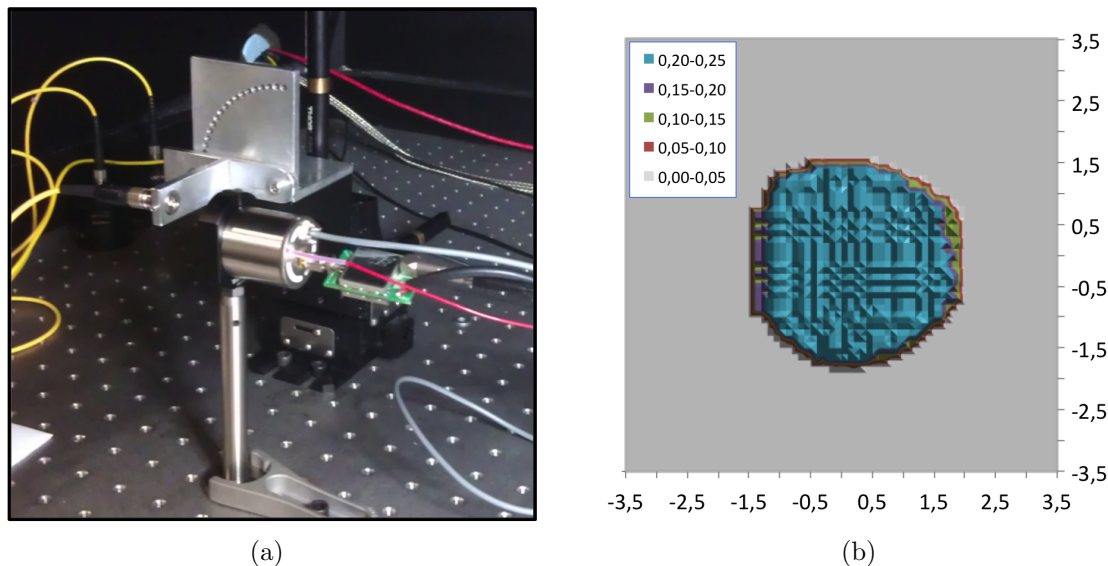
Figure 3.27: ZJ5025 prototype XY scan: experimental setup (a) - results (b).

3.2.6   Gain

As for a PMT, also in the case of the VSiPMT the gain is given by the electron multiplying stage. Therefore, for the two prototypes under test the gain coincides with the gain of the G-APDs.

As described in Sec. 2.5.1, the gain of the G-APD can be defined as the fraction between the charge of the pulse generated from each pixel during the breakdown process and the charge of the electron. Following the same approach used in the preliminary phase characterization (Sec. 3.1.1), the charge of a single fired pixel can be calculated as the difference between all the possible couples of adjacent peaks in the charge spectrum shown in Fig. 3.22. Setting a fixed HV value of -3.2 kV for the reasons discussed in the previous Section, a measure of the G-APD gain as a function of the applied reverse voltage in the range 72.1 V - 73.0 V has been performed. The resulting curve (shown in Fig. 3.28) exhibits a very linear trend, with values ranging between 4×10^5 and 8×10^5, in fairly good agreement with expectations. The uncertainty on the gain, estimated from the least observable error of 1 mV over a signal on the oscilloscope trace, is very simple to propagate to the calculated charge, and leaded to a 7% error, not shown in the graph. Therefore, considering the additional gain provided by the amplifying circuit, the overall gain of the two prototypes under test ranges between 10^6 and 10^7. These values are comparable with the gain of a standard PMT, with the strong advantage of a much easier low voltage-based stabilization.
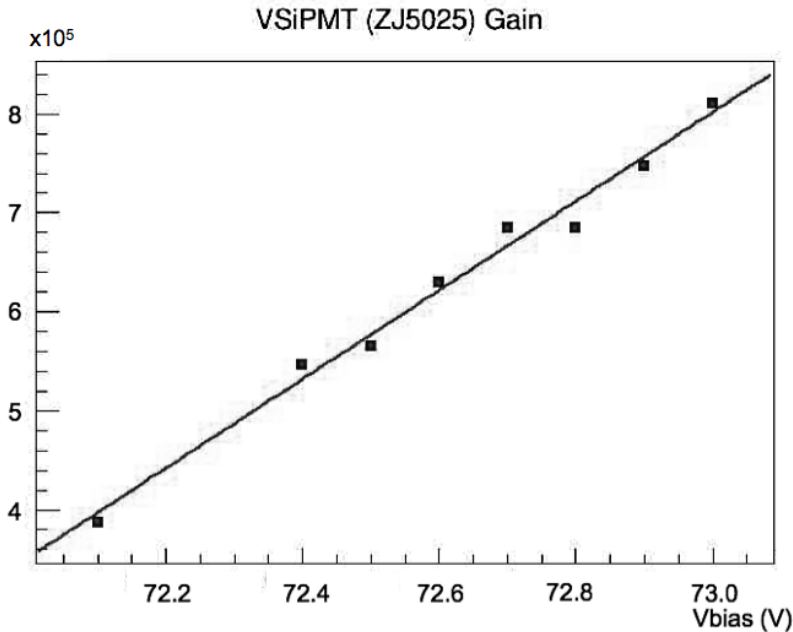
Figure 3.28: Gain workfunction of the ZJ5025 prototype.

3.2.7 Linearity

The linearity of aVSiPMT depends on three factors: photocathode linearity, focusing and G-APD output linearity. For the GaAsP transmission mode photocathode in use, an excellent output linearity is provided if operated at high supply voltages (above few hundreds Volts) and at small currents. The first condition is fairly satisfied by the operating photocathode HV described previously, while the upper limit for the average current is 0.1 μA.

As argumented in Sec. 2.5.1, the linearity of a G-APD is strongly related to the total number of pixels. Until the number of detected photons is much smaller than the number of cells, the output of the G-APD is fairly linear. As the number of incident photons increases, the output linearity starts to degrade until saturating when the number of photons is about equal to the number of cells.

Electrostatic focusing plays a crucial role in the definition of the dynamic range of a VSiPMT. Indeed, the output linearity of the G-APD is maximized if all its pixels are hit by the accelerated photoelectrons. Differently from the cases of a PMT or an HPD, a too strong focusing would be deleterious because a too squeezed photoelectron spot means that not all pixels are involved, thus drastically reducing the linearity (see Fig. 3.29).

In the ideal case, assuming a perfect photocathode linearity and an optimal electrostatic focusing, for the VSiPMTs under test the expected dynamic range is given by the following expression:

$$N_{pe}(N_{pixels}, \lambda, V) = N_{pixels} \times \left[1 - \exp\left(\frac{-N_p h \times PDE(\lambda, V)}{N_{pixels}} \right) \right], \qquad (3.12)$$

where N_{pe} is the number of detected photoelectrons, N_{pixels} is the total number of G-APD pixels, $N_p h$ is the number of incident photons and PDE the overall Photon Detection

90
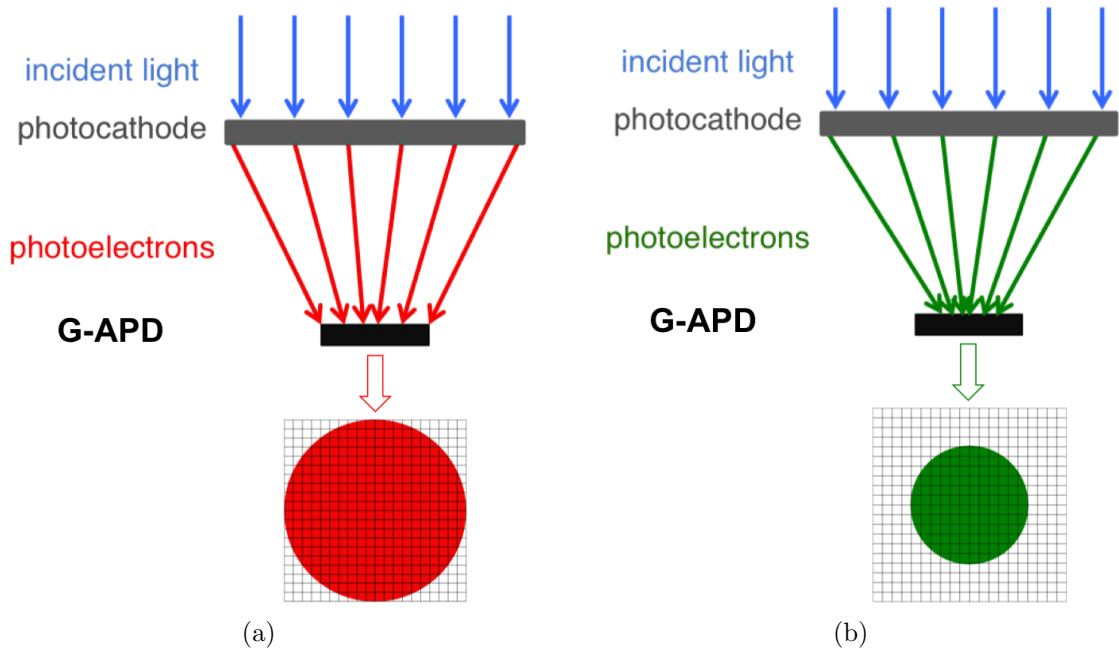
Figure 3.29: VSiPMT electrostatic focusing: ideal case (a) - strong focusing case (b).

Efficiency of the devices.

The linearity of the two VSiPMT prototypes has been measured keeping the photocathode fully illuminated and measuring the number of detected photoelectrons (number of fired G-APD pixels) as a function of the incident power.

The results for the ZJ4991 prototype, shown in Fig. 3.30, indicate clearly that a focusing problem holds. The output signal saturates soon, with a number of photoelectrons not exceeding 20 even under high illumination conditions, suggesting a too small size of the photoelectrons beam. This is a robust hint for a too strong focusing, a crucial feature to take into account in the future phases of optimization.

3.2.8 Noise

The main noise source in a VSiPMT is represented by **dark pulses**. Two contributions can be taken into account: thermal electrons emitted at the photocathode and intrinsic G-APD dark pulses. The latter, as described in Sec. 2.5.1, has a typical rate ranging between few tens and some hundreds of kcps per mm^2 of active surface, depending on the applied overvoltage, thus constituting, by far, the dominant noise source.

The dark count rate of the two prototypes has been measured setting an HV value above the threshold (-4 kV) and counting, for different bias voltages, the number of events with peak amplitude above 0.5, 1.5 and 2.5 photoelectrons thresholds, respectively. Fig. 3.31 shows the measured dark count rates for the ZJ5025 and the ZJ4991 prototypes. In both cases, the results are in excellent agreement with the expected dark count rate of the G-APD alone. The test was repeated in the same experimental conditions but with no high voltage applied to the photocathode. The results were practically unvaried, confirming that the dark counts rate of the VSiPMT depends only on the G-APD.

Another important noise source for the VSiPMT is represented by **afterpulses**. Also in
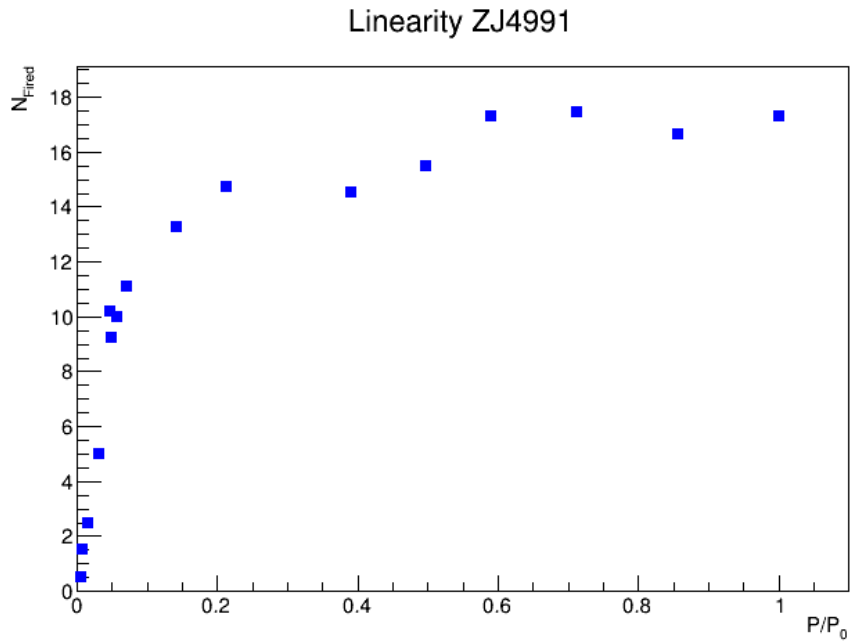
Figure 3.30: Linearity of the ZJ4991 prototype.
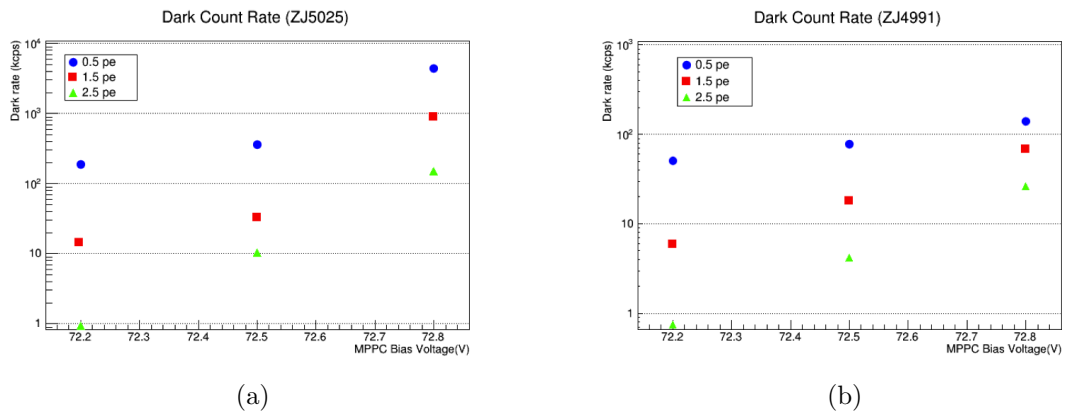
Figure 3.31: Dark count rate of the ZJ5025 (a) and ZJ4991 (b) prototypes at 0.5, 1.5 and 2.5 photo-electrons thresholds.
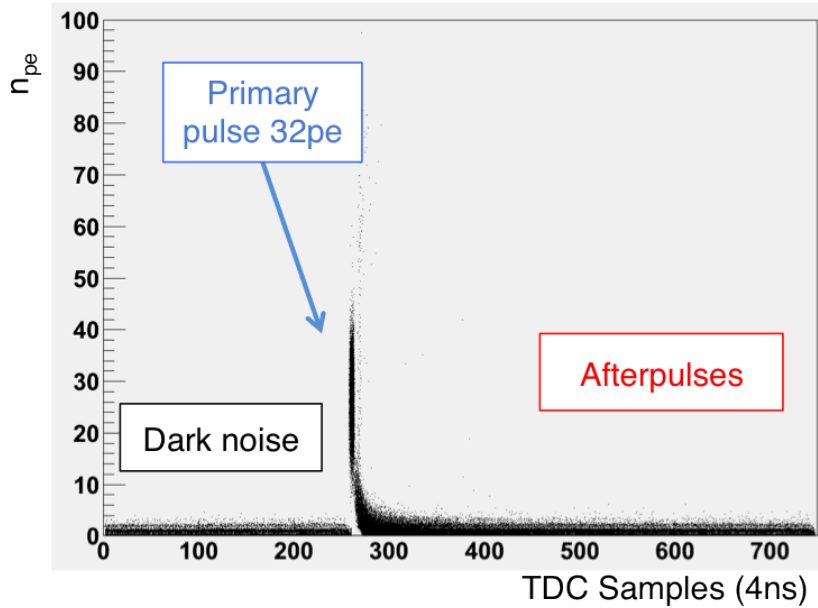
Figure 3.32: Peak arrival times for the ZJ5025 prototype: signal amplitude (expressed in terms of number of photoelectrons) as a function of arrival time (in units of TDC samples).

this case, the combination of two technologies gives rise to a double contribution: vacuum-related afterpulses and G-APD afterpulses. The former are produced by the ionization of residual gases left in the tube after evacuation or desorbed by the materials of the VSiPMT structure. This kind of afterpulses is characterized by a delay depending on the electrostatic focusing field intensity and on the distance between the photocathode and the G-APD. The second class of afterpulses is intrinsically related to the G-APD technology (as described Sec. 2.5.1). In this case, secondary pulses are generated by charges carriers that are temporarily trapped by some impurities inside the crystal lattice and then released again after some delay which can last from few nanoseconds up to several microseconds. Typically, G-APD afterpulses are characterized by small amplitudes (corresponding to up to 3 photoelectrons) and high frequency.

In order to investigate both afterpulse classes and to get an estimate of the corresponding rates, an extensive study has been performed. Keeping the prototypes in high light level conditions (corresponding to 32 photoelectrons detected), 100.000 waveforms have been acquired, searching for each of them all the peaks above 3 Root Mean Square (RMS) of the noise level distribution and reconstructing arrival time, integral and pulse height of all the peaks found. The results are shown in Fig. 3.32. The peaks found before and relatively long after the primary pulse (> 50 ns) occur almost uniformly. However, it is possible to observe a band of high intensity afterpulses (more than 10 photoelectrons) at a fixed 38.4 ns delay with respect to the primary pulse. These features are better displayed in Fig. 3.33.

As it can be observed in Fig. 3.33 (left picture), the peaks detected before the primary pulse are uniformly distributed and characterized, in most cases, by single photoelectron amplitude. Only few two-photoelectrons and three-photoelectrons peaks are found, suggesting a dark noise origin. On the other side, the uniformly distributed peaks detected long after the primary pulse correspond, on average, to a slightly higher number
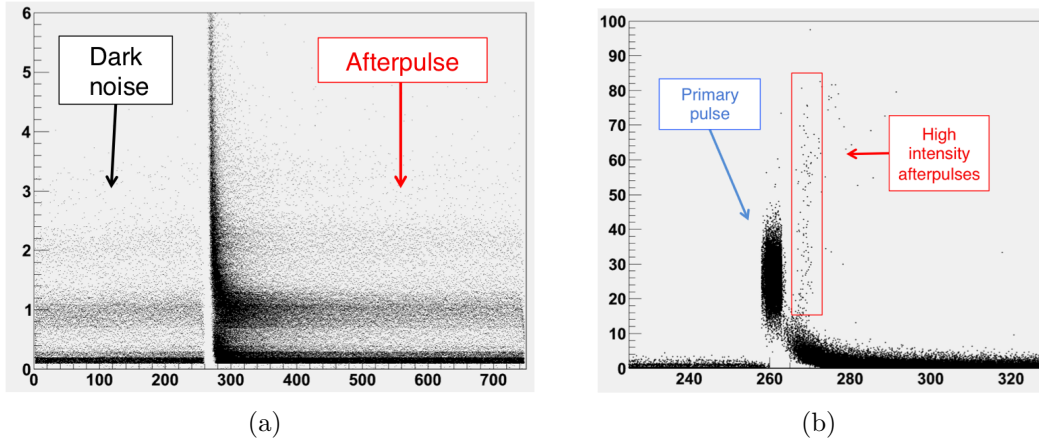
Figure 3.33: ZJ5025 afterpulses: G-APD (a) and residual gases (b) contributions.

of photoelectrons. This increase is given by the contribution of the G-APD-related afterpulses. Indeed, the measured afterpulse rates in this time interval (10.41%, 9.40% and 7.34%, corresponding to 0.5, 1.5 and 2.5 photoelectrons thresholds, respectively) are in fair agreement with the typical afterpulse rates of a standard G-APD.

The high amplitude band shown in Fig. 3.33 (right picture) is populated by peaks ranging from 10 to more than 80 photoelectrons and can be attributed to the contribution of vacuum-related afterpulses. In order to test this hypothesis, several runs have been taken keeping the same experimental conditions and varying only the HV applied to the photocathode. It has been observed that, as the value of the HV increases, the high amplitude band appears with a decreased time delay with respect to the primary pulse and an increased mean intensity, a result perfectly compatible with the expected behavior for afterpulses generated by the ionization of residual gases in the tube. However, the contribution of these afterpulses is really negligible, with a measured rate of $\sim 0.02\%$.

3.2.9 Transit Time Spread

Transit Time Spread (TTS) is a key feature for all photodetectors. As for a standard PMT, also in VSiPMTs the main contribution to TTS is given by the spread in electron path length. However, in this case there is no contribution from the spread in emission velocities of the secondary electrons in the dynode chain. In a VSiPMT the electron multiplication is obtained by means of a breakdown, a faster process with negligible time spread. For these reasons, the TTS for a VSiPMT is expected to be systematically lower with respect to that measured in standard PMTs.

For the two prototypes under test, the TTS has been measured with the experimental setup shown in Fig. 3.34.

The laser output was set at single photoelectron level and the photocathode was fully illuminated keeping the optical fiber distant from the VSiPMT and exploiting the divergence angle of the output light. The transit time has been measured as the time interval between the emission of photons and the acquisition of the corresponding VSiPMT output signal. Therefore, the external trigger signal of the laser source is used as START, while the output from the VSiPMT is fed as the STOP signal via a discriminator.

94
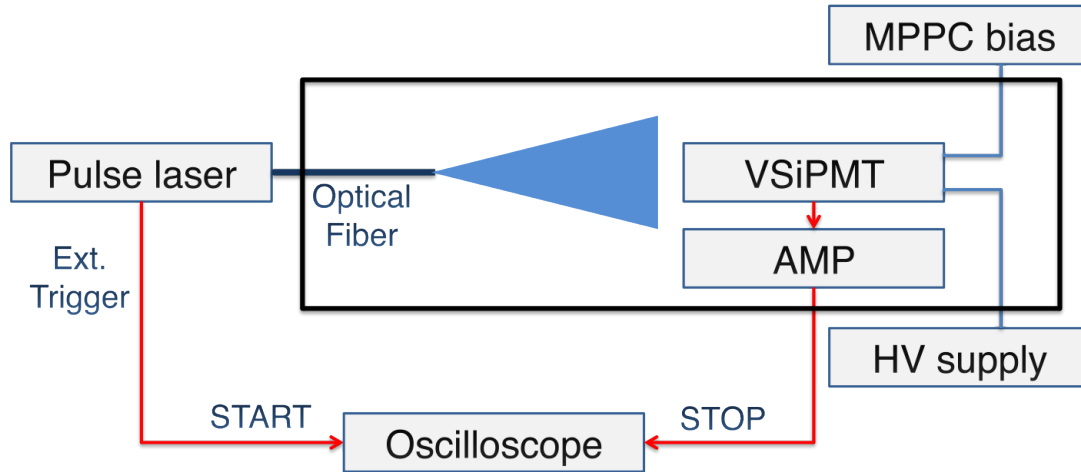
Figure 3.34: Experimental setup for TTS measurement.

As for PMTs, also in a VSiPMT the transit time has statistical fluctuations, mainly due to the differences in the photoelectrons path lengths between the different points of the photocathode where they are generated and the G-APD target. Fig. 3.35 shows the histogram of the measured transit times values: the standard deviation of such distribution corresponds to the TTS, for which the calculated value is less than 0.5 ns.

3.3 Prototype engineering

The balance of the characterization of the first two prototypes of VSiPMT is unbelievably positive. The devices exhibit outstanding properties and performances beyond expectations. Excellent photon counting capability, fast response, low power consumption and great stability are among the most attractive features of the two devices under test, and represent the starting point for a 2.0 phase aimed at the realization of a new optimized version of the prototypes.

The extremely encouraging results of the prototype characterization phase have also drawn the attention on some weak points, paving the way to a prototype engineering phase. Indeed, two main aspects must be taken into account in order to realize the next version of the device: the active surface of the two prototypes is still too small for astroparticle physics applications and linearity is poor. For example, a 3-inch photocathode prototype, with optimized linearity, would represent a perfect solution for many Cherenkov experiments, as well as for Dark Matter search applications.

In order to meet such requirements, an extensive engineering work is required, involving all the constituents of the VSiPMT: photocathode, electrostatic focusing and G-APD.

- **Photocathode**

As described in Sec. 3.2, the two VSiPMT prototypes have a 3 mm diameter circular GaAsP photocathode. Such solution provides excellent performances, with a wide band gap, covering all the visible wavelengths, and values of quantum efficiency up to $\sim 50\%$. However, the technology of GaAsP photocathodes exhibits some crucial drawbacks that drastically limit their applicability to the new version of prototypes under development.
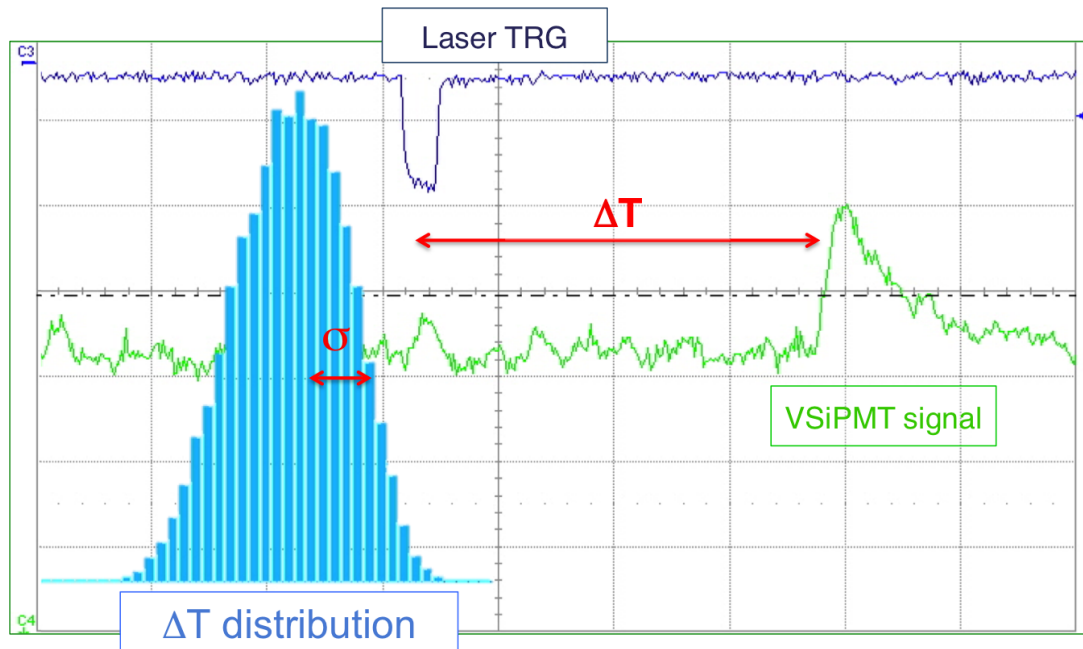
Figure 3.35: TTS measurement: external trigger signal of the laser source and VSiPMT output signal (blue and green waveform, respectively). The cyan histogram is the transit time distribution, whose standard deviation (σ) corresponds to the TTS.

Indeed, a GaAsP photocathode can be made only by epitaxial growth. This implies that such photocathodes can be realized only in flat shape, with high manufacture complexity and costs.

Therefore, a bialkali photocathode seems to represent the most reasonable solution for the next 3-inch VSiPMT prototype version. A bialkali photocathode is made of a compound of two alkali metals with a low work function, providing low noise and high blue and near UV sensitivity. These photocathodes have a typical spectral response ranging between 300 nm and 600 nm, with a quantum efficiency peak of about 25% in the 370-390 nm range. This values are significantly lower with respect to the GaAsP ones and a bialkali photocathode does not cover the visible band as a GaAsP does. However, if compared to the relative Cherenkov spectrum through pure water (see Fig. 3.36) it is possible to observe that for such applications it provides a very suitable solution.

Another fundamental feature of this kind of photocathodes is that they are realized by evaporation. Therefore, differently from GaAsP photocathodes, high surfaces and curve shapes are easily obtainable with much lower costs. Indeed, a GaAsP photocathode is about one order of magnitude more expensive than a bialkali photocathode with the same sensitive surface.

Moreover, recently the QE of bialkali photocathodes has been significantly improved by approximately a factor of two just improving the crystallinity of the antimony film. Two generations of enhanced bialkali photocathodes have been developed: ultra-bialkali (UBA) and super-bialkali (SBA) photocathodes, released in the market in 2007.

As it is possible to observe from their transmission curves (Fig. 3.37), the quantum efficiency of a UBA is competing, in the wavelength range of interest, with GaAsP photocathodes, making it the preferable solution for the next VSiPMT prototype.
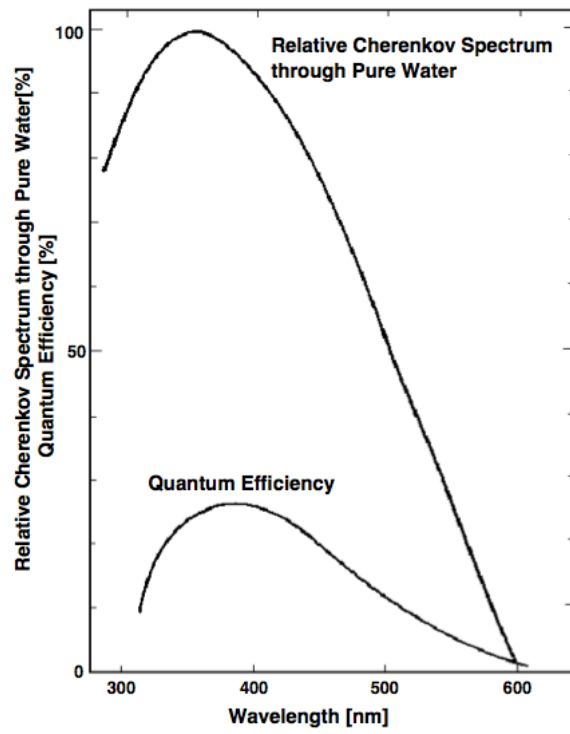
Figure 3.36: Relative Cherenkov Spectrum through pure water and typical QE curve of a bialkali photocathode.
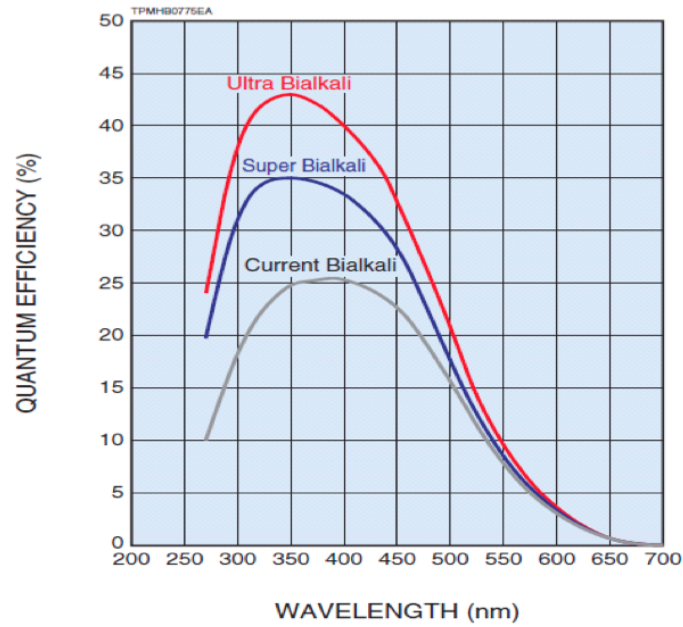
Figure 3.37: Transmission curves for UBA, SBA and bialkali photocathodes.
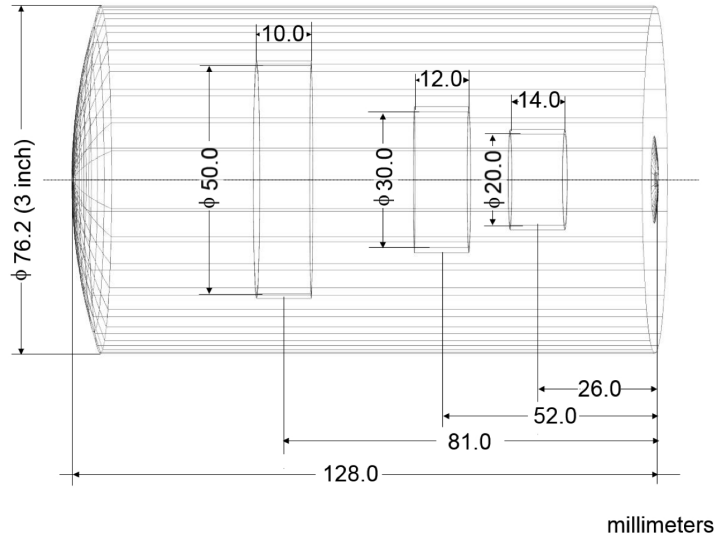
Figure 3.38: Schematic view of the proposed solution for the 3-inch prototype.

- **Electrostatic focusing**

As discussed in the previous section, electrostatic focusing is crucial for VSiPMT performances in terms of PDE and dynamic range. The photoelectron beam size is strongly dependent on the electrostatic focusing field. If the focusing is too weak, the photoelectron spot exceeds the size of the G-APD. Consequently, a fraction of the photoelectrons misses the target and is systematically lost, thus decreasing the overall PDE of the device.

On the other side, a too strong focusing produces a too much squeezed photoelectron beam. In this case, the photoelectron spot intercepts only a fraction of the active surface of the G-APD, with a consequent reduction of the linearity. Indeed, in this case only a small number of pixels can be fired (N_{spot}) and hence the dynamic range is given by Eq. 3.12, with N_{spot} replacing N_{pixels}. This reduction can be drastic, with the additional drawback that all the G-APD pixels not involved in the electron multiplication process are still dark count sources. The budget is deficit: the operative features of the pixels are lost, noise is kept.

The optimal solution, therefore, is represented by an electrostatic focusing system that generates a photoelectron beam having the same size of the G-APD (see Fig. 3.29, left picture). This is not the case of PMTs and HPDs and represents the main problem for VSiPMTs and one of the most crucial goals of the engineering phase.

Obviously, to obtain an optimal focusing becomes more difficult as the size of the photocathode increases. In the following, a study for the realization of the electrostatic focusing system for a 3-inch photocathodes over a 3×3 mm^2 G-APD is presented. The proposed solution consists of a three-stages focusing system. Therefore, the device can be schematized as follows (see Fig. 3.38):

- a 3-inch *photocathode*, curvature radius 128.0 mm;

- *first focusing ring*, performing a time alignment of all possible electrons paths, diameter 50 mm;

98
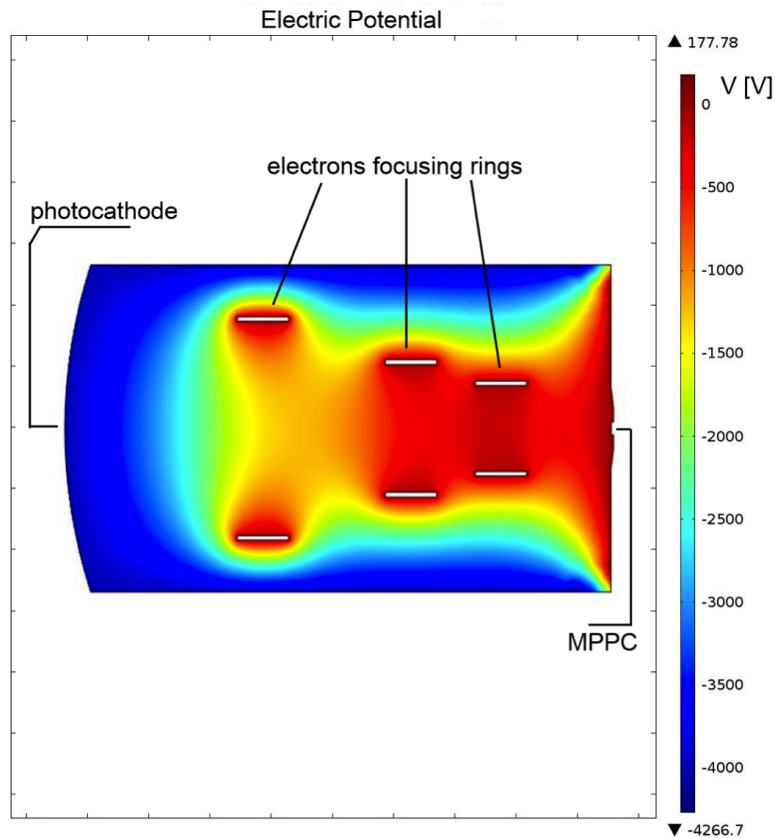
Figure 3.39: COMSOL simulation: electric potential.

- *second* and *third focusing rings*, for fine tuning of the electron beam focusing, diameters 30 mm and 20 mm, respectively;

- 3×3 mm^2 *G-APD* target, electron multiplier stage.

The photocathode is kept at -4 kV, the focusing rings at 100 V, the G-APD is grounded. The electrostatic system has been simulated by means of the COMSOL Multiphysics software. The electric field inside the model has been calculated selecting a stationary solver, using the electrostatic module. Results are shown in Fig. 3.39, while in Fig. 3.40 the equipotential surfaces are reported.

Starting from the stationary solution of the electric field, it has been performed the simulation of electrons trajectories using the COMSOL particle tracing module (see Fig. 3.41). The electron initial energy has been set at 1 eV, with random initial speed directions within an angle of 40° from the normal direction.

The calculated total time of flight for photoelectrons is 5.85 ms while the final energy is 4 keV, above the E_{thr} found in the characterization phase.

The spot of the photoelectrons beam, shown in Fig. 3.42, indicates that photoelectrons are well focused towards the G-APD target: few photoelectrons are lost and few pixels are unused.

- **G-APD**
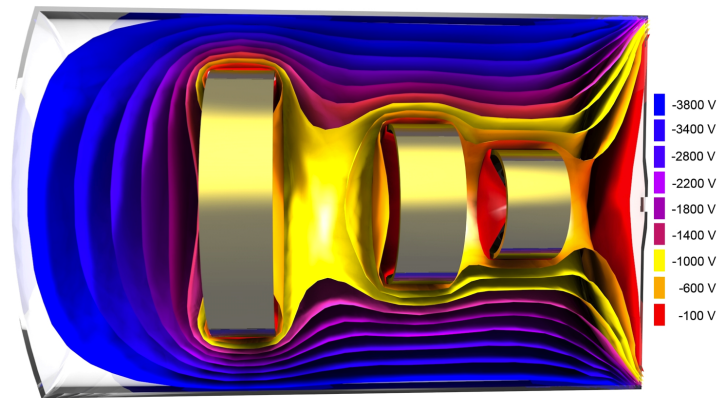
Figure 3.40: COMSOL simulation: equipotential surfaces.
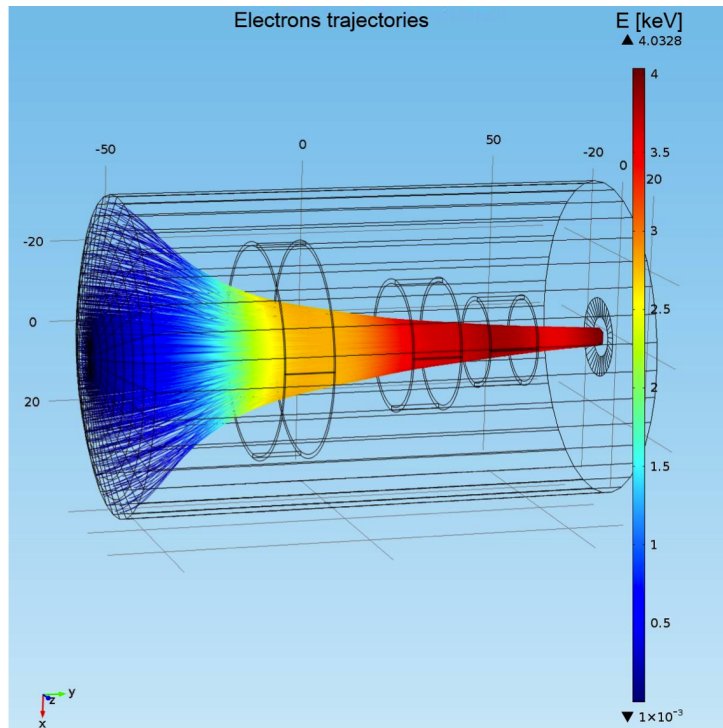
Figure 3.41: COMSOL simulation: electrons trajectories.
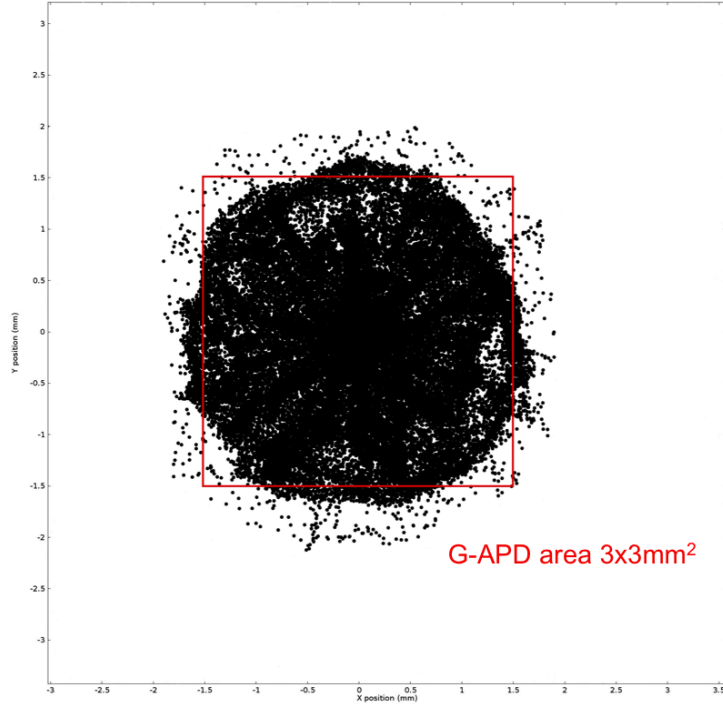
Figure 3.42: COMSOL simulation: photoelectrons beam spot.

The electron multiplier stage represents the most critical part of the VSiPMT. As discussed previously, the G-APD has many attractive features, but also some drawbacks that strongly affect the performances of the whole device.

Much progresses have been made in this sense and still much can be done taking advantage of the whirling evolution of SiPM technology. Indeed, the development of a dedicated G-APD is mandatory and absolutely unavoidable, however it is possible to benefit from some solutions realized specifically for photon detection applications.

An emblematic case has been the development of the p^+nn^+ structure with a thiner SiO_2 surface layer. Originally, it was introduced to enhance the sensitivity of SiPMs to UV photons, but its application to the VSiPMT has generated many fundamental advantages, like lower energy threshold, lower power consumption and higher stability (see Sec. 3.1.2 and Sec. 3.1.2 for details).

Analogously, the VSiPMT will take enormous advantages from the new generation of Hamamatsu MPPCs (Multi Pixel Photon Counters, commercial name for SiPMs), released in January 2014. One of the most outstanding achievements of this new family of detectors is the almost total suppression of **afterpulses**. As described in Sec. 3.2.8, the afterpulse rate for a VSiPMT is practically coincident with that of the G-APD inside, with a measured value of the order of 10%. In the new generation of MPPCs this rate drastically drops to less than 0.3%, a value unimaginably low only few months ago (see Fig. 3.43).

Another crucial factor to optimize is the **dark noise**, that represents the main weak points of the VSiPMT in the comparison with PMTs and HPDs. Again, the new generation of Hamamatsu MPPC exhibits a sensibly lower dark count rate, reduced from some hundreds of kcps to one hundred kcps only per mm^2 of active surface. However, a more
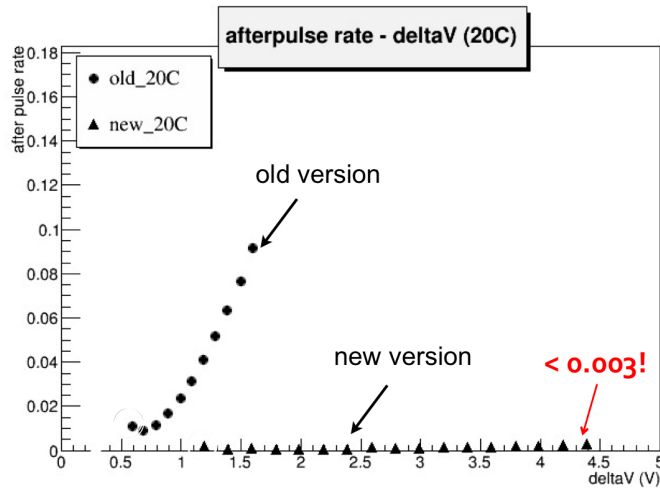
Figure 3.43: New Hamamatsu MPPC generation: afterpulse rate as a function of the applied overvoltage

significant improvement can be achieved taking into account the results of the simulation described above. Indeed, for a round photocathode the spot of the photoelectron beam is expected to have a circular shape (see Fig. 3.42). Therefore, even in the most optimistic case, there will be some dead zones of the active surface of the G-APD that will provide no contribution to signal but only to noise. A smart solution in this case can consist in the realization of an octagonal-shaped G-APD (see Fig. 3.44), in order to adapt the sensitive area of the electron multiplier to the shape and to the size of the photoelectrons spot. As an alternative, it could be possible to use a standard square G-APD with "blind" corners, turning off all the pixels that are not involved in the electron multiplication process.

Also an improvement of G-APD **gain** would provide fundamental benefits to the VSiPMT. As shown in Sec. 3.28, the intrinsic gain of the G-APD ($10^5 - 10^6$, depending on the applied overvoltage) is too small to allow an appropriate data acquisition, thus requiring the realization of some amplifier circuits with multiplication factors ranging between 10 and 20. This means that a further increase of the G-APD internal gain (at least one order of magnitude), would make unnecessary the amplifier circuit, with a consequent significant reduction of power consumption and costs.

Finally, an important feature to take into account is the **linearity**. Assuming an optimized focusing, the linearity of the VSiPMT is directly related to its dynamic range. In general, a high number of micro-cells would be preferable, but a high number of micro-cells means a low fill factor and hence a reduced PDE. Currently, new generations SiPMs are achieving high fill factors even for high number of pixels ($\approx 65\%$ for 10000 cells/mm^2 and $\approx 80\%$ for 100 cells/mm^2, Hamamatsu-Photonics [2014b]), thus extending the possible field of choice. However, a universal solution does not exist. Or better, each application will have an optimal solution, depending on the rightest balance between PDE and dynamic range required.
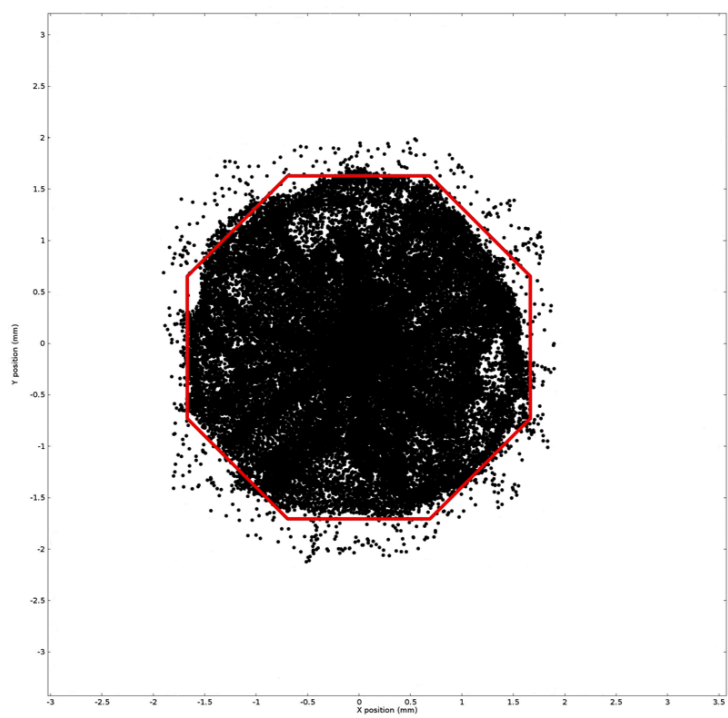
Figure 3.44: Octagon shaped G-APD

Chapter 4

Astroparticle Physics applications: the KM3NeT project

KM3NeT (acronym for Cubic Kilometer Neutrino Telescope) is a European project for the realization of a deep-sea multidisciplinary research infrastructure in the Mediterranean Sea hosting a multi-km^3-scale neutrino telescope and dedicated instruments for long-term and continuous measurements in earth and sea sciences.

The project builds on the extensive experience gained in the Mediterranean pilot projects ANTARES, NEMO and NESTOR, as well as on deep-sea know-how from other fields of science and industry (KM3NeT-Collaboration [2010]), renewing the path traced by former underwater neutrino telescopes like DUMAND and BAIKAL and taking up the challenge with the outstanding achievements of ICECUBE.

The realization of a neutrino telescope in the boreal hemisphere will permit to cover a region of the sky complementary to the field of view of ICECUBE (see Fig. 4.1), including the Galactic Centre and a large part of the Galactic plane. Moreover, KM3NeT will achieve a far better sensitivity with respect to ICECUBE, improving its discovery potential even in the overlapping field of view (see Fig. 4.2). An amazing ambitious task involving more than 200 scientists of 40 research institutes and universities from 10 European countries.

The KM3NeT research facility will be constructed as an installation distributed over several sites, with common detector technology, management, data handling and operation control. The reason of such decision is based on a detailed simulation study indicating that, for muon-neutrino signals from Galactic point sources, the overall sensitivity is not reduced by splitting the detector in independent building blocks, provided these have a minimal size of about 0.5 km^3 (Katz [2014]). Moreover, the choice of a distributed installation will constitute a benefit also for earth and sea science applications, establishing a multitude of observation sites.

The locations of the three installation sites correspond to the ones proposed by the three pilot projects, found after the examination of several candidate sites and an extensive program of measurements into their environmental conditions. The measurements done at these sites were taken over periods that vary in length from a few days to several years of continuous or periodic data and consisted in the study of a large number of oceanographical properties, like deep-sea water optical properties (absorption and diffusion), water environmental properties (temperature, salinity), biological activity, optical
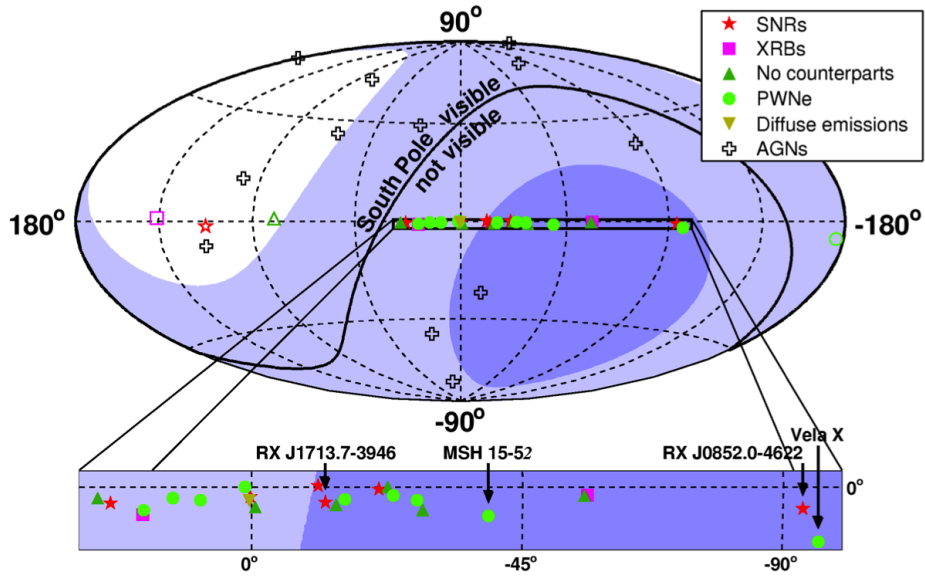
Figure 4.1: Region of sky seen in galactic coordinates for KM3NeT and ICECUBE, assuming 100% efficiency for 2π down.
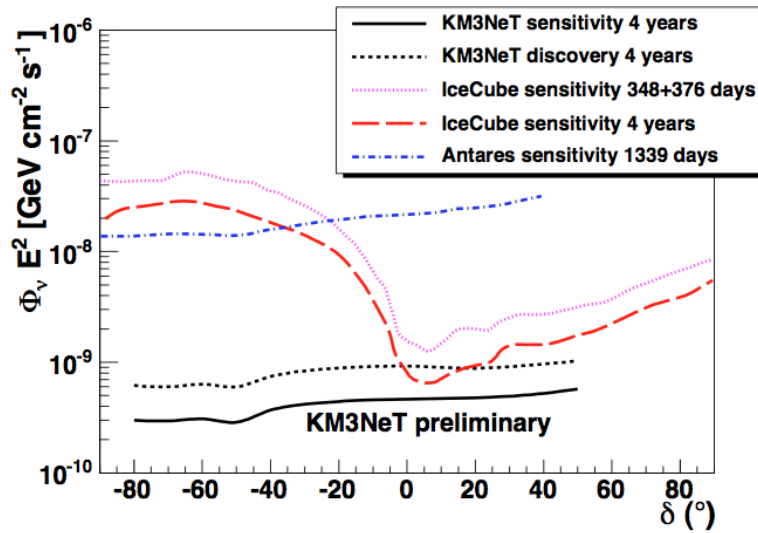
Figure 4.2: KM3NeT 5σ discovery potential and sensitivity for point sources emitting a muon neutrino flux with an E^{-2} spectrum, for 4 years of data taking with the full detector configuration. The flux values are shown as function of the source declination. For comparison, the corresponding sensitivities are also shown for ANTARES and IceCube.
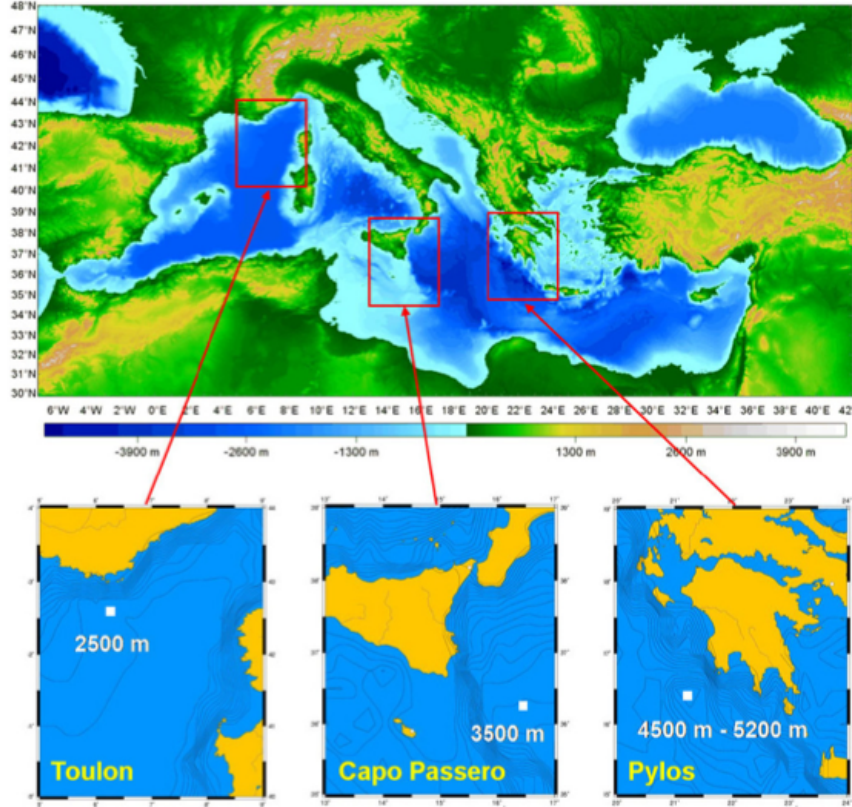
Figure 4.3: The locations of the three installation sites of the KM3NeT neutrino telescope in the Mediterranean Sea.

background, water currents, sedimentation and seabed nature.
The three sites, shown in Fig. 4.3, are:

- **Toulon** (ANTARES), located in the Ligurian Sea at 42° 48' N 06° 10' E, with a seafloor depth of 2475 m. The shore station is placed at La Seyne-sur-Mer, at a distance of 40 km from the site;

- **Capo Passero** (NEMO), located in the West Ionian Sea at 36° 16' N 16° 6' E, with a seafloor depth of 3500 m. The shore station is placed at Portopalo di Capo Passero, at a distance of 100 km from the site;

- **Pylos** (NESTOR), located in the East Ionian Sea in three possible locations at depths of 5200 m, 4500 m and 3750 m. In all cases, the shore station is placed at Methoni, at a distance ranging between 15 and 50 km from the candidate sites.

The italian shore station of Portopalo di Capo Passero is already connected to the installation site by means a 100 km electro-optical cable. Currently, a prototype structure of KM3NeT, built accordingly to the NEMO tower architecture (see KM3NeT-Collaboration [2010] for details) and deployed on March 2013, is in data-taking phase for prototype qualification and site characterization. The next step will consist in the deployment of a group of 8 more towers, currently under construction.
A further qualification step, consisting in the deployment of a reduced-size DU hosting
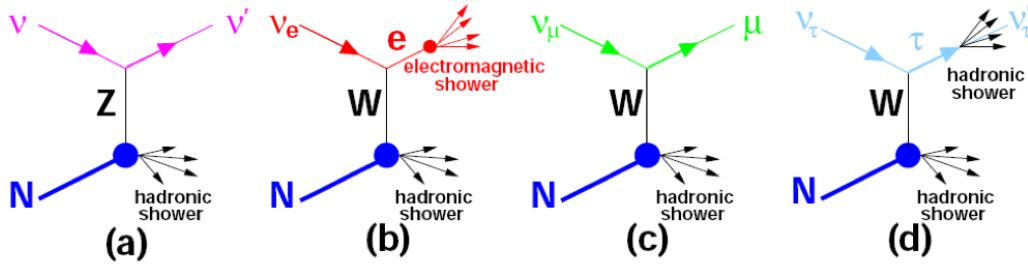
Figure 4.4: Neutrino interactions. (a) Neutral-current reaction: scattered neutrino and hadronic shower; (b) Charged-current reaction of ν_e: electromagnetic and hadronic shower; (c) Charged-current reaction of ν_μ: muon and hadronic shower; (d) Charged-current reaction of ν_τ: double bang event.

three DOMs with the final electronics, has already been planned. The aim will be the test of inter-DOM synchronization, readout, data acquisition and the connection to the deep-sea cable network. In the next future, the deployment of 24 complete strings is foreseen.

This chapter is dedicated to the KM3NeT project: from the physics on which the experiment is based to the project phase, until the most recent developments. In particular, it will be focused on the technological solutions adopted for photon detection. In such context, the unrivalled performances and the outstanding features of the VSiPMT described in the previous chapter could represent an important breakthrough. In the following, the possible application of the VSiPMT to the KM3NeT project will be extensively investigated, taking into account its potential, its current limits and the most interesting perspectives on the base of the forthcoming developments.

4.1   Physics of neutrino telescopes

The high-energy neutrino detection technique on which neutrino telescopes are based consists in the detection of the Cherenkov light emitted by the secondary particles generated in neutrino interactions. The extremely small cross sections of neutrinos require a big target for interactions and a large volume detection medium. In 1960, Markov and Zheleznykh suggested to use the Earth itself as target for neutrino charged-current and neutral-current interactions and a large volume of sea water (or ice) as medium (Markov and Zheleznykh [1961]).

As described in Sec. 1.4, a high-energy neutrino can interact with a nucleon N of a nucleus in the target either through a CC or a NC interaction, with different event classes produced by the different neutrino flavors (see Fig. 4.4) and consequently different signatures of the neutrino event in the detector.

High-energy ν_e and ν_τ can be detected through the detection either of the electromagnetic cascades generated in CC interactions or of the hadronic cascade of NC interactions. However, the detection efficiencies for these types of neutrinos are relatively low, since the produced particles are able to travel short distances and thus can be detected only if they occur inside or at least very near to the instrumented volume of the detector. The main channel for neutrino telescopes is represented by the detection of the relativistic muons generated in ν_μ CC interactions. Indeed, muons are highly penetrating particles, with a
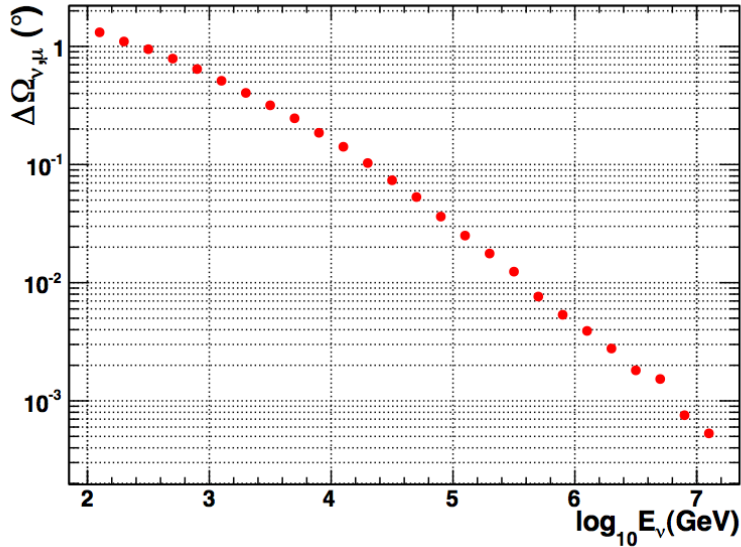
Figure 4.5: Median of the angle between the neutrino and the produced muon directions as a function of neutrino energy.

long range in water and rock in the energy range of interest (several kilometers at $E_\mu \leq 1$ TeV) that makes them detectable even when generated far outside the instrumented detector volume, thus providing a long lever arm for accurate direction reconstruction.

As seen in Sec. 1.4, when a lepton propagates faster than the speed of light through a transparent medium, it emits Cherenkov radiation. The angle between the muon track and the initial direction of the neutrino strongly decreases with the neutrino energy, with values below 0.1° for $E_\nu > 100$ TeV (see Fig. 4.5). Therefore, large volumes of water (or ice) equipped with an array of optical sensors allow the reconstruction of muon tracks with extremely good angular accuracy. Considering the extremely small neutrino interaction cross sections and hence the theoretical expectations of neutrino fluxes, for a neutrino telescope a detection area of at least the order of ~ 1 km^2 is required, with an as much isotropic as possible distribution of optical detectors in order to be sensitive to events coming from different directions. Moreover, an efficient track reconstruction for crossing and internal muons imposes a transversal dimension of at least 1 km and hence a typical volume scale for Cherenkov neutrino telescopes of the order of 1 km^3.

The optical detectors are typically represented by modules where one or more photomultipliers are housed in a high-pressure resistant glass sphere. Such modules measure the arrival time and the intensity of the Cherenkov light, in order to accurately reconstruct the muon energy and the track direction with a precision of up to a few tenths of a degree. The recommended distance between the optical sensors is determined taking into account the attenuation and the scattering of the Cherenkov light in water, described in terms of absorption length λ_{abs} and scattering length λ_s, both functions of the light wavelength λ. Given a beam of initial intensity I_0 and wavelength λ, after traversing an optical path of

length x the intensity reductions due to absorption and scattering are given by:

$$I_{abs} = I_0 \exp\left(-\frac{x}{\lambda_{abs}}\right),$$ (4.1)

$$I_s = I_0 \exp\left(-\frac{x}{\lambda_s}\right).$$ (4.2)

Therefore, λ_{abs} and λ_s represent the path after which the initial intensity of the beam is reduced by a factor of $1/e$ through absorption and scattering, respectively. In particular, the absorption length for pure sea-water turns out to be something about 70 m, thus imposing a constraint on the maximum allowable distance between optical sensors and hence on the detector geometry and layout.

The main background source for a neutrino telescope is represented by the intense flux of atmospheric muons originated by the extensive air showers produced in the interactions of Cosmic Rays with the atmosphere. At the Earth surface their flux is estimated to be about eleven (!!!) orders of magnitude larger than that expected for astrophysical neutrino events. In order to reduce such background contribution, the adopted solution is to deploy the neutrino telescope deep underwater (or under-ice). It can be shown, however, that even at a depth of ~ 3000 m the intensity of the vertical atmospheric muon flux is several orders of magnitude more intense than any neutrino-induced muon flux (KM3NeT-Collaboration [2008]). For this reason, only upward-oriented muon events are considered as good neutrino candidates, thus taking into account only the muons generated by neutrinos passing through the Earth and neglecting down-going muon tracks, being the signal almost completely washed out by the atmospherical background. However, it is possible that multiple coincident atmospheric muons produce a hit pattern resembling that of an up-going muon. This means that detector design and reconstruction algorithms must be optimized in order to minimize the rate of such fake events.

An additional source of background is represented by the large flux of atmospheric high-energy neutrinos generated by the decay of charged pions and kaons produced in the interaction of Cosmic Rays with the atmosphere. This is an unavoidable source of background, however in the case of study of cosmic point sources it is possible to reduce its contribution to a manageable level just reducing the search to a small cone given by the angular resolution of the telescope and to the directional information provided about the source. Conversely, in the case of diffuse neutrino flux search a key for discrimination can be provided by the fact that the energy spectrum of atmospheric neutrinos (spectral index $\alpha \sim 3.7$) is softer than that expected for cosmic neutrinos ($\alpha \sim 2$). This makes possible to search for an excess of cosmic origin neutrinos at higher energies.

In an underwater neutrino telescope, background light can be generated by Cherenkov emission of charged particles originating in the decay of radioactive elements. In particular, sea water contains small amounts of the naturally occurring radioactive potassium isotope (^{40}K) decaying in the following channels:

$$^{40}K \rightarrow^{40} Ca + e^- + \bar{\nu}_e \ \ (B.R.\ 89.3\%)$$ (4.3)
$$^{40}K + e^- \rightarrow^{40} Ar + \nu_e + \gamma \ \ (B.R.\ 10.7\%)$$ (4.4)
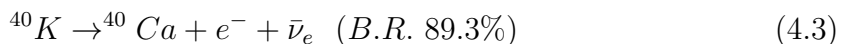
In the former case, the Cherenkov light can be generated by the high-energy electrons produced, while in the latter the γ-rays are energetic enough to produce electrons with
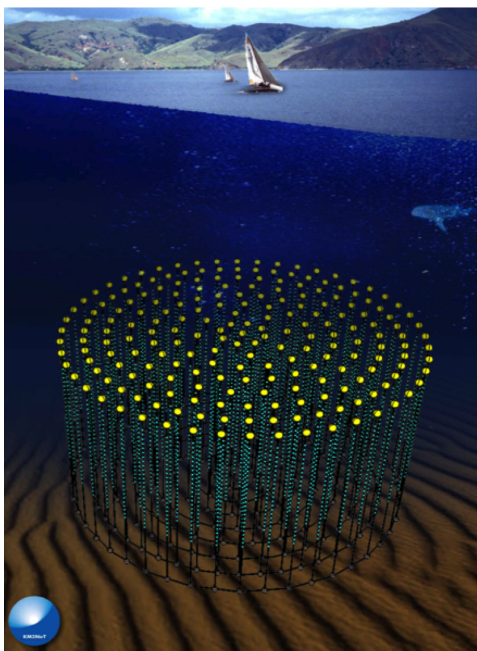
Figure 4.6: Artist's view of KM3NeT.

energies over the threshold for Cherenkov light emission. The result is a steady, isotropic background of photons with rates of the order of 350 Hz per square centimeter that can contaminate the hit pattern of a neutrino induced event (KM3NeT-Collaboration [2008]). The intensity of Cherenkov light from ^{40}K radioactive decays depends crucially on the ^{40}K concentration in the sea water. Since the salinity in the Mediterranean Sea has small geographical variation, this Cherenkov light intensity is largely site independent (KM3NeT-Collaboration [2008]).

Finally, a significative contribution to background is provided by the luminescence induced by biological organisms, called *bioluminescence*, consisting of two main components. The first one is isotropic and continuous, varying on timescales of hours to days, and is usually attributed to bioluminescent bacteria. The other one is represented by localized bursts of light with high rates and durations of the order of few seconds, typically associated to macroscopic organisms passing in proximity to the detector. Both components strongly depend on water quality, season factors and especially on site depth. Extensive campaigns have been carried on in several candidate sites in the Mediterranean sea, showing that the contribution of bioluminescence strongly decreases with depth. In particular, it has been observed (Riccobene [2007]) that for a depth of ~ 3000 m the optical background rate is compatible with that expected from ^{40}K background only, with rare high rate spikes due to bioluminescence.

4.2 The KM3NeT neutrino telescope

KM3NeT is a multi-site three-dimensional array of optical detectors contained in glass spheres that are designed to resist the high hydrostatic pressure of the deep sea environment (artist's view in Fig. 4.6). Such modules, called *Digital Optical Modules*

(DOMs), are suspended in the sea by means of vertical string structures, called *Detection Units* (DUs), supported by two pre-stretched Dyneema ropes, with a dead weight keeping them anchored to the seabed and a buoyancy keeping them in tension. Each DU is equipped with 18 DOMs, starting 100 m above the sea floor and with 36 m distance between adjacent DOMs (see Fig. 4.7, left picture), and hosts the optical detectors readout electronics and all the devices required for calibration, positioning and acoustics measurements as well as sea and earth science instrumentation like video cameras, conductivity-temperature-depth probes, Doppler current profilers, chemical analyzers and seismographs.

Taking into account the values of the absorption and scattering lengths measured during the extensive sea campaigns carried on in order to investigate the properties of the candidate KM3NeT sites, several approaches can be followed about the layout of the DUs (geometry and relative distances). The optimal arrangement of the DUs in space has been determined by means of simulations, in order to achieve the best neutrino detection efficiency, in terms of effective detection volume and angular resolution for the tracks. In particular, at each of the three sites, two building blocks of 115 Detection Units each will be constructed, with an average distance between neighboring DUs of 90 m and the layout shown in Fig. 4.7, right picture.

(a)   (b)
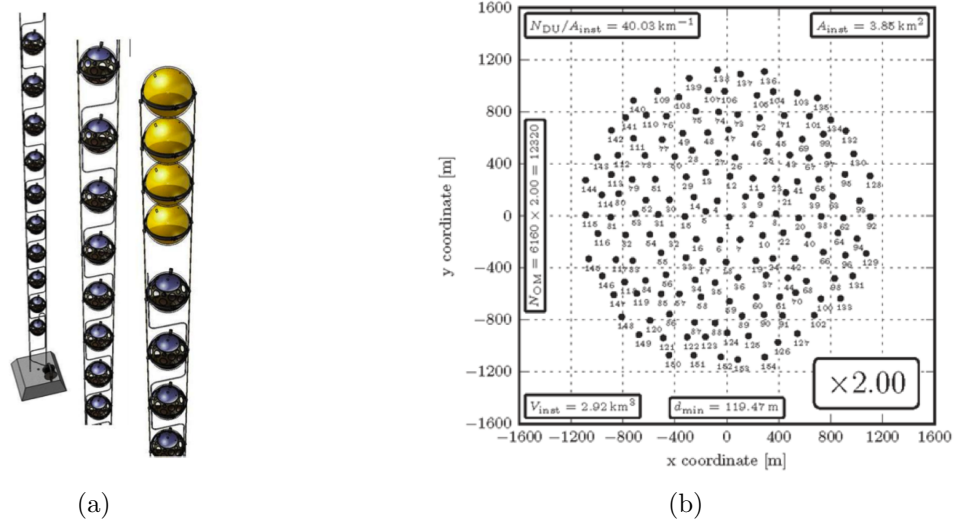
Figure 4.7: The KM3NeT DU: artist's view, split into 3 parts (anchor/middle/top) for display purposes (a) and building block layout (b).

Data and power flows proceed vertically: the power required for the optical detectors and the related readout electronics is fed from shore to a primary Junction Box via a single deep-sea Vertical Electro-Optical Cable (VEOC), consisting of a flexible, oil-filled hose in pressure equilibrium with the sea water. From the primary Junction Box, the power is distributed to several secondary junction boxes and then to the DUs, where it is further distributed to each DOM via a vertical backbone cable. On the other side, data from optical detectors are first digitized inside the DOM and then sent to shore via a fiber optic-based system incorporated in the electro-optical cable network.

The power supplies and the lasers that drive the fiber optic network are housed into a shore station, that hosts also the computing farm required to implement data filtering,
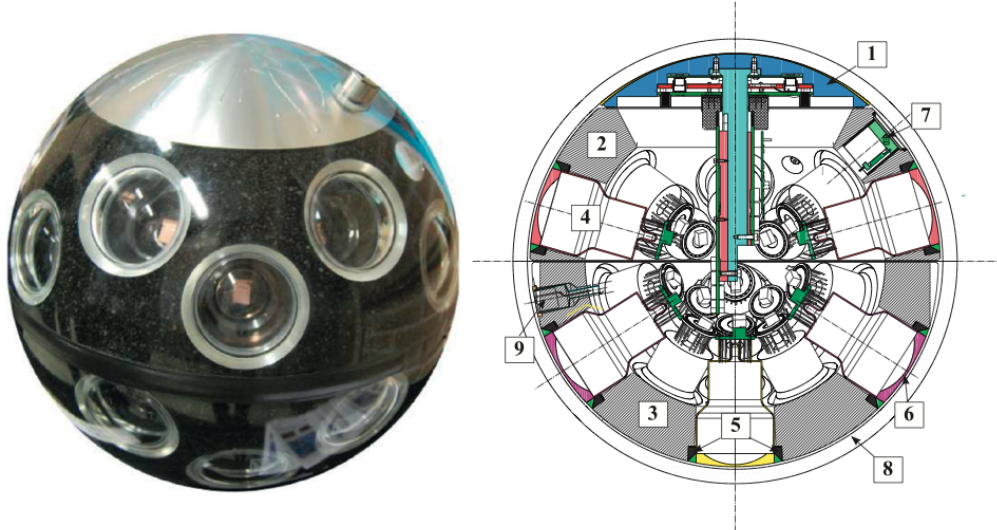
Figure 4.8: *Left*: The Digital Optical Module (DOM) of KM3NeT. *Right*: cross-section of the DOM. Numbers refer to: (1) heat conductor, (2,3) foam cores, (4) PMT with PMT base, (5) expansion cone, (6) optical coupler, (7) nanobeacon, (8) glass sphere, (9) piezo element.

mass storage and distribution.

4.2.1 The Digital Optical Module

The Digital Optical Module represents the active part of a neutrino telescope and therefore the real heart of KM3NeT.

The DOM is composed by a 17-inch, 14mm thick borosilicate glass (Vitrovex) spheric vessel housing 31 PMTs with 3-inch photocathode diameter, the associated frontend and readout electronics, along with power distribution and calibration components, and accessory instrumentation, as temperature and humidity sensors for monitoring purposes (see Fig. 4.8 and Fig. 4.9).

In order to achieve an accurate track reconstruction, a precise PMT positioning (with an accuracy of the order of 10 cm) is mandatory. Therefore, the DOM includes a calibration system composed by a 3-axes compass/tiltmeter to measure the orientation of each module, an acoustic piezo sensor glued to the inner surface of the glass sphere and a compact nanosecond light flasher (nanobeacon), incorporated on an extension board.

The function of such spheres is to provide an adequate mechanical resistance to the extreme compressive stresses of deep-sea environment (the ambient hydrostatic pressure is in the range of 250-400 bar) while keeping a good transparency. The refractive index for borosilicate glass is 1.47, with a transmissivity of more than 95% at a wavelength of $\lambda = 350$ nm. The vessel is composed of two half spheres, with a good water and air tightness of the junction achieved by means of a precisely ground interface and of a special tape applied on the outside of the joint. A dry-mate bulkhead connector penetrates the glass sphere allowing for two power conductors and one fiber to be connected to the high pressure oil filled electro-optical cable.

The choice 31 small surface PMTs (3-inch diameter) adopted in KM3NeT is in countertrend with respect to the standard design of precursor experiments (like IceCube) and
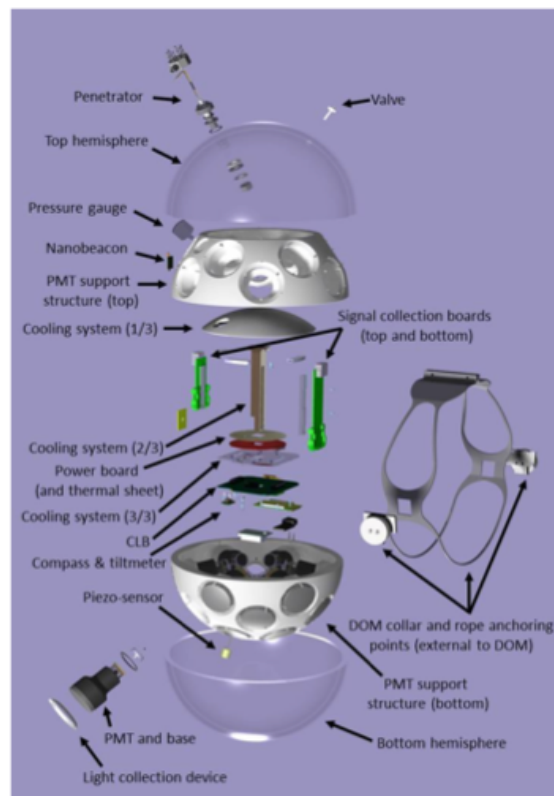
Figure 4.9: DOM components.

even of the three pilot projects, consisting in an optical module housing only one large surface (typically between 8 and 10 inches) PMT. Indeed, such approach offers several strong advantages. First of all, the overall sensitive surface (1260 cm^2) is significantly higher, thus improving the detection efficiency. Small surface PMTs exhibit a weaker sensitivity to Earth's magnetic fields, that in a 8 or 10 inches device can significantly deflect the electrons inside the tube, thus reducing the PMT efficiency and critically affecting its timing characteristics. This means that no shielding is required, with a consequent appealing reduction of integration complexity and costs. Moreover, a segmented detection surface makes possible a definitely better distinction between single-photon from multi-photon events. Indeed, in a DOM a two-photon event can be unambiguously recognized if the two photons hit separate tubes, a condition that occurs in the 85% of cases for photons arriving from the same direction. In addition, the failure risk of a PMT is strongly related to its dimension. In particular, for a small diameter device the integrated anode charge is significantly smaller, thus making them less subject to ageing and decreasing their failure rate to something around 10^{-4} per year.

The PMTs inside the DOM are suspended in a foam support structure (19 in the lower hemisphere and 12 in the upper hemisphere) and are positioned as follows: 30 tubes are arranged in 5 rings with zenith angles of 50°, 65°, 115°, 130° and 147°, respectively, each one hosting 6 PMTs, spaced of 60° in azimuth. The remaining PMT is placed at the bottom of the DOM, with a zenith angle of 180°.

The photomultipliers are glued in the sphere by means of a two-components transparent silicon optical gel (Wacker 612), filling the cavity between the foam support and the glass, and assuring optical contact. In order to reduce the unwanted reflections, a refractive index of ≈ 1.40 is required, close to both the refractive indexes of the glass vessel (1.47) and of the PMT window (1.51-1.54), with an attenuation length greater than 40 cm for wavelengths above 350 nm. In addition, sufficiently elastic foam and gel would provide a precious help in the absorption of the shocks and the vibrations induced by transportation and deployment, contributing to accommodate the shrinkage of the glass vessel under the high hydrostatic pressure.

The DOM contains also a passive cooling system, based on the heat conduction mechanism, aimed at keeping the temperature of the electronic components as low as possible, thus maximizing their lifetime. In order to optimize the transfer of the heat generated by the electronics to the seawater, a metallic structure is required, with an as large as possible contact surface with the inner surface of the glass vessel (through the optical gel). The cooling system is constituted by a mushroom-shaped Aluminium structure, able to maintain temperatures below 30°C for an overall power dissipation inside the glass vessel of up to 20 W.

4.2.2 KM3NeT photon detectors

In KM3NeT, the choice of the optical sensors is definitely crucial. The overall performances of the telescope, in terms of efficiency and track reconstruction resolution, are intrinsically related to the basic performances of the adopted photodetectors. The standard solution is represented by a 3-inch PMT, but in principle also other photodetectors can be eligible. In particular, an attractive alternative to the PMT solution, based on the VSiPMT, will be investigated in details in the following sections.
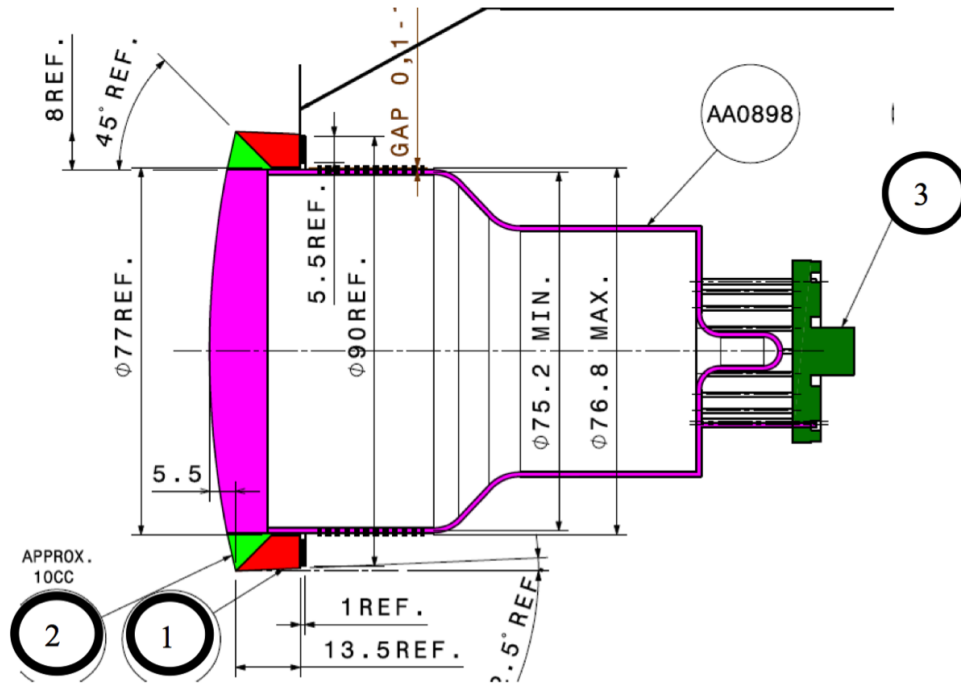
Figure 4.10: Dimensions of the PMT. Numbers refer to: 1. Expansion cone, 2. Optical gel (green), 3. PMT-base.

In order to meet the KM3NeT requirements, the PMTs need to fulfill several requisites, including some geometry constraints. The reduced space available inside the DOM imposes an overall limitation on the length of the device (less than 122 mm) and on the curvature of its photocathode area. In particular, the outer convex surface of the PMT must match as precisely as possible the curvature of the inner surface of the glass sphere. A schematic view of the required dimensions of KM3NeT PMTs is shown in Fig. 4.10.

The performance specifications for the PMTs are summarized as follows (see Fig. 4.11 for a scheme view). First of all, a high **quantum efficiency** is required ($> 32\%$ at 404 nm and $> 20\%$ at 470 nm) in order to enhance the detection capabilities of the optical modules, with an **inhomogenity of cathode response** of less than 10% for track reconstruction optimization. Taking into account the noise level of the electronic circuit for PMT readout, the value of the **gain** of each photomultiplier is fixed at 5×10^6, in order to obtain an easily measurable output signal even in single photoelectron conditions, with a **peak-to-valley ratio** of at least 3 for an acceptable resolution. As thoroughly described in the previous chapters, the gain of the PMTs is strongly dependent on the high voltage applied. This means that, for an imposed value of the gain, each PMT requires its own adjusted **supply voltage**. The requirement for KM3NeT is that this voltage must be below 1400V.

Considering that for a 3-inch PMT the optical background in the sea water is of the order of few tens of kHz, the **dark count rate** of the adopted PMTs (given by the combination of two main effects: thermal electron emission from photocathode and dynode chain and radioactive decay in the glass and in the optical gel, mainly in the form of ^{40}K decay) must be less than 3 kHz.

Cathode	
QE (CsK)	> 32% at 404 nm (> 20% at 470 nm)
Inhomogenity of cathode response	< 10%
Supply voltage	< 1400 V
Gain	5x10^6
External electrostatic coating to the cathode	
Anode characteristics	
Dark count	< 3 kHz at 15 °C > 0.3 pe threshold
Transit time spread	< 2 ns (σ)
Peak to valley ratio	> 3
Environment	
Storage	-10 – 60 °C
Operation	10 – 25 °C

Figure 4.11: Required characteristics for the KM3NeT 3-inch PMT.
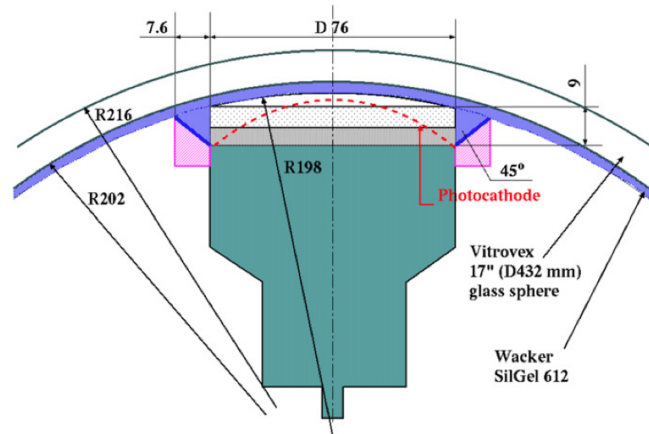
Figure 4.12: The 3-inch PMT inside the glass sphere.

As it will be discussed in the following, the time resolution of the optical sensor has a crucial impact on the reconstructed muon track angular resolution. Therefore, a **Transit Time Spread** as small as possible is preferable, compared with the timescale of the absolute time calibration of the telescope. For the KM3NeT case, a TTS of 2 ns (expressed in terms of the standard deviation σ) has been set as an upper limit.

Finally, some environmental conditions are set, although decisively not severe: the storage temperature must be in the range between $-10°$ and $60°$, while the operating temperatures interval is $10° - 25°$.

The different radius of curvature of the PMT photocathode with respect to that of the glass vessel implies an extra space available on the inner surface of the sphere, surrounding the cathode entrance window (see Fig. 4.12). In order to maximize the effective sensitive surface, each PMT in the DOM is surrounded by an expansion cone, designed to collect the photons that would otherwise miss the photocathode. The expansion cone has an Aluminium structure, with a 45° tilted rflective surface improved by silver evaporation,

keeping a Wacker 612 silicon gel and guiding additional light to the photocathode. The opening angle of 45° is optimized for maximum collection of light coming perpendicular to the PMT entrance window, which is essential for the direction reconstruction. In Fig. 4.13 a scheme view of the light collection mechanism and a drawing of the expansion cone are shown.

(a)

(b)
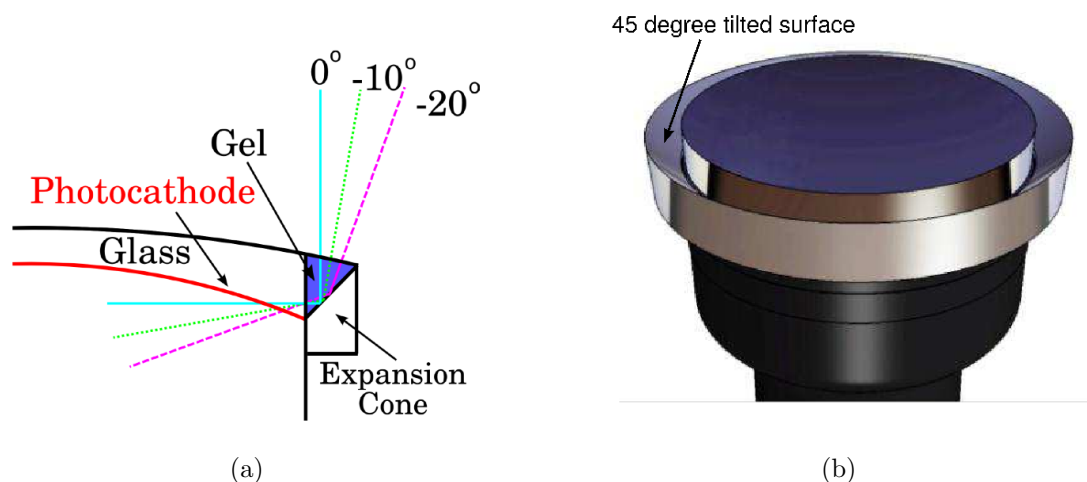
Figure 4.13: The KM3NeT expansion cone: light collection mechanism (a) and drawing (b).

Precise measurements of the expansion cone performances with respect to position and angle of incidence demonstrate a significant increase of the sensitive surface, with high values of the relative collection efficiency (see Fig. 4.14, KM3NeT-collaboration [2013]). The dip in the curve observed at about X=38 mm corresponds to the contact point between the PMT and the expansion cone. In order to quantify the improvement achieved

(a)

(b)
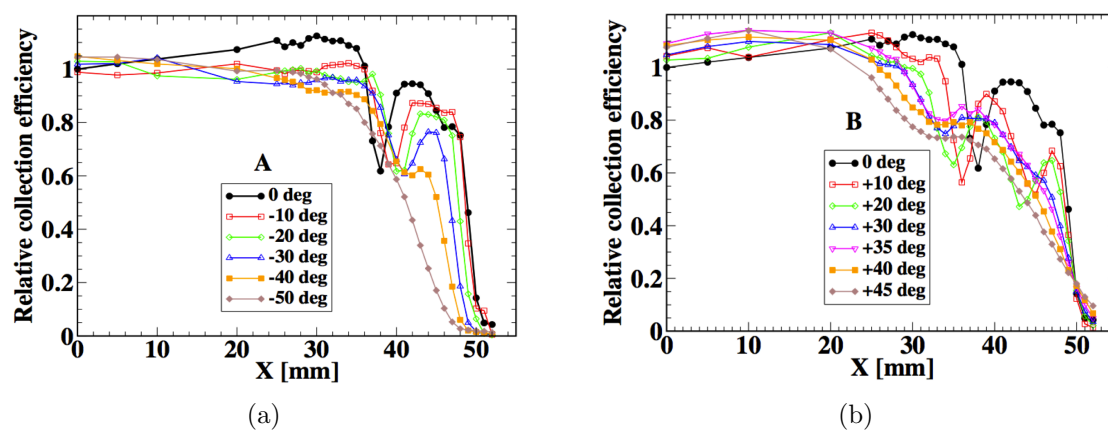
Figure 4.14: Measured relative collection efficiency as a function of the radial position X, normalized to 100% at the center (X=0), for various angles of incidence and for negative (a) and positive (b) angles of incidence.

by means of the expansion cone, the gained collection efficiency (C_g) has been measured.
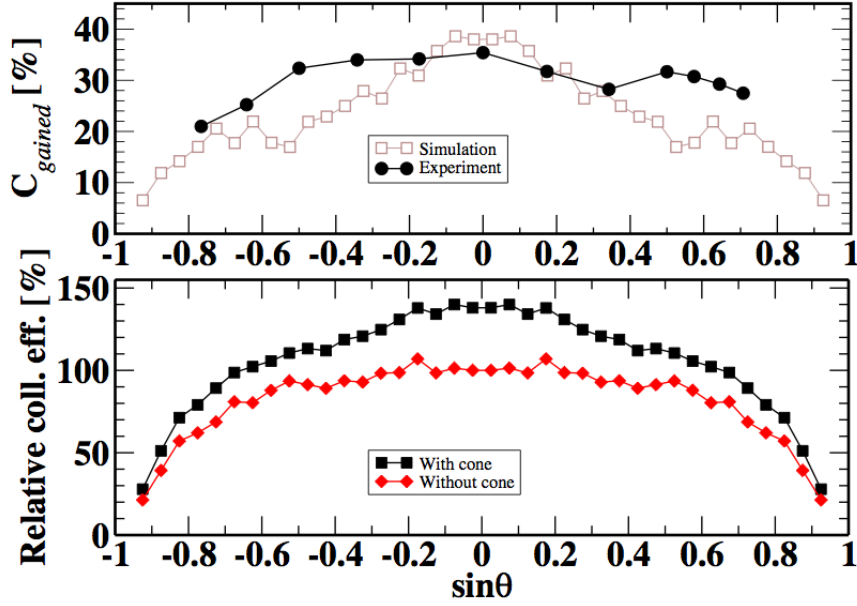
Figure 4.15: *Upper panel*: Gained collection efficiency as a function of $sin\theta$, where θ is the angle of incidence, compared to the results of ray-tracing simulations (KM3NeT-collaboration [2013]). *Lower panel*: Collection efficiency as a function of $sin\theta$ for a single PMT with and without expansion cone (squares and diamonds, respectively).

C_g is defined as:

$$C_g = \frac{C_{P+C} - C_P}{C_P} \times 100, \qquad (4.5)$$

where C_{P+C} and C_P are the collection efficiencies of the PMT+Cone system and of the PMT alone, respectively. For each incidence angle, C_P was measured in the range from 0 to 38 mm, corresponding to the light entering directly in the photocathode, while C_{P+C} was taken in the radial range of the expansion cone, going from 0 to 46 mm. The results show an increase in the collection efficiency of 30% on average for angles of incidence from $-50°$ to $+45°$, with a maximum of 35% for perpendicular incidence (see Fig. 4.15). An extensive campaign has been carried on in order to find out possible PMT candidates. PMTs from several companies have been tested and two candidates (Hamamatsu R12199 and ETEL D792KFL) have been demonstrated to match pretty satisfactorily the KM3NeT requirements in terms of performances and of geometrical specifications. In both cases, the production of the required quantities in due time has been guaranteed by the respective companies.

4.2.3 Frontend and Readout electronics

The output signals from PMTs are processed by means of a dedicated Application Specific Integrated Circuit (ASIC), named SCOTT (Sampler of Comparators Outputs with Time Tagging) and housed in the PMT-base, containing a pre-amplifier, a comparator (Time over Threshold) and an ID circuit for identification.
The digitization of the analog output signals of the PMTs is performed in two steps: in the first one the output charge signal is converted in a voltage signal, while the second
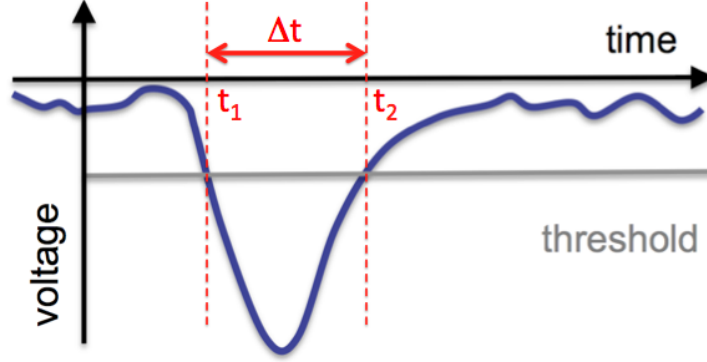
Figure 4.16: Time Over Threshold.

step consists in the time-tagging of the leading and trailing edge of the PMT signal by means of a comparator, resulting in a Time Over Threshold (TOT) signal. In order to achieve a reduced power consumption, only one threshold is set, adjustable using a I2C protocol.

The basic principle is shown in Fig. 4.16. The raw data from the PMTs consist of a continuous stream of hits corresponding to the analogue PMT output pulses that pass a preset threshold. Such data are then digitized and contain information about the timestamp and length of the produced TOT signals. The timestamp corresponds to the leading time t_1 and is used to reconstruct the absolute timing of the pulses, while the Time Over Threshold interval Δt is used for the estimation of the charge of the pulses. Both t_1 and Δt require an accuracy of 1 ns.

The digitized output data is made of 48 bits, where the 8 most significant are used for the PMD ID code, the next 32 represent the timestamp and the last 8 encode the TOT. Such solution provides a significant reduction of data to be sent to shore, but exhibits some intrinsic biases that strongly affect both time and charge reconstruction.

Indeed, the value of t_1 depends critically on the pulse height (slewing bias). Such effect has been calculated parametrizing the slewing as a function of the Δt (tot) values (see Fig. 4.17, left panel) and then comparing it to the simulated time difference between the leading edge of the pulse and the arrival time of the first photon. As a result, the effect of the slewing can be estimated with a resolution of 5.5% (see Fig. 4.17, right panel).

An ever worse situation arises in the case of charge reconstruction. Indeed, the parameterization of the PMT charge in terms of the Δt values is decisively difficult, with many factors (like intrinsic fluctuations of the PMT output signal or deformations introduced by the electronics itself) leading to a poor charge resolution, especially for higher pulses. However, considering the whole DOM, photon counting can be achieved by simply counting the number of (simultaneous) hits on different PMTs. The total charge Q_{DOM} is therefore given by:

$$Q_{DOM} = \sum_{i=1}^{31} Q_i, \qquad (4.6)$$

where Q_i is the charge of the $i - th$ PMT, with an overall resolution that has been estimated to be $\sim 22\%$ (see Fig. 4.18). The DOM charge resolution, although further

(a)　　　　　　　　　　　　　　(b)
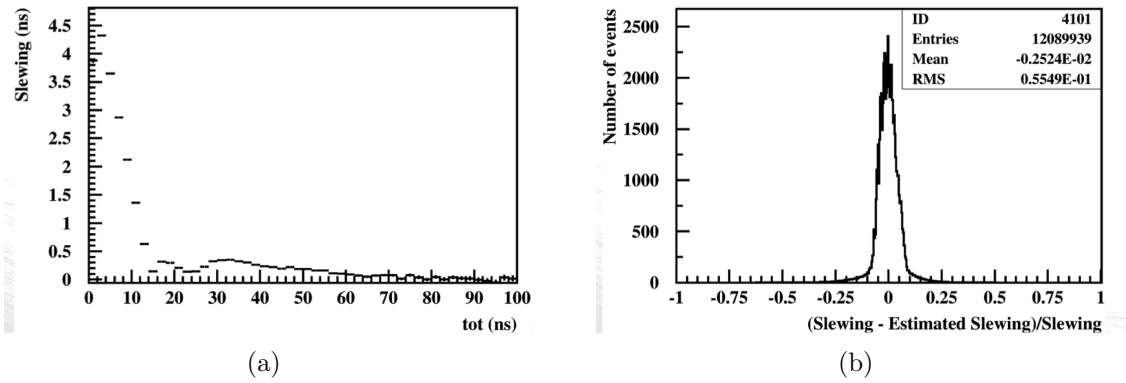
Figure 4.17: Slewing parameterization as a function of the Time Over Threshold (tot) values (a); Slewing resolution (b)
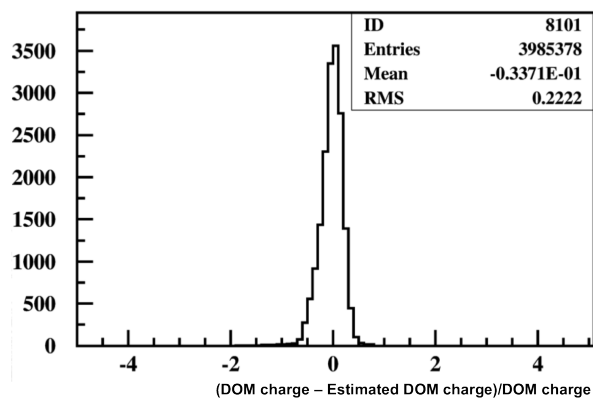
Figure 4.18: DOM charge resolution.
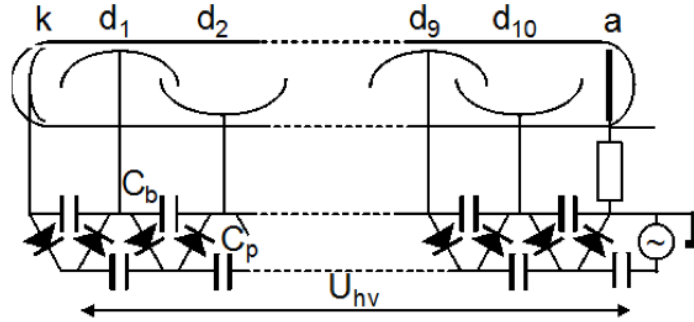
Figure 4.19: Schematic of the Cockcroft-Walter Multiplier.

improvable by taking into account the correlations between neighboring PMTs, represents a decisively weak feature, with important consequences on the reconstructed muon energy resolution. However, other solutions and other approaches are possible, as it will be shown in the next sections.

Another fundamental task of the PMT-base is to provide each PMT with its individual HV supply, in order to have all the PMTs giving the same output signal when hit by a single photon. An I2C protocol is used to program the PMT-base and hence to adjust the HV of the single PMTs in the range between 800 and 1400V.

The DOM is a densely packed glass envelope, therefore power consumption is definitely a crucial feature to take into account. The dissipation of the electronics must be kept within the safety limits determined by the available cooling system, a task demanding severe power budgeting. As shown in the previous chapters, one of the major demands in order to achieve a good stability in the performances of a PMT consists in providing a stable high voltage to all the dynodes. The system adopted in KM3NeT consists in the use of a Cockcroft-Walton multiplier (or Villard cascade, see Fig. 4.19), realized to fulfill the cooling budget requirements and optimized for a significantly lower power consumption with respect to standard passive voltage dividers. The high voltage fed to the PMTs is generated from a 3.3 V DC, with each photomultiplier having its own adjustable base tuned to its own high voltage. The power dissipated by a PMT ranges between 2 and 4.5 mW. The average total power dissipation for HV generation in a DOM is about 31×3.3 mW = 102.3 mW, one order of magnitude lower than the 31×50 mW= 1.55 W achieved by commercially available passive PMT power supplies (Timmer et al. [2010]). Moreover, in order to reduce the ageing effects of PMTs, related to the integrated charge, the high voltage bases are equipped with a preamplifier, allowing for photomultiplier operation at lower gain, with a power consumption of about 25 mW.

The TOT signals of each PMT are collected on a custom electronics board, the so-called "Octopus board" and transferred by a LVDS connection to the DOM Central Logic Board (CLB), see Fig. 4.20.

The Octopus board is responsible for the connection of the electrical power to the PMT bases and the I2C communication control. In particular, it makes possible to switch ON (or OFF) each PMT individually, with an automatic switch OFF procedure in case of overload of a PMT.

The Central Logic Board collects the LVDS data generated by the PMT-base and distributed by the Octopus board. In the CLB, the output signals of the PMTs are converted
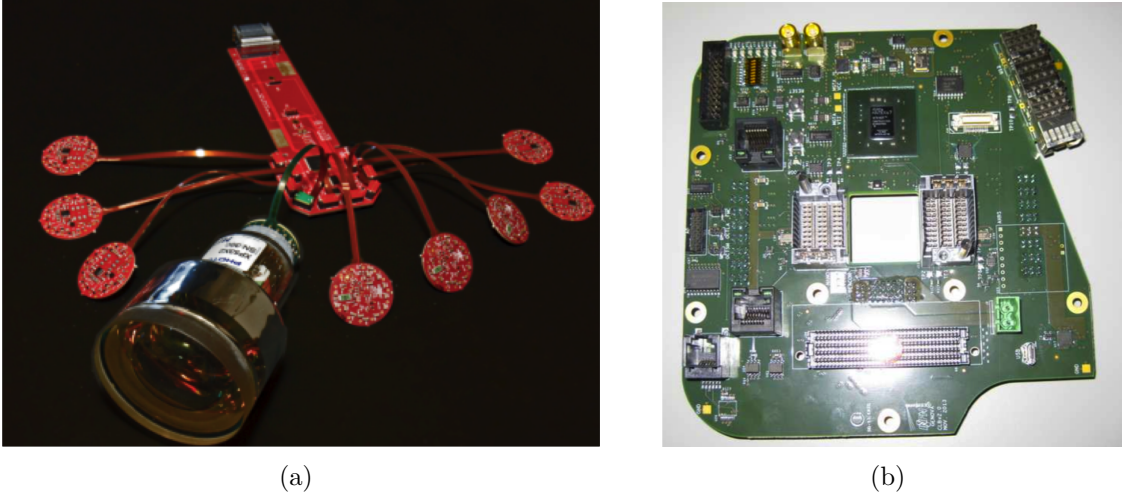
Figure 4.20: The KM3NeT Octopus board (a) and CLB (prototype version) (b)

in time, pulse duration and identification information by means of a 31-channel Time to Digital Converter (TDC) core, timestamped and then sent on-shore. The TDC is embedded in the Xilinx Kintex-7 Field Programmable Gate Array (FPGA) of the CLB, that integrates the so-called "White Rabbit Protocol", a fully deterministic Ethernet-based network that allows to synchronize all the DOMs providing a global time for KM3NeT with 1 ns resolution. The FPGA is used also for the reconfiguration of the firmware of the CLB, with the possibility to store up to four FPGA images for booting.

In addition, the CLB manages the read-out of all the other instruments present in the DOM, as the Compass, the Tiltmeter, the Temperature sensor, the Piezo, the Nanobeacon and the Acoustic Hydrophone.

4.3   The VSiPMT as a possible solution for KM3NeT

The choice of the adopted photodetector is probably the most delicate and challenging issue of all the KM3NeT design phase. The overall performances of the telescope are intrinsically and directly dependent on the performances of the chosen optical sensor. Every single feature is involved: from the achievable detection efficiency to the track reconstruction resolution, from the power consumption to the realization costs and so on. As discussed above, the standard solution, adopted in all the present and past neutrino telescopes, is represented by a PMT. Indeed, PMT technology exhibits many advantages and several interesting features. The most attractive one is undoubtedly represented by its reliability: PMTs are based on a consolidated and well-known technology, a crucial factor to take into account when designing an experiment that must be deployed several kilometers under the sea level.

However, as extensively shown in the previous chapters, such technology is affected by some intrinsic drawbacks that strongly limit its performances, thus seriously compromising the achievable performances of the whole experiment. In this scenario, the unrivalled performances and the outstanding features of the VSiPMT prototypes described in Chapter 3 make this device a serious and charming candidate as an alternative solution to the

standard PMT in KM3NeT.

One of the next steps of the KM3NeT experiment will consist in the deployment, in the italian site of Capo Passero, of 24 fully equipped Detection Units, for a total of 1500 PMTs. Several PMT models from several different companies have been extensively characterized, in order to find out the device that most suitably fulfills the given specifications. As a result, the final choice has been the recently developed **R12199-02** 3-inch PMT by Hamamatsu. In the following, the basic performances of this device (taken from the characterization performed by Kalekin [2013] and Avgitas et al. [2013]) will be accurately compared to those of the VSiPMT prototypes, taking as benchmark all the photodetectors specifications, one by one, officially required by the KM3NeT collaboration and shown in Fig. 4.11.

- **Quantum Efficiency** requirements: > 32% at 404 nm, > 20% at 470 nm.
  For the Hamamatsu R12199-02 PMT a too low QE has been measured at 404 nm ($\approx 27\%$), while the requirement is fulfilled at 470 nm ($\approx 21\%$). The results of the characterization are shown in Fig. 4.21.
  For the VSiPMT, only QE values at 407 nm are available. For both the 50 μm pitch and the 100 μm pitch prototypes the measured Quantum Efficiencies are below the requirements ($\approx 23\%$ and $\approx 30\%$, respectively), but comparable to that measured for the Hamamatsu R12199-02 PMT.
  Considerations: as described in Sec. 3.2.5, the overall QE of the VSiPMT is given by the product of the photocathode Quantum Efficiency and the G-APD EDE, the latter approximable with the fill factor. This means that just improving the fill factor of the G-APD a significant improvement of the total QE is achievable. This is a technological issue, and some interesting progresses have already been done with the new generation of Hamamatsu MPPCs released in January 2014. Indeed, the fill factor for the 50 μm and the 100 μm pitch models is the same, while for the 25 μm pitch an improvement of more than 100% has been achieved (from 30.8% to 65%). This means that significantly higher values can be expected even in the near future. However, on the other side, an important consideration must be done: the two VSiPMT prototypes under test have a GaAsP photocathode, that has a significantly higher QE with respect to the standard bialkali photocathodes but whose complex realization makes it a currently not viable solution for an hypothetical 3-inch device. This means that a possible improvement in the fill factor would be balanced by the loss of QE obtained by using a bialkali protocathode.

- **Gain** and **Supply Voltage** requirements: gain fixed to 5×10^6 for all PMTs, with HV ranging between 1000 V and 1400 V.
  Hamamatsu R12199-02 PMTs are characterized by a very high gain, ranging between 10^6 and 10^7 (Fig. 4.22, left panel) and therefore well matching the gain requirements. However, a quite large HV range is required (Fig. 4.22, right panel), reflecting the typical PMT gain stabilization difficulties described in Sec. 2.1.1.
  As described in Sec. 3.28, for the VSiPMT prototypes a gain ranging between 4×10^5 and 8×10^5 has been measured. These values are about one order of magnitude lower than those measured for the Hamamatsu R12199-02 PMT, but an amplifying stage with a gain of only 10 is enough to meet the KM3NeT specifications. In this

(a)   (b)
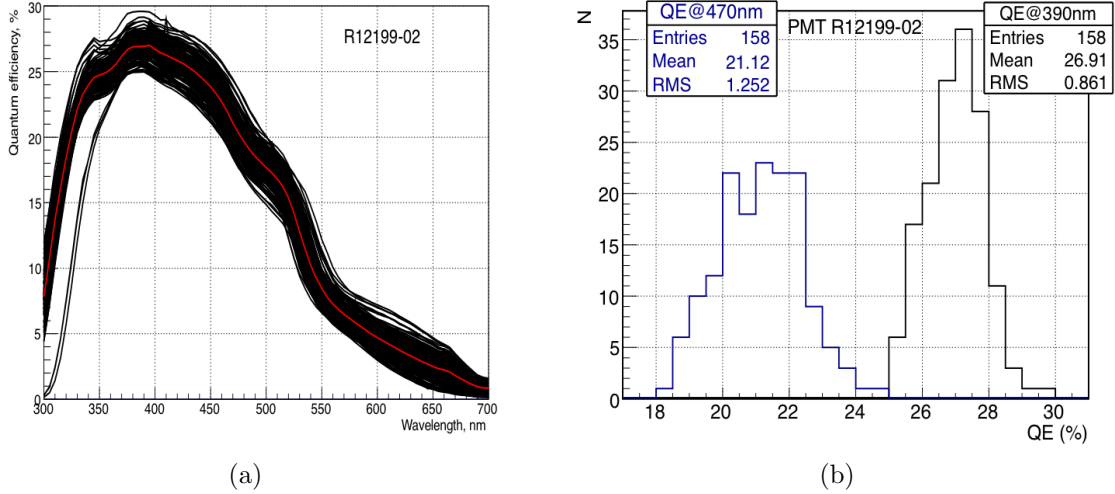
Figure 4.21: Quantum Efficiency for the Hamamatsu R12199-02 PMT: (a) QE vs wavelength (the black curves are the measured QE for each PMT characterized, the red curve is the average) and (b) QE distributions at 390 nm and at 470 nm.

case, however, the required HV must be above the 3.2 kV plateau threshold shown in Sec. 3.2.5.

Considerations: gain stability is a crucial feature and undoubtedly one of the strongest points in favor of the VSiPMT solution. As thoroughly described in the previous chapter, the strong dependence of the PMT gain on the applied supply voltage makes it difficult to achieve a stable gain, and the distribution shown in Fig. 4.22 (right panel) is symptomatic. Indeed, it implies that for 181 nominally identical devices, the HV required to achieve the same gain spans over an interval of about 600 V. Moreover, in general even a small fluctuation in the HV produces a significative variation of the gain. This is not the case of the VSiPMT. It has been shown that the performances of the VSiPMT are independent on the High Voltage applied to the photocathode. In particular, the gain of the VSiPMT depends only on the G-APD bias voltage (see Sec. 3.28), thus implying a much easier low voltage-based gain stabilization.

This is a crucial feature, a fundamental breakthrough bringing extraordinary consequences on the whole telescope performances, in terms of both detector resolution and muon track reconstruction efficiency.

- **Dark count rate** requirements: $< 3\text{kHz}$ at 0.3 pe threshold.
  The dark count rate measured for the Hamamatsu R12199-02 PMT (see Fig. 4.23, left panel) fulfills almost satisfactorily the requirements of KM3NeT: of the 190 PMTs tested, about the 68% has a dark count rate below 1kHz, while in the 86% of cases it is less than 2kHz. Only a very small fraction of PMTs are out of the allowed range.
  For the VSiPMT the measured dark count rate is unacceptably large: between 2 and 3 orders of magnitude higher than the requirements, depending on the pixel size of the G-APD acting as electron multiplier (see for instance Fig. 4.23, right panel).

124
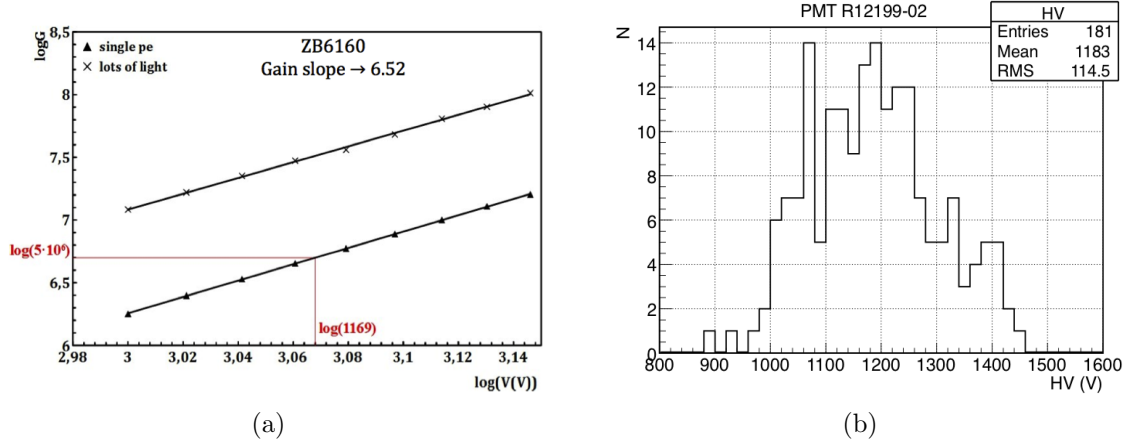
Figure 4.22: Hamamatsu R12199-02 gain: (a) Gain vs HV curve and (b) HV distribution corresponding to the required gain of 5×10^6.

Considerations: dark count rate is undoubtedly the weakest feature of the VSiPMT. The KM3NeT collaboration requires a dark count rate at least one order of magnitude lower than the optical background measured in the sea water (that is of few tens of kHz), while the VSiPMT dark count rate is about one order of magnitude higher. A slight improvement has been achieved with the new generation of hamamatsu MPPCs, but current values are still very far from meeting the collaboration requirements.

Two approaches can be followed in order to overcome this limitation. The first one is to set a higher threshold, cutting off all the events corresponding (for instance) to signals below two photoelectrons and thus achieving a significant reduction of the dark count rate (see Fig. 4.23, right panel). However, given the extremely small number of expected events, the choice of neglecting all the single photoelectron and double photoelectron signals could not be preferable.

The second approach consists in the realization of multiple coincidences between adjacent photodetectors. In principle this seems to be a feasible solution, considering the outstanding performances of the VSiPMT in terms of photon counting and resolution, and would lead to a significative reduction of the dark count rate even to values below the upper limit established by the KM3NeT collaboration.

- **Transit Time Spread** requirements: < 2 ns (σ).
  Both the Hamamatsu R12199-02 PMT (see Fig.4.24) and the VSiPMT prototypes exhibit measured values of the TTS satisfactorily within the KM3NeT requirements (≈ 1.7 ns and < 0.5 ns, respectively).
  Considerations: the TTS measured for the VSiPMT prototypes is more than 3 times lower than that measured for the PMT. However, in this case it must be taken into account that the reduced size of the prototypes play a fundamental role. A small photocathode surface and a small length of the device imply a shorter path for photoelectrons and consequently a lower TTS. For an hypothetical 3-inch VSiPMT prototype it would be reasonable to expect an increase of the TTS value. However, as discussed in Sec. 3.2.9, although the main contribution to the TTS is

125
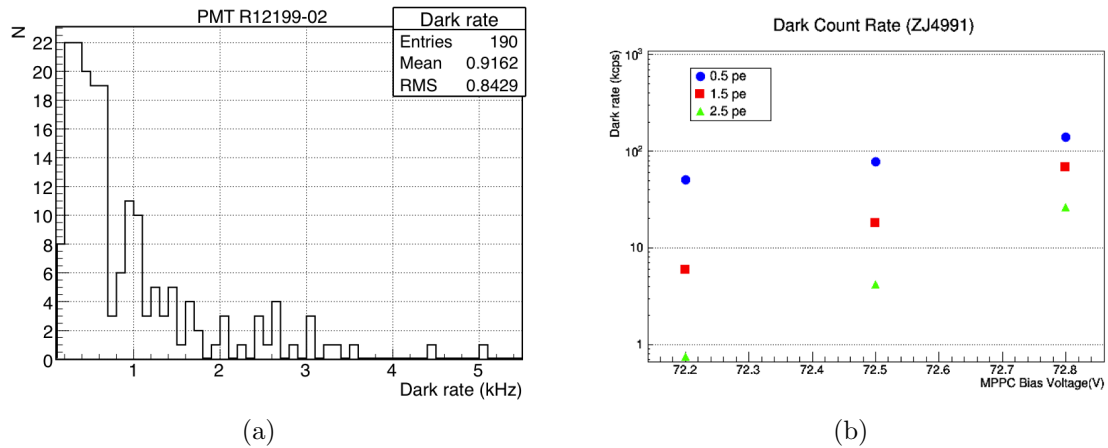
Figure 4.23: Dark count rate: (a) distribution of the measured dark count rate for the Hamamatsu R12199-02 PMT and (b) Dark count rate as a function of the applied G-APD bias voltage for the $100\mu m$ pitch VSiPMT (ZJ4991).

provided by the spread in electron path length, in the case of a VSiPMT there is no contribution from the spread in emission velocities of the secondary electrons in the dynode chain and therefore a systematically lower TTS with respect to a standard PMT is expected.
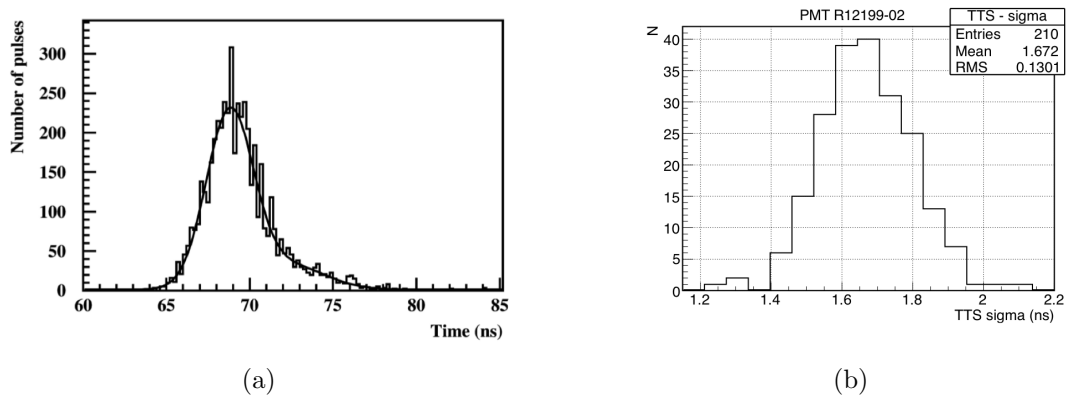
Figure 4.24: Transit time spread for Hamamatsu R12199-02 PMT: (a) Distribution of the arrival time of the pulses, measured at a 0.3 pe threshold level, and (b) TTS distribution.

- **Peak-to-valley ratio** requirements: > 3.
  For the Hamamatsu R12199-02 PMT, values of peak-to valley ratio slightly above 3 have been measured at all the PMT voltage supplies in the range between 1100 and 1400 V (see Fig. 4.25, left panel). On the other side, for the VSiPMT prototypes a value of 65 has been measured, with an exceptional improvement factor of ≈ 20 (see Fig. 4.25, right panel).
  Considerations: in a standard PMT, the photon counting capabilities are seriously affected by the fluctuations of the gain (in particular by the fluctuations of first dynode gain) due to the non-uniformities of the multiplication process. Indeed, by effect of such statistical fluctuations, the anode output pulses exhibit a

126

wide distribution in pulse height, that in many cases can make difficult to separate the SPE signal from electronic noise (see Sec. 2.1.1). This is translated in a low value of the peak-to-valey ratio.

The VSiPMT case is diametrically opposite: the fluctuations due to the dynode chain are no more present and the high value of the peak-to-valley ratio is just a reflection of the excellent photon counting capabilities of the device. This is an extremely attractive feature, as it would imply a significative improvement in the direction and energy reconstruction of the muon tracks.

High Voltage (V)	Peak-to-valley
1100	3,3±0,1
1200	3,5±0,1
1300	3,6±0,2
1400	3.4±0,1

χ^2 / ndf	4.488 / 3
Prob	0.2134
Constant	17.92 ± 3.70
Mean	64.99 ± 3.62
Sigma	20.55 ± 3.22

(a)　　　　　　　　　　　　　　　(b)
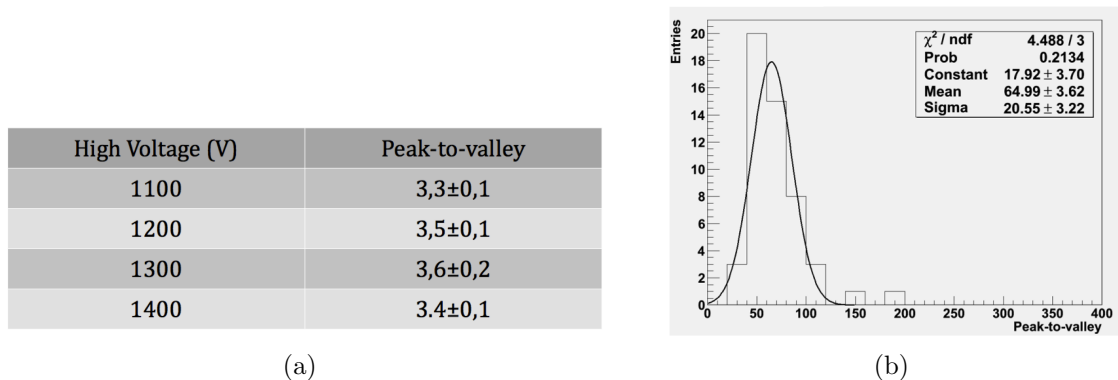
Figure 4.25: Peak-to-valley ratio: (a) values of peak-to-valley ratio measured for the Hamamatsu R12199-02 PMT, as a function of the applied HV and (b) peak-to-valley distribution for the VSiPMT prototypes.

- **Afterpulse rate** requirements: $< 10\%$.
  Both the Hamamatsu R12199-02 PMT and the two VSiPMT prototypes exhibit afterpulse rates fulfilling the requirements of KM3NeT ($\approx 6\%$ and $\approx 10\%$ respectively, see Fig.4.26).
  Considerations: the afterpulse rate of the chosen PMT is about one half of that measured for the VSiPMT prototypes, but the trend is ready to be inverted.
  As described in Sec. 3.2.8, in the case of VSiPMT afterpulses two contributions must be taken into account: G-APD-related afterpulses and vacuum-related afterpulses, with the former representing the dominant afterpulse source. However, as seen in Sec. 3.3, its contribution has been almost totally suppressed with the recently released new family of Hamamatsu MPPC, with a drastic drop of the afterpulse rate to less than 0.3%. On the other side, with the realization of a 3-inch prototype the vacuum-related afterpulses contribution is expected to increase. Indeed, a larger number of gas particles desorbed by materials of the VSiPMT structure is expected as the volume of the device increases. However, considering that in the prototype case the vacuum-related afterpulses contributed for only the 0.02% to the total afterpulse rate, and under the hypothesis that such contribution scales with the detector volume, it is reasonable to expect a small contribution (not exceeding the 0.5%) even for the 3-inch prototype. Therefore, realistically an overall afterpulse rate below 1% will be achieved, one order of magnitude below the requirement of KM3NeT and more than 6 times better than the measured afterpulse rate of the Hamamatsu R12199-02 PMT.
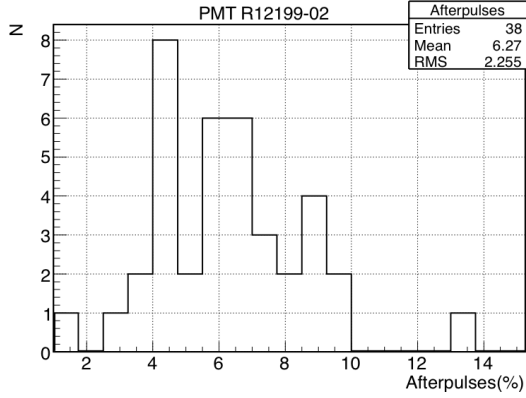
127

Figure 4.26: Afterpulse rate: (a) afterpulse distribution for the Hamamatsu R12199-02 PMT and (b) values of afterpulse rates measured for the two VSiPMT protptypes, for different threshold levels.

- **Power consumption** is a decisive feature in all neutrino telescope experiments. Several contributions can be taken into account, but undoubtedly the most relevant one is represented by the PMT voltage divider.

  In KM3NeT, the typical power consumption of standard passive voltage dividers has been reduced of about one order of magnitude by means of the so-called Cockcroft-Walton multiplier described in Sec. 4.2.3. However, the average total power dissipation for HV generation in the DOM remains high ($\approx$ 100 mW).

  In this scenario, a VSiPMT solution based on the currently available prototypes, along with all the advantages described above, would provide a power consumption comparable to that currently achieved with the standard PMT solution. However, as discussed in Sec. 3.3, the main power consumption source of a VSiPMT is represented by the amplification circuit required to reach a total gain level in line with KM3NeT specifications. The multiplication factors required are relatively small (10 to 20), therefore a further increase of the next generation G-APD internal gain would make unnecessary the amplifier circuit, with a consequent important reduction of both power consumption and costs.

  A lower power budget would provide several fundamental benefits to some of the most puzzling tasks of KM3NeT: the DOM cooling systems requirements would be significantly lightened, and consequently a fascinating strong reduction of detector realization and maintenance costs, as well as of the failure risks, would be achieved. In particular, the latter is a fundamental issue, provided that the hostile abyss environment makes almost impossible every maintenance operation on the deployed string.

  As a possible scenario, the reduced power consumption due to photodetectors could be assigned to front-end and readout electronics resources, in order to achieve a better resolution.

a : Discrimination of the PMT analogue signal

b : Discriminator output signals sampling

c : Digital data in the internal memory
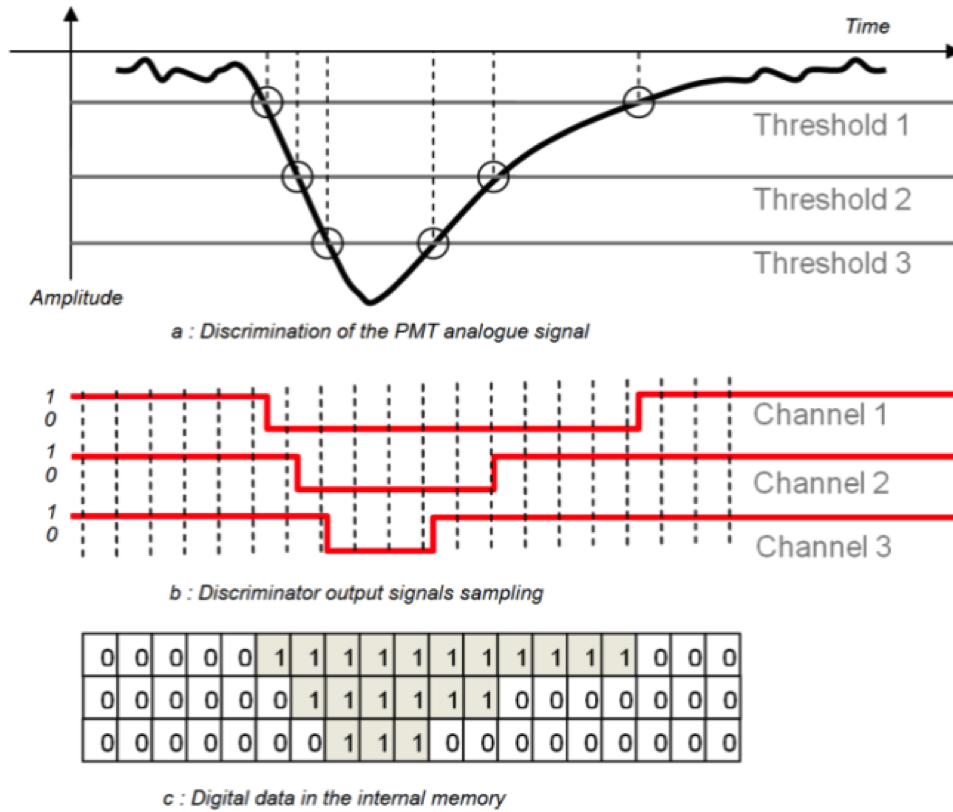
Figure 4.27: The SCOTT approach: signal reconstruction from crossing threshold points.

4.3.1 VSiPMT-optimized front-end electronics for KM3NeT

In the following, a possible solution for KM3NeT front-end electronics optimized for the VSiPMT is presented.

The proposed front-end is inspired to the SCOTT (Sampler of Comparators Outputs with Time Tagging) ASIC designed for the readout of ANTARES-like and NEMO-like Optical Modules (OMs), but is intrinsically different in concept. Only the first step, consisting in the conversion of the output charge signal into a voltage signal, is in common between the two approaches.

In the aforementioned pilot plots, only one large surface PMT was hosted in the OM. Therefore, much more resources could be dedicated to front-end electronics, allowing for a multi-threshold discrimination of the PMT output signal. This approach is aimed at reconstructing the shape of the analog PMT output by means of amplitude and time samplings, and is based on the measurement of the TOT of the different crossed thresholds to determine the corresponding integrated charge (see Fig.4.27).

The process on which the front-end is based can be divided in three steps, shown schematically in Fig. 4.28: in the first one, the PMT analog output signal is sampled in amplitude by comparing it to several variable thresholds, programmable by means of a 10 bit DAC. The digital output of the discriminator is fed as input to a digital sampling memory composed of a Delay-Locked Loop (DLL) to guarantee the accuracy of the sampling time, and two circular banks of memory (2 MB each). A 16 bit coarse time counter converts the discriminator output into a TOT information, with a 1.25 ns time resolution. In the
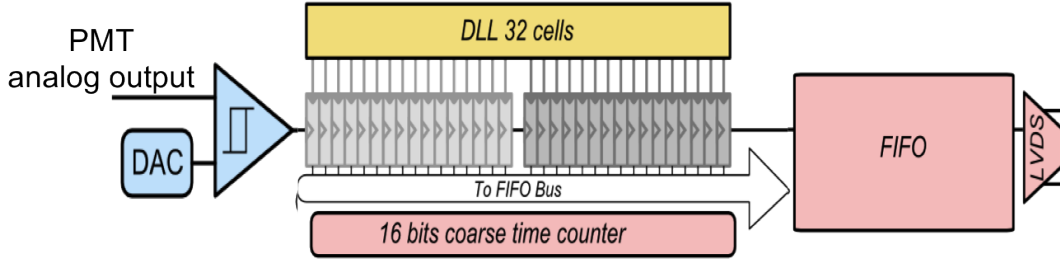
Figure 4.28: The SCOTT data processing architecture.

last step, a FIFO digital memory is used to de-randomize the signal flux and to store the data in a buffer for the subsequent readout steps.

In the case of single PMT OMs, the described multi-threshold TOT approach enables charge reconstruction with an acceptable accuracy (20% up to 60 photoelectrons)[1]. However, as shown in Sec. 4.2.3, the limited power budget available in the KM3NeT DOM led to the realization of an adapted SCOTT-like front-end in which each PMT analog output is connected to one ASIC channel only (see Fig. 4.29). This solution provides
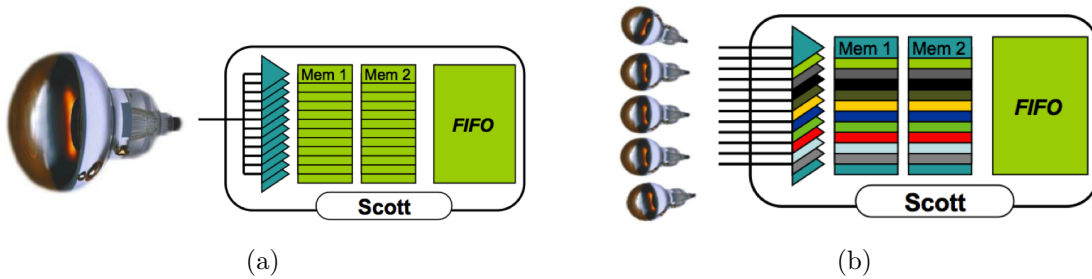
Figure 4.29: SCOTT front-end: (a) standard multi-threshold and (b) KM3NeT single threshold approaches.

a significant reduction of the data that must be sent to shore, but a single threshold only leads to a too poor charge resolution, with serious consequences on the achievable resolution in the reconstruction of muon track direction and energy.

The proposed solution is a VSiPMT-optimized custom version of the multi-threshold SCOTT front-end. In particular, it is thought to exploit in the best way the outstanding photon counting capabilities of the VSiPMT, providing a better achievable resolution and less complicated electronics, with an overall lower power consumption.

As shown in the previous chapters, the output signals of the VSiPMT are characterized by extremely well separated waveforms in correspondence to different numbers of fired pixels (see Fig. 3.21). This fundamental feature makes possible to achieve an unprecedented charge resolution, making completely unnecessary all the TOT measurements and the related electronics. In the proposed front-end, only multiple thresholds discriminators are required to accurately reconstruct the amplitude (and hence the charge) of the PMT

---

[1]An alternative possible approach is that based on the FRED (Fast Rise Exponential Decay) integration, providing a slightly better accuracy (12% up to 25 photoelectrons) but much time and CPU consuming.

output signal, without any time information. Indeed, if the multiple thresholds are set in correspondence to "half photoelectrons" levels (0.5 pe, 1.5 pe, 2.5 pe, 3.5 pe and so on) it is necessary to check only the highest threshold crossed in order to determine the number of G-APD fired pixels and, consequently, of the incident photons. The working principle of the proposed approach is schematically shown in Fig. 4.30.
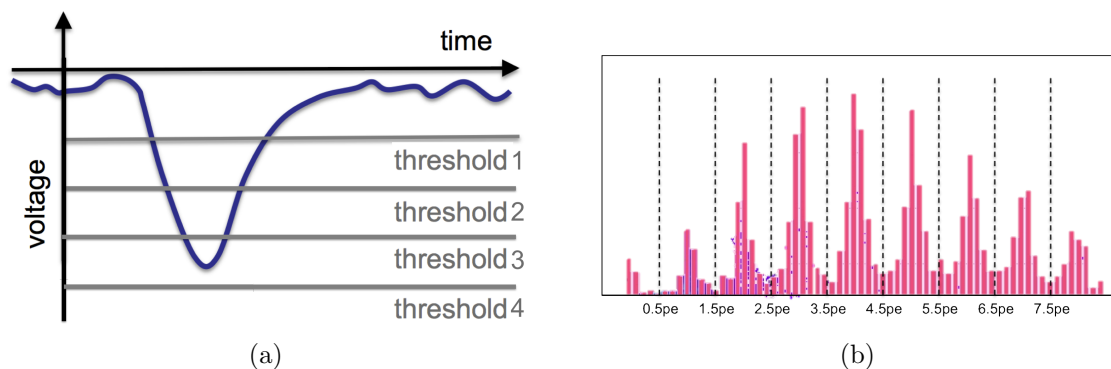
Figure 4.30: SCOTT-like proposed front-end: (a) multi-thresholds crossing by the VSiPMT output waveform and (b) "half-photoelectrons" level thresholds in the output signal amplitude histogram.

As a consequence, in order to implement the proposed front-end, only a set of N programmable threshold discriminators and one N bit register are necessary, along with the FIFO digital memory necessary to de-randomize the signal flux and to store it for the following readout steps. This implies a less complex structure and a lower power consumption, with far better performances!

One of the most attractive advantages of the proposed solution is that the excellent photon counting capabilities of the VSiPMT make it extremely stable and reliable. Indeed, the large separation between the different VSiPMT output waveform families make this method weakly dependent on small variations or fluctuations of the set thresholds values. Nevertheless, as in the case of the standard SCOTT front-end, an accurate preliminary calibration of the devices is mandatory. Indeed, each variation of the bias voltage applied to the G-APD determines a variation of the VSiPMT gain and, consequently, of the output signal amplitudes and so of the multiple thresholds to be set. However, also in this case the low voltage-dependent stabilization of the VSiPMT represents a fundamental advantage, allowing to work in extremely stabler conditions with respect to the standard PMT case and making possible to achieve an otherwise unreachable charge resolution.

Final remarks

This thesis talks about an invention. A three-years-journey started with a sketch on a piece of paper and finished with a prototype realized by the World's greatest photodetector company. And the most amazing pages are still to be written...

A novel photodetector, a revolutionary breakthrough in one of the most crucial fields of experimental physics. A field dominated for more than one century by PMT technology, by the same basic working principle, by the same idea. Obviously, in so much decades this technology has known an impressive evolution. New materials, new layouts, new solutions led to an incredible improvement of PMT performances, most of all in terms of quantum efficiency, gain, bandwidth and power consumption. However, this technology suffers of some intrinsic drawbacks that strongly affect its performances, limiting its current field of application and even seriously compromising its secular leading role in astroparticle physics experiments.

In the last decades, several alternative solutions to PMTs have been proposed. In particular, the strong development of silicon devices have boosted this technology towards a new generation of solid-state photodetectors, based on the inverse pn junction. These devices exhibit important advantages over PMTs, namely higher quantum efficiency, lower operation voltages (and hence strongly reduced power consumption), weak sensitivity to external magnetic fields, robustness and compactness. Depending on the applied inverse polarization bias, three families of photodetectors can be distinguished: PN or PIN photodiodes (with no internal gain), Avalanche PhotoDiodes (APDs, operating in linear region with internal gains of up to a few hundreds) and avalanche photodiodes in Geiger-Mode (G-APDs or SiPMs, operating in Geiger regime with gains ranging between 10^5 and 10^6).

In particular, the SiPM technology, introduced in the first years of the 21st century, has known a whirling evolution, that led current devices to reach an extremely challenging level of performances, in terms of quantum efficiency, gain, photon counting capabilities and time response. However, the small sensitive surface achieved by the current generation of SiPMs (due mainly to thermal dark currents and Silicon wafer costs) sets a strong limit to their possible field of application, making them weak photodetector candidates for most of the next generation astroparticle physics experiments based on scintillation phenomena, Cherenkov or fluorescence radiation.

This is the framework in which the concept of VSiPMT was born. An novel photodetector based on the combination of the excellent photon counting performances of G-APDs and the large sensitive surface of standard PMTs.

In a VSiPMT, the dynode chain of the PMT is replaced by a G-APD, that acts as electron multiplying stage. This solution is expected to bring several important advantages in the comparison with standard PMTs: an significantly improved photon counting capability, faster time response, higher stability and a drastically decreased power consumption (be-

cause no voltage divider is needed). All this while keeping comparable values of gain and quantum efficiency.

In order to prove the feasibility of the VSiPMT, it was mandatory to investigate the performances of the G-APD as an electron multiplier. This required a huge and hard preliminary work, lasted more than two years and consisting in the characterization of a special non-windowed G-APD with a laser source, in the simulation of electron backscattering over the G-APD sensitive surface and in the test of G-APD response to an electron source.

The encouraging results of such preliminary work convinced Hamamatsu Photonics, World leader company in PMT and G-APD manufacture, to realize some prototypes of VSiPMT. The extensive characterization of the two devices provided results going far beyond the most optimistic expectations: the VSiPMT offers very attractive features and high level performances, superior to every other photodetector of the same sensitive surface currently available.

Excellent SPE resolution, easy low-voltage-based stability, very good time performances, acceptable gain and good PDE are among the most outstanding achievements, counterbalanced by some drawbacks like a still high dark noise and lack of linearity. Keeping in mind the extremely encouraging results of the characterization phase, as well as all the weak points found, a 2.0 prototype engineering phase for the realization of a new optimized version of the prototypes has been started. The aim is to realize a next version of the device with a larger active surface and improved linearity. In particular, the feasibility of a 3-inch photocathode prototype, with optimized linearity, is under investigation: a perfect solution for many Cherenkov experiments, as well as for Dark Matter search applications.

One of the most interesting applications is undoubtedly represented by the KM3NeT underwater neutrino telescope. The experiment consists of a deep-sea multi-site three-dimensional array of optical detectors contained in glass spheres, called Digital Optical Modules (DOMs), and suspended in the sea by means of vertical string structures, called Detection Units (DUs). Each DOM houses 31 PMTs with 3-inch photocathode diameter, a solution in countertrend with respect to the standard design of precursor experiments (like IceCube) and even of the three pilot projects (ANTARES, NEMO and NESTOR), consisting in an optical module housing only one large surface (typically between 8 and 10 inches) PMT. Such approach provides several attractive advantages, like higher sensitive surface, weaker sensitivity to Earths magnetic fields, higher resolution and smaller ageing effects.

In this context, the possible application of the VSiPMT to the KM3NeT project has been extensively investigated, taking into account the results of the prototype characterization phase and the most interesting perspectives on the base of the forthcoming developments. The study provided extremely interesting results: the VSiPMT fulfills almost all the official KM3NeT requirements, winning the challenge with the adopted PMTs and thus arising as a very strong candidate for the future phases of the experiment. Among the most important advantages there are a significantly improved photon counting capability, allowing a more accurate muon track reconstruction in terms of both energy and direction, a much easier to stabilize gain, improved timing performances and a considerably lower power consumption, definitely one of the most puzzling tasks for an experiment operating in the hostile deep-sea environment.

Astroparticle physics applications

The performances of the VSiPMT prototypes and the interesting perspectives of the engineering phase make this device a serious candidate for many astroparticle physics applications. A wide range of next generation experiments, aimed at fronting the still many open challenges of astroparticle physics, could benefit from the advantageous features of the VSiPMT.

One of the most interesting application fields is represented by the **Imaging Atmospheric Cherenkov Telescopes** (IACTs). The IACT technique consists in the detection of flashes of Cherenkov light emanating from the extensive air showers that develop when a very high energy γ-ray or Cosmic Ray interacts in the upper part of the Earth's atmosphere (Bouvier et al. [2013]). The goal is to reconstruct their time, direction and energy in order to study the most energetic phenomena in the Universe, like AGNs and GRBs.

In IACTs, the Cherenkov light is collected using a lens or a mirror and imaged onto a camera located at the focal plane. Typically, the camera is composed by an array of photosensors that "pixelizes" the image, recording the arrival time and the number of photons on each pixel element.

The signature of this Cherenkov light emission is given by a ~ 5 ns typical duration and by a blue-ultraviolet peaked spectrum. Therefore, a fast photodetector sensitive in the range between 300 and 600 nm is required to populate the focal plane of the telescope, providing at the same time also a high amplification factor and a large light collection area. All these requirements are well satisfied by the PMTs, that for this reason have been the choice of predilection in this field since the early days.

Indeed, all the current generation IACT arrays, like H.E.S.S., MAGIC and VERITAS, are based on the same scheme, with a matrix of several hundreds of PMTs populating a camera located at the focal plane of a Davies-Cotton (DC) telescope (a multi-faceted single dish mirror). However, the intrinsic drawbacks of PMT technology, especially in terms of the poor SPE resolution caused by the large pulse-to-pulse gain fluctuations shown in Chapter 2, are paving the way to the search of alternative solutions, in order to fulfill the most critical requirements of these kind of experiments: photon counting, high gain, weak temperature dependence, good light efficiency, low noise and small aging effects. In this scenario, SiPMs can represent an attractive solution. However, despite the outstanding performances, a strong limit is represented by their too small sensitive surface. To cover the whole focal plane of the telescope a too large number of SiPMs would be required, implying a too high dark noise level and too large dead areas. One of the adopted solutions consists in the collection of the incident light by means of optical concentrators like Winston cones or pyramidal light guides. In this case, the increase of sensitive surface is paid mainly in terms of angular acceptance, that usually is reduced to values between $20°$ and $25°$. For Davies-Cotton telescopes this is not a decisive weak point, because the light reflected by the multi-faceted mirror is characterized by small angles of incidence (typically within $28°$).

However, this is not the case of the forthcoming *Cherenkov Telescope Array* (CTA), the largest ground-based cosmic γ-ray detector ever built in the World, currently in preparatory phase. The final design consists in the deployment of an array of 60 to 100 telescopes of different sizes and designs over a ≥ 1 km^2 area in the southern hemisphere, comple-

mented by a second smaller array in the northern hemisphere in order to cover the whole celestial sphere over an energy range from a few tens of GeVs to several hundreds of TeVs.

Three kinds of telescopes are foreseen, with different diameter size: Large-Size Telescopes (LST, 24 m), Medium-Size Telescopes (MST, 12 m) and Small-Size Telescopes (SST, 6 m), based on the two-mirror Schwarzschild-Couder (SC) telescope design. This kind of telescope is characterized by a small plate scale which enables the use of compact photosensors and front-end electronics, thus drastically decreasing the overall cost of the camera. However, the dual mirror design of the SC optics focuses the reflected photons onto the focal plane with high incidence angles (up to $\sim 65°$ from normal incidence), making the SiPM+optical concentrator solution definitely not viable.

One of the currently most considered solutions consists in the use of a matrix of SiPMs. However, this would lead to an incredible increase of the number of required photodetectors and, consequently, of the related dark noise. For instance, the MST camera will consist of $\sim$11,000 pixels, each with physical size of 6×6 mm^2. This means that, in order to cover the focal area, 44,000 SiPMs with 3×3 mm^2 size would be required, for an overall dark noise rate of $3 - 6$ Mcps per pixel.

IACTs operate in a naturally noisy environment because of the surrounding Night Sky Background (NSB), therefore sky darkness is one of the most important criteria for site selection. Indeed, the pollution from NSB photons represents the main limiting factor in the determination of the instrument low energy threshold. For this reason, it is fundamental that the level of the photodetectors-related dark noise is significantly below the expected NSB rate, in order to affect as weakly as possible the telescope performances.

For CTA, several sites have been investigated. In particular, from simulations of the SC-MST telescope performance with the NSB spectrum of a site in Namibia, one of the darkest CTA sites being considered, the expected NSB rate for the SiPM solution is of $\sim 20 - 80$ MHz/pixel. Therefore, although smaller than the expected NSB rate, the dark noise of the SiPM pixel cannot be considered a completely negligible component.

In this context, the VSiPMT would represent a very interesting solution. It fulfills all the timing and spectral requirements, providing all the advantages of a pure SiPM solution (especially in terms of photon counting capabilities) with a significantly lower level of dark noise. Indeed, in an ideal layout in which each pixel of the focal plane is made of a 6×6 mm^2 square photocathode VSiPMT, with a 1×1 mm^2 G-APD inside as electron multiplier stage, the overall dark noise would be of the order of 100 kcps. As described in Chapter 3, the dark noise of a SiPM scales linearly with the active surface, therefore in this case a reduction factor of 36 must be expected.

In the last few decades noble liquid detectors for the search of **Dark Matter** (DM) in the form of WIMPs have been extremely successful in improving their sensitivities. In particular, the next generation of multi-ton scale experiments will have the unique opportunity to cover the entire range of predictions for a WIMP particle of O(1 TeV) mass, reaching the paramount sensitivity of 10^{-48} cm^2 in the WIMP interaction cross-section for elastic scattering off a nucleon.

The current generation of DM detectors based on noble liquids is characterized by an effective target mass ranging from 100 kg to the ton-scale (e.g. LUX, Xenon-1T, DarkSide-G2). All these experiments are based on the measurement of scintillation light from liquid argon (128 nm shifted to 420 nm) and liquid xenon (170 nm), performed by means

of 3-inch PMTs. However, the forthcoming next generation experiments (like LZ and DARWIN) will require several improvements in photodetectors performances, especially in terms of single photon counting capabilities, as well as in quantum efficiency, time resolution, gain, power consumption and radioactivity. In particular, the latter represents one of the major concerns, since in current experiments the neutron background rate is dominated by the residual activity of the PMTs.

An impressive amount of R&D has been committed to the development of specialized photocathodes. However, the degraded performances of low temperature PMTs are leading to the search of alternative device.

In this scenario, a customized version of the 3-inch VSiPMT prototype under study could represent a definitely charming solution. Indeed, it would provide the required large sensitive surface and excellent photon counting, while the absence of the dynode chain is expected to produce a significant reduction of the level of radioactivity. Moreover, operations at cryogenic temperatures is expected to suppress the dark noise of the device to a negligible level, thus completely overcoming one of the main current limits of the VSiPMT.

Obviously, several key developments are required to meet the desired targets, spanning from the mechanical structure (made from ultra-clean radioactivity free synthetic fused silica) to the realization of a low temperature high efficiency photocathode, but premises are extremely encouraging.

Hyper-Kamiokande (Hyper-K) represents the next generation of underground water Cherenkov detectors. The project has been designed for the upgraded J-PARC beam, plus a megaton-scale detector, and will serve as a far detector of long baseline neutrino oscillations for the exploration of the CP violation. It will make possible to observe, with a sensitivity going far beyond that achieved by the current generation of water Cherenkov detectors, proton decays, atmospheric neutrinos and low-energy (less than ~ 50 MeV) astrophysical neutrinos, including solar neutrinos, core-collapse supernova neutrinos and potentially dark matter annihilation neutrinos (Kearns et al. [2013]).

The Hyper-K design consists of two cylindrical tanks lying side-by-side, with a total (fiducial) mass of 0.99 (0.56) million metric tons, viewed by $99,000$ 20-inch PMTs, corresponding to a PMT density of 20% photocathode coverage (Abe et al. [2011]). However, there are several efforts currently ongoing to search some alternative photodetectors in order to fulfill as well as possible all the experimental requirements.

For example, a wide dynamic range and a good linearity are among the most important specifications for the adopted photodetector, in order to detect both the several hundred photons expected for high energy particles (e.g. the particles generated by an inelastic atmospheric neutrino interaction) and the extremely low light levels expected for low energy particles, like recoil electrons from solar neutrino elastic scattering interaction. In particular, in the latter case a good resolution at the level of a single photon is mandatory, in order to achieve an acceptable particle energy resolution.

On the other side, the reconstruction of the interaction vertex is performed using the arrival time of photons. Therefore, a good timing resolution of the photosensors, along with a small jitter of the transit time (less than 3 ns), is crucial.

One of the candidate solutions is represented by a 20-inch HPD (currently not commercially available and under development), made attractive by its single photon sensitivity and high timing resolution. Obviously, a hypothetical 20-inch VSiPMT would repre-

sent an even more optimal solution for the Hyper-K experiment. Indeed, apart all the known advantages with respect to the standard PMT extensively shown in this work, the VSiPMT wins the challenge also with the HPD solution, by virtue of its much better photon counting capabilities, much easier-to-stabilize gain and lower power consumption.

Beyond astroparticle physics

The outstanding performances and the features of the VSiPMT make its potential field of application go far beyond astroparticle physics.

One of the most interesting applications is represented by the readout of crystal and scintillating calorimeters. Imaging hadronic calorimeters with scintillator readout use small scintillator tiles individually read-out by SiPMs, in order to achieve the necessary granularity needed for the reconstruction algorithms of future collider detectors (Simon [2011]). In its basic scheme, a wavelength shifting fiber (WLS) is embedded in each scintillator cell, in order to collect the scintillation light (typically emitted in the blue spectral range) and guide it to the SiPM with a wavelength corresponding to its maximum sensitivity (mainly in the green, for old generation devices).

Recently, a new generation of SiPMs with enhanced blue sensitivity has been commercially released, allowing for the direct readout of plastic scintillators without the use of a WLS fiber. This solution leads to a significantly simplified mechanics, due to relaxed mechanical constraints for the optical coupling of the SiPM with the fiber end. Moreover, the elimination of the WLS has the advantage of a faster response since the additional time constant contribution due to the fiber re-emission is no more present.

However, in this case specific modifications of the tile geometry are required in order to achieve an optimal coupling with the photon sensor and to ensure a high degree of uniformity over the full active area. In these conditions, the use of a VSiPMT instead of the SiPM would provide the same photon counting performances with the enormous benefits of a large sensitive surface and an optimal spectral response.

Matching the large sensitive surface of a standard PMT with the excellent photon counting performances of a SiPM, the VSiPMT represents an unprecedented breakthrough in the field of photon detection. In principle, the VSiPMT can be considered a valid solution in almost all the applications in which PMTs are adopted and in many applications in which the performances of a SiPM are required along with a larger sensitive surface.

Many possibilities have been discussed and investigated, but the possible applications are potentially limitless, going from nuclear and particle physics to medical equipment (i.e. PET), from physical check-ups and diagnosis to in-vitro inspections (Radioimmunoassay, Enzyme immunoassay as well as luminescent, fluorescent, Chemiluminescent Immunoassay), biomedicine, industrial applications and environmental measurement equipments.

Bibliography

R. Abbasi et al. Calibration and Characterization of the IceCube Photomultiplier Tube. *Nucl.Instrum.Meth.*, A618:139–152, 2010. doi: 10.1016/j.nima.2010.03.102.

R. Abbasi et al. Constraints on the extremely-high energy cosmic neutrino flux with the icecube 2008-2009 data. *Phys. Rev. D*, 83:092003, May 2011. doi: 10.1103/PhysRevD.83.092003. URL http://link.aps.org/doi/10.1103/PhysRevD.83.092003.

A.A. Abdo. Observations of the young supernova remnant RX J1713.7-3946 with the Fermi Large Area Telescope. *Astrophys.J.*, 734:28, 2011. doi: 10.1088/0004-637X/734/1/28.

K. Abe, T. Abe, H. Aihara, Y. Fukuda, Y. Hayato, et al. Letter of Intent: The Hyper-Kamiokande Experiment — Detector Design and Physics Potential —. 2011.

P. Abreu et al. The Pierre Auger Observatory III: Other Astrophysical Observations. 2011.

W.D. Apel, J.C. Arteaga-Velzquez, K. Bekk, M. Bertaina, J. Blmer, et al. KASCADE-Grande measurements of energy spectra for elemental groups of cosmic rays. *Astropart.Phys.*, 47:54–66, 2013. doi: 10.1016/j.astropartphys.2013.06.004.

R. Atkins et al. Evidence for TeV gamma-ray emission from the galactic plane. *Phys.Rev.Lett.*, 95:251103, 2005. doi: 10.1103/PhysRevLett.95.251103.

T. Avgitas, G. Bourlis, A. Leisos, A. Tsirigotis, and S.E. Tzamarias. Characterization of hamamatsu r12199-02 pmts for the km3net. *HEP2013, Recent Developments in High Energy Physics and Cosmology*, 2013. URL http://physicslab.eap.gr/EN/Conferences_&_Seminars_files/6_HEP2013_Avgitas.pdf.

W. Baade and F. Zwicky. Remarks on super-novae and cosmic rays. *Phys. Rev.*, 46:76–77, Jul 1934. doi: 10.1103/PhysRev.46.76.2. URL http://link.aps.org/doi/10.1103/PhysRev.46.76.2.

G. Barbarino, R. de Asmundis, G. De Rosa, C.M. Mollo, S. Russo, and D. Vivolo. *Silicon Photo Multipliers Detectors Operating in Geiger Regime: an Unlimited Device for Future Applications*. Intech, 2011. URL http://www.intechopen.com/books/photodiodes-world-activities-in-2011/silicon-photo-multipliers-detectors-operating-in-geiger-regime-an-unlimited-device-

G Barbarino, L Campajola, R de Asmundis, G De Rosa, G Fiorillo, P Migliozzi, F C T Barbato, C M Mollo, A Russo, and D Vivolo. Proof of feasibility of the vacuum silicon photomultiplier tube (vsipmt). *Journal of Instrumentation*, 8(04):P04021, 2013a. URL `http://stacks.iop.org/1748-0221/8/i=04/a=P04021`.

Giancarlo Barbarino, Riccardo de Asmundis, Gianfranca De Rosa, Giuliana Fiorillo, Valentina Gallo, et al. A new high-gain vacuum photomultiplier based upon the amplification of a Geiger-mode p-n junction. *Nucl.Instrum.Meth.*, A594:326–331, 2008. doi: 10.1016/j.nima.2008.06.026.

Giancarlo Barbarino, Riccardo de Asmundis, Gianfranca De Rosa, Stefano Russo, Daniele Vivolo, and Carlos Maximiliano Mollo. Light concentrators for silicon photomultipliers. *Physics Procedia*, 37(0):709 – 714, 2012. ISSN 1875-3892. doi: http://dx.doi.org/10. 1016/j.phpro.2012.02.420. URL `http://www.sciencedirect.com/science/article/ pii/S1875389212017622`. Proceedings of the 2nd International Conference on Technology and Instrumentation in Particle Physics (TIPP 2011).

Giancarlo Barbarino, Riccardo de Asmundis, Gianfranca De Rosa, Carlos Maximiliano Mollo, and Daniele Vivolo. {VSiPMT} for underwater neutrino telescopes. *Nuclear Instruments and Methods in Physics Research Section A: Accelerators, Spectrometers, Detectors and Associated Equipment*, 725(0):162 – 165, 2013b. ISSN 0168-9002. doi: http://dx.doi.org/10.1016/j.nima.2012.12.097. URL `http://www. sciencedirect.com/science/article/pii/S0168900212016531`. VLVT 11, Erlangen, Germany, 12 - 14 October, 2011 5th International Workshop on Very Large Volume Neutrino Telescopes, The future of high-energy neutrino astronomy.

Julia K. Becker. High-energy neutrinos in the context of multimessenger physics. *Phys.Rept.*, 458:173–246, 2008. doi: 10.1016/j.physrep.2007.10.006.

J. Beringer et al. Review of Particle Physics (RPP). *Phys.Rev.*, D86:010001, 2012. doi: 10.1103/PhysRevD.86.010001.

Pijushpani Bhattacharjee and Gunter Sigl. Origin and propagation of extremely highenergy cosmic rays. *Phys.Rept.*, 327:109–247, 2000. doi: 10.1016/S0370-1573(99) 00101-5.

Aurelien Bouvier, Lloyd Gebremedhin, Caitlin Johnson, Andrey Kuznetsov, David Williams, et al. Photosensor Characterization for the Cherenkov Telescope Array: Silicon Photomultiplier versus Multi-Anode Photomultiplier Tube. 2013. doi: 10.1117/12.2023778.

J. Brack, B. Delgado, J. Dhooghe, J. Felde, B. Gookin, S. Grullon, J. R. Klein, R. Knapik, A. LaTorre, S. Seibert, K. Shapiro, R. Svoboda, L. Ware, and R. Van Berg. Characterization of the Hamamatsu R11780 12 in. photomultiplier tube. *Nuclear Instruments and Methods in Physics Research A*, 712:162–173, June 2013. doi: 10.1016/j.nima.2013.02.022.

A.J. Cohen, K.F. Koral, and Lewis Research Center. *Backscattering and secondaryelectron emission from metal targets of various thicknesses*. NASA technical note.

National Aeronautics and Space Administration, 1965. URL `http://books.google.it/books?id=Vs5-0i-QoQAC`.

P C Divari. Supernova neutrino reactions on 114 cd and 116 cd isotopes via charge current interaction. *Journal of Physics G: Nuclear and Particle Physics*, 40(12):125201, 2013. URL `http://stacks.iop.org/0954-3899/40/i=12/a=125201`.

Albert Einstein. On a heuristic viewpoint concerning the production and transformation of light. *Annalen der Physik*, 17:Original title: ¨Uber einen die Erzeugung und Verwandlung des Lichtes betreffenden heuristischen Gesichtspunkt, 1905. URL `http://lorentz.phl.jhu.edu/AnnusMirabilis/AeReserveArticles/eins_lq.pdf`.

R. Enomoto and R. Enomoto. The acceleration of cosmic-ray protons in the supernova remnant rx j1713.7-3946. *Nature*, 416:823–826, 2002. doi: 10.1038/416823a.

D. Fargion. Air-shower spectroscopy at horizons. *Progress in Particle and Nuclear Physics*, 57(1):384 – 393, 2006. ISSN 0146-6410. doi: http://dx.doi.org/10.1016/j.ppnp.2005.11.015. URL `http://www.sciencedirect.com/science/article/pii/S0146641005001262`. International Workshop of Nuclear Physics 27th course Neutrinos in Cosmology, in Astro, Particle and Nuclear Physics Ettore Majorana Center for Scientific Culture.

ENRICO Fermi. On the origin of the cosmic radiation. *Phys. Rev.*, 75:1169–1174, Apr 1949. doi: 10.1103/PhysRev.75.1169. URL `http://link.aps.org/doi/10.1103/PhysRev.75.1169`.

Yasuo Fukui. Molecular and Atomic Gas in the Young TeV γ-Ray SNRs RX J1713.7-3946 and RX J0852.0-4622 Evidence for the Hadronic Production of γ-Rays. *Astrophys.Space Sci.Proc.*, 34:249–270, 2013. doi: 10.1007/978-3-642-35410-6_17.

T.K. Gaisser. The cosmic-ray spectrum: From the knee to the ankle. *J.Phys.Conf.Ser.*, 47:15–20, 2006. doi: 10.1088/1742-6596/47/1/002.

Wolfgang W. Gärtner. Depletion-layer photoeffects in semiconductors. *Phys. Rev.*, 116:84–87, Oct 1959. doi: 10.1103/PhysRev.116.84. URL `http://link.aps.org/doi/10.1103/PhysRev.116.84`.

P.W. Gorham et al. Erratum: Observational Constraints on the Ultra-high Energy Cosmic Neutrino Flux from the Second Flight of the ANITA Experiment. *Phys.Rev.*, D85:049901, 2012. doi: 10.1103/PhysRevD.82.022004,10.1103/PhysRevD.85.049901.

Martin A. Green and Mark J. Keevers. Optical properties of intrinsic silicon at 300 k. *Progress in Photovoltaics: Research and Applications*, 3:189 – 192, 1995 1995. ISSN 1099159X. doi: 10.1002/pip.4670030303. ¡br /¿.

Claus Grupen. *Astroparticle Physics*. Springer, 2005.

Hamamatsu-Photonics. *PHOTOMULTIPLIER TUBES - Basics and applications. 3rd edition.* 2006.

Hamamatsu-Photonics. *MPPC - Multi Pixel Photon Counter*. 2010.

Hamamatsu-Photonics. *Opto-Semiconductor Handbook*. 2013.

Hamamatsu-Photonics. *MPPC Selection guide*. 2014a.

Hamamatsu-Photonics. S12571-025, -050, -100c/p datasheet. 2014b.

H. Hertz. Ultraviolet Light of Spark. *Annalen der Physik*, 31:983–1000, 1887.

Harley Iams and B. Salzberg. The secondary emission phototube. *Radio Engineers, Proceedings of the Institute of*, 23(1):55–64, Jan 1935. ISSN 0731-5996. doi: 10.1109/ JRPROC.1935.227243.

O. Kalekin. Characterization of hamamatsu r12199-02 pmts for the km3net. *KM3NeT Collaboration Meeting, LNS-INFN Catania, 25-06-2013*, 2013.

U. Katz. News from KM3NeT. 2014.

Ulrich F. Katz and Christian Spiering. High-energy neutrino astrophysics: Status and perspectives. *Prog. Part. Nucl. Phys.*, 67:651–704, 2012.

E. Kearns et al. Hyper-Kamiokande Physics Opportunities. 2013.

Shunji Kishimoto. An avalanche photodiode detector for x-ray timing measurements. *Nuclear Instruments and Methods in Physics Research Section A: Accelerators, Spectrometers, Detectors and Associated Equipment*, 309(3):603 – 605, 1991. ISSN 0168-9002. doi: http://dx.doi.org/10.1016/0168-9002(91)90272-R. URL `http://www.sciencedirect.com/science/article/pii/016890029190272R`.

KM3NeT-Collaboration. Conceptual design for a deep?sea research infrastructure incorporating a very large volume neutrino telescope in the mediterranean sea. 2008.

KM3NeT-Collaboration. Technical design report for a deep-sea research infrastructure in the mediterranean sea incorporating a very large volume neutrino telescope. 2010.

KM3NeT-collaboration. Expansion cone for the 3-inch pmts of the km3net optical modules. *Journal of Instrumentation*, 8(03):T03006, 2013. URL `http://stacks.iop.org/1748-0221/8/i=03/a=T03006`.

Ilya Kravchenko, S. Hussain, Dave Seckel, Dave Besson, E. Fensholt, et al. Updated Results from the RICE Experiment and Future Prospects for Ultra-High Energy Neutrino Detection at the South Pole. *Phys.Rev.*, D85:062004, 2012. doi: 10.1103/PhysRevD.85.062004.

P. Lenard. Ueber die lichtelektrische wirkung. *Annalen der Physik*, 313(5):149–198, 1902. ISSN 1521-3889. doi: 10.1002/andp.19023130510. URL `http://dx.doi.org/10.1002/andp.19023130510`.

M. A. Markov and I. M. Zheleznykh. On high energy neutrino physics in cosmic rays. *Nucl. Phys.*, 27:385–394, 1961.

K. G. McKay and K. B. McAfee. Electron multiplication in silicon and germanium. *Phys. Rev.*, 91:1079–1084, Sep 1953. doi: 10.1103/PhysRev.91.1079. URL `http://link.aps.org/doi/10.1103/PhysRev.91.1079`.

S. L. Miller. Ionization rates for holes and electrons in silicon. *Phys. Rev.*, 105:1246–1249, Feb 1957. doi: 10.1103/PhysRev.105.1246. URL `http://link.aps.org/doi/10.1103/PhysRev.105.1246`.

L. Neri, S. Tudisco, F. Musumeci, A. Scordino, G. Fallica, et al. Dead time of single photon avalanche diodes. *Nucl.Phys.Proc.Suppl.*, 215:291–293, 2011. doi: 10.1016/j.nuclphysbps.2011.04.034.

Julio Rodrguez Martino Pablo M. Bauleo. The dawn of the particle astronomy era in ultra-high-energy cosmic rays, 2009. URL `http://www.nature.com/nature/journal/v458/n7240/full/nature07948.html`.

B. Peters. Primary cosmic radiation and extensive air showers. *Il Nuovo Cimento*, 22 (4):800–819, 1961. ISSN 0029-6341. doi: 10.1007/BF02783106. URL `http://dx.doi.org/10.1007/BF02783106`.

G. Riccobene. Results from NEMO and Km3Net. *J.Phys.Conf.Ser.*, 60:235–238, 2007. doi: 10.1088/1742-6596/60/1/050.

R. P. Riesz. High speed semiconductor photodiodes. *Review of Scientific Instruments*, 33(9):994–998, Sep 1962. ISSN 0034-6748. doi: 10.1063/1.1718049.

B.E.A. Saleh and M.C. Teich. *Fundamentals of photonics, Volume 2*. Matfyzpress, 1994.

B.E.A. Saleh and M.C. Teich. *Fundamentals of Photonics*. Wiley Series in Pure and Applied Optics. Wiley, 2007. ISBN 9780471358329. URL `http://books.google.it/books?id=Ve8eAQAAIAAJ`.

SensL. *Introduction to the SPM . technical note.* 2011.

Frank Simon. Studies of Scintillator Tiles with SiPM Readout for Imaging Calorimeters. *J.Phys.Conf.Ser.*, 293:012074, 2011. doi: 10.1088/1742-6596/293/1/012074.

T. Tanaka, A. Allafort, J. Ballet, S. Funk, F. Giordano, J. Hewitt, M. Lemoine-Goumard, H. Tajima, O. Tibolla, and Y. Uchiyama. Gamma-ray observations of the supernova remnant rx j0852.04622 with the fermi large area telescope. *The Astrophysical Journal Letters*, 740(2):L51, 2011. URL `http://stacks.iop.org/2041-8205/740/i=2/a=L51`.

P. Timmer, E. Heine, and H. Peek. Very low power, high voltage base for a photo multiplier tube for the KM3NeT deep sea neutrino telescope. *JINST*, 5:C12049, 2010. doi: 10.1088/1748-0221/5/12/C12049.

Albert H. Titus, Maurice C.K. Cheung, and Vamsy P. Chodavarapu. *Photodiodes - World Activities in 2011*. Intech, 2011. URL `http://www.intechopen.com/books/export/citation/BibTex/photodiodes-world-activities-in-2011/cmos-photodetectors`.

V.K. V.K. Zworykin, G.A. Morton, and L. Malter. The secondary emission multiplier-a new electronic device. *Radio Engineers, Proceedings of the Institute of*, (24):351, Mar 1936.

Eli Waxman and John N. Bahcall. High-energy neutrinos from astrophysical sources: An Upper bound. *Phys.Rev.*, D59:023002, 1999. doi: 10.1103/PhysRevD.59.023002.

R. Winston and J. O'Gallagher. Nonimaging concentrators (optics). In Robert A. Meyers, editor, *Encyclopedia of Physical Science and Technology (Third Edition)*, pages 507 – 522. Academic Press, New York, third edition edition, 2003. ISBN 978-0-12-227410-7. doi: http://dx.doi.org/10.1016/B0-12-227410-5/00483-X. URL `http://www.sciencedirect.com/science/article/pii/B012227410500483X`.

F. Zwicky. Die Rotverschiebung von extragalaktischen Nebeln. *Helv.Phys.Acta*, 6:110–127, 1933.

V.K. Zworykin and J.A. Rajchman. The electrostatic electron multiplier. *Proceedings of the IRE*, 27(9):558–566, Sept 1939. ISSN 0096-8390. doi: 10.1109/JRPROC.1939.228753.